POLITECNICO
MILANO 1863

SCUOLA DI INGEGNERIA INDUSTRIALE
E DELL'INFORMAZIONE

# Performance of new collimation optics for improved cleaning and impedance at the Large Hadron Collider

Tesi di Laurea Magistrale in
Nuclear Engineering

Author: **Ludovica Bertolozzi**

Student ID: 10684753
Advisor: Prof. Marco Beghi
Co-advisors: Stefano Redaelli (CERN), Bjorn Lindstrom (CERN, RHUL)
Academic Year: 2024-25

# Abstract

The High-Luminosity Large Hadron Collider (HL-LHC) project aims to significantly increase the luminosity of the LHC. One of the key factors in achieving this goal is the increase in beam intensity by a factor of 2 compared to the LHC design. This poses two major challenges related to beam collimation: the collimation cleaning performance, and the collimation-induced machine impedance. To address these challenges, a new optics configuration for the betatron cleaning insertion has been developed, which improves both aspects.

This thesis work produced the first implementation of the new optics in the LHC operational cycle, and in particular the deployment of the optics change during the energy ramp. This is achieved through a delicate "optics de-squeeze" transition from the nominal optics at injection energy to the new configuration at top energy. This work included the design of the optics transitions, the development of the matching procedure and tools, and the preparation for the LHC beam tests. Beam tests were also carried out at the LHC in dedicated machine development sessions: this work also addressed their analysis. Given the excellent results with low-intensity beams, the optics was considered adequate for high-intensity beam tests at the LHC, which were prepared and followed up. The successful completion of high-intensity tests is a crucial milestone in assessing the operational feasibility of this new configuration at the HL-LHC.

The expected cleaning performance was evaluated through simulations both at top energy and during the energy ramp, and compared to the performance by the reference optics. The measured cleaning shows an improvement and a good agreement with simulations. Dedicated impedance measurements, carried out by colleagues in the Accelerator and Beam Physics group using the optics developed within this thesis, showed an improvement close to predictions.

These results demonstrate that the new betatron collimation optics can be safely deployed during the LHC energy ramp and is effective in mitigating beam losses and impedance with high beam intensities, also confirming the reliability of the modelling tools for future HL-LHC operation. At the time of writing, these changes are considered for deployment at the LHC during the 2026 run.

# Abstract italian

Il progetto High-Luminosity Large Hadron Collider (HL-LHC) mira ad aumentare significativamente la luminosità dell'LHC e uno dei fattori chiave per raggiungere questo obiettivo è il raddoppio dell'intensità del fascio rispetto al valore di design dell'acceleratore. Questo pone due sfide principali relative alla collimazione del fascio: le prestazioni di cleaning della collimazione e l'impedenza della macchina indotta dal sistema di collimazione. Per affrontare queste sfide, è stata sviluppata una nuova configurazione ottica per l'inserzione di collimazione betatronica che migliora entrambi questi due aspetti.
Questo lavoro di tesi ha prodotto la prima implementazione della nuova ottica nel ciclo operativo dell'LHC, e in particolare l'implementazione del cambiamento dell'ottica durante la rampa di energia. Ciò è stato realizzato con una delicata "de-squeeze" dell'ottica per passare dall'ottica nominale all'energia di iniezione alla nuova configurazione all'energia massima. Questo lavoro ha incluso la progettazione di una transizione ottica, lo sviluppo della procedura e degli strumenti del "matching" e la preparazione per i test del fascio dell'LHC. I test del fascio sono stati effettuati sull'LHC in sessioni dedicate allo sviluppo della macchina: questo lavoro ha affrontato anche la loro analisi.
Dati gli eccellenti risultati ottenuti con fasci a bassa intensità, l'ottica è stata ritenuta adeguata per i test con fasci ad alta intensità sull'LHC, anch'essi preparati e monitorati nell'ambito di questo lavoro di tesi. Il completamento con successo dei test ad alta intensità rappresenta una tappa fondamentale nella valutazione della fattibilità operativa di questa nuova configurazione per HL-LHC. Le prestazioni di cleaning previste sono state valutate attraverso simulazioni sia all'energia massima sia durante la rampa di energia, e confrontate con le prestazioni dell'ottica di riferimento. Le prestazioni di cleaning misurate mostrano un miglioramento e una buona corrispondenza con le simulazioni. Misurazioni di impedenza dedicate, effettuate dai colleghi del gruppo Accelerator and Beam Physics utilizzando l'ottica sviluppata nell'ambito di questo progetto, hanno mostrato un miglioramento in linea con le previsioni.
Questi risultati dimostrano che la nuova ottica di collimazione betatronica può essere implementata in sicurezza durante la rampa di energia dell'LHC ed è efficace nel ridurre le perdite di fascio e l'impedenza con alte intensità di fascio, confermando anche l'affidabilità

degli strumenti di modellizzazione per il futuro funzionamento dell'HL-LHC. Al momento della stesura di questa tesi, si sta valutando l'implementazione di queste modifiche nell'LHC a partire dal run del 2026.

# Contents

# 1 | Introduction

Particle colliders for physics research are machines used for studying high energy physics by accelerating beams of particles and making them collide, in order to produce new and rare particles and investigate the fundamental interactions of nature. To push their performances to the limit, key goals are reaching the highest possible energy of the particles and maximizing the collision rate.

The Large Hadron Collider (LHC) is the largest and most powerful accelerator ever built. With a circumference of almost 27 km, it is located at CERN, on the Franco-Swiss border close to Geneva, in Switzerland. It is designed to accelerate proton and ion beams to an energy of 7 TeV and 574 TeV respectively. Two high-energy particle beams travel in opposite directions and they collide in four points, where experiment detectors are located. As designed, the two counter-rotating beams have intensities of $3.2 \times 10^{14}$ protons and $4.1 \times 10^{10}$ lead ions and the stored energy per proton beam amounts to 362 MJ.

To bend and focus the beams, dipole and quadrupole magnets are installed along the accelerator. Most of them operate in a superconducting state at a temperature of 1.9 K. In these conditions, even minimal energy losses can lead to a loss of the superconductivity condition: less than one billionth of the total energy stored by the circulating beams is sufficient to quench the magnets. Therefore, an efficient collimation system is essential. Its main goal is the controlled disposal of unavoidable beam losses that could otherwise occur at sensitive areas or on accelerator components that are not designed to withstand them.

The LHC is equipped with a multi-stage collimation system that provides an efficient beam cleaning performance. LHC collimators consist of two parallel, movable blocks of material called jaws. Their position define the gap through which the beam particles can pass unperturbed, particles with large orbit errors are intercepted by the jaws in order to prevent uncontrollable beam losses. In the LHC the collimation system is located in two dedicated insertion regions (IRs): the momentum cleaning insertion, IR3, which provides the cleaning of off-momentum particles, and the betatron cleaning insertion, IR7, where particles with too large transverse oscillation amplitudes are intercepted. In addition to

these dedicated insertions, other collimators are installed around the ring, such as near the collision points and at the injection and extraction regions.

At present (2025), the LHC is in its third operational Run, known as Run 3, delivering proton-proton collisions at 13.6 TeV

The next major upgrade is the High-Luminosity LHC (HL-LHC) project. The HL-LHC project aims to boost the performance of LHC machine to extend its discovery potential, by increasing the instantaneous luminosity from 1 to $5 \times 10^{34}$ $\mathrm{cm}^{-2}\,\mathrm{s}^{-1}$ and reaching an integrated luminosity of 250 $\mathrm{fb}^{-1}$ per year, with the goal of 3000 $\mathrm{fb}^{-1}$ in about 12 years after the upgrade [9]. One of the major factors in achieving these luminosity targets is an increase of the bunch intensity from $1.15 \times 10^{11}$ ppb (protons per bunch) to $2.2 \times 10^{11}$ ppb. This poses significant challenges for the collimation system. First of all, the leakage of losses from the collimation insertion to the downstream superconducting magnets, that can potentially lead to quenches. In addition, the impedance (see Section 2.1.4), for which the collimation system is the main contributor, can trigger beam instabilities.

A new optics for proton beams in the betatron cleaning insertion has been developed to face these two challenges, improving the performance of the collimation cleaning and reducing its effective impedance. Due to aperture constraints, the new optics is inserted during the energy ramp of the LHC: a complex and delicate challenge which has never been done operationally before. The present work focuses on the design and validation of the optics transition during the energy ramp through both simulations and experiments.
In Chapter 2 the fundamental concepts of accelerator physics are provided, together with the notation used throughout this document. In particular, the basic principles of linear beam dynamics and collimation theory concepts are introduced. Still in chapter 2, the HL-LHC project is presented together with its challenges for the collimation system.
In Chapter 3, the development of the new optics for the betatron collimation insertion (IR7) is presented. The main goals of the new optics are introduced, together with its challenges. The chapter provides the procedure to obtain the new optics configuration in the energy ramp of the LHC and the tools used to perform it.
Chapter 4 describes the simulation results for the new optics. After a description of the tools used to perform the simulations, the expected cleaning performance of the collimation system is evaluated both at top energy and during the energy ramp. The chapter provides an evaluation of the expected cleaning improvements compared to the reference optics. The impact of different collimator settings scenarios on the cleaning performance is also analyzed.
Chapter 5 presents the experimental validation of the new optics. First, it summarizes the Machine Development sessions performed in 2025. The results demonstrate a suc-

cessful deployment of the optics in the LHC. The chapter analyzes the measured cleaning performance both at top energy and during the ramp of the LHC. The impedance results are also discussed. Moreover, it analyzes the comparison between the simulations and measurements. Finally, conclusions are drawn.

# 2 | Beam collimation in the LHC and the future High Luminosity LHC

The beam circulating in a circular accelerator consists of bunches of particles and the particle distribution in each bunch can be represented by a Gaussian distribution. In ideal conditions, particles travel along the reference orbit, which is the ideal trajectory defined by the accelerator design. The center of the Gaussian corresponds to the core of the bunch, where particles perform quasi-stable oscillations around the reference orbit. Particles that populate the tails of the distribution, the so-called halo, can eventually hit the aperture of the machine. If they hit the superconducting magnets, the resulting energy deposition can lead to magnet quenches. Therefore, an efficient collimation system is needed. Collimators intercept halo particles, providing halo cleaning and protection of the machine.

## 2.1. Accelerator fundamentals

The beam in an accelerator is subject to a combination of forces from electric and magnetic fields. The motion of a charged particle subjected to these fields is described by the Lorentz force:

$$\frac{d\vec{p}}{dt} = q(\vec{E} + \vec{v} \times \vec{B}), \tag{2.1}$$

where $\vec{p}$ is the relativistic momentum of the particle, $q$ is the charge, $\vec{v}$ is the velocity and $\vec{E}$ and $\vec{B}$ are the electric and magnetic fields, respectively. The magnetic field generates a change of momentum perpendicular to the particle velocity, bending its trajectory and keeping it confined along the designed orbit. The electric field generates a change of momentum in the direction of the field, accelerating or decelerating the particle.
In circular accelerators, these functions are fulfilled, respectively, by dipole magnets, which bend the beam, and by the Radio-frequency (RF) system, which accelerates the particles and compensates for the energy lost by synchrotron radiation. The accelerating electric

field is produced by RF cavities, metallic resonators that confine electromagnetic waves at specific frequencies. When an alternating voltage is applied to the cavities, standing waves are formed at a resonant frequency that is synchronized with the revolution frequency of the particles. Therefore, each time the particles pass through the cavity, they receive an energy kick that accelerates them. The frequency of the applied voltage typically lies in the radio frequency range, hence the name *RF cavity*. These cavities not only accelerate the particles, but also define a region in the longitudinal phase space, called *RF bucket*, that contains the particles that are synchronized with the RF field and are longitudinally stable. Therefore, the RF cavities produce longitudinally separated groups of particles, known as *bunches*, each contained in an RF bucket.
Particles outside the bucket are not synchronized with the RF field: they can gain or lose energy turn by turn, depending on their phase, and are ideally lost at collimators.
Magnetic fields are used to bend and focus the particles travelling around the machine, see Fig 2.1. Dipole magnets generate a uniform dipolar field that bends the particles along the accelerator, defining a closed orbit on which, ideally, a particle with nominal energy can move indefinitely. In practice, particles diverge from the closed orbit, therefore they need to be focused. This effect is provided by quadrupolar magnets, which generate a quadrupolar magnetic field that focuses the particles in one plane and defocuse them in the other plane. By alternating focusing and defocusing quadupoles, a configuration of magnets can be found that provides an overall focusing of the beam. Higher-order magnets, such as sextupoles, octupoles and so on, provide corrections for non-linear effects and chromatic aberrations.

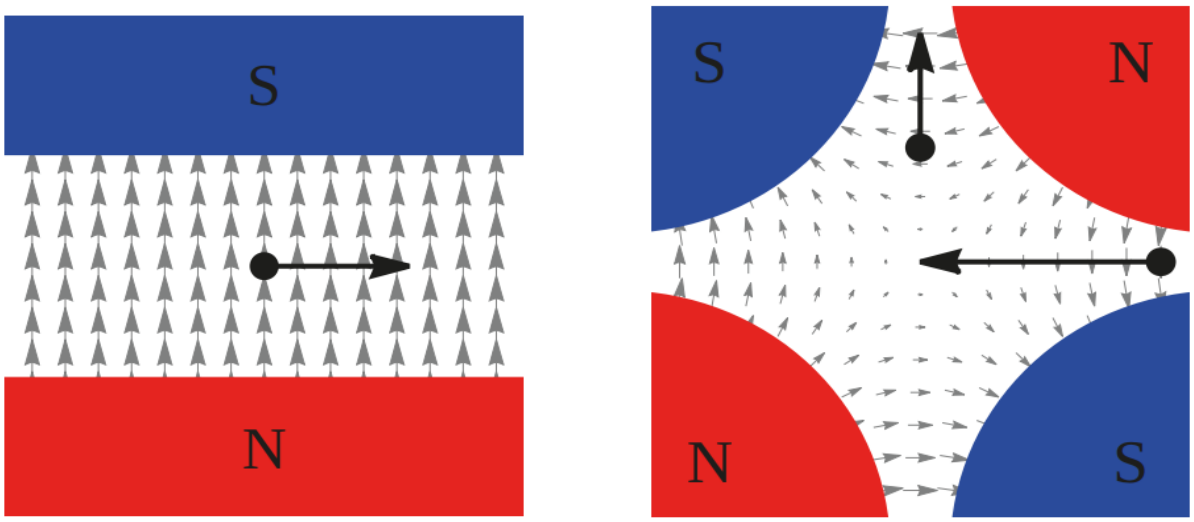


Figure 2.1: Magnetic fields for a dipole (left) and a quadrupole (right) magnet. Dipole magnet generates a uniform magnetic field between the two poles that bends the charged particles on their orbit. Quadrupole magnet produces a field that increases linearly with the distance from the center, focusing in one transverse plane and defocusing in the other [22]. These schematics are shown to illustrate the conceptual field distributions and do not represent the physical layout of the LHC superconducting magnets, where the fields are generated by coil geometry.

### 2.1.1. Basic principles of linear beam dynamics

In this section, the transverse motion of a charged particle in a circular accelerator is described in the steady state regime, at constant beam energy.
A right-handed orthogonal and moving reference system $(x,y,z)$ is considered, as illustrated in Fig.2.2 (2.2)
The circular black line represents the reference closed orbit along which the charged particle travels, with $\vec{r_0}$ the orbital radius. The $\vec{z}$ vector is tangent to the closed orbit and represents the longitudinal direction of motion, the $\vec{y}$ and $\vec{x}$ vectors represent the vertical and horizontal position of the particle with respect to the closed orbit.
Equating the Lorentz and centrifugal forces for a constant magnetic field $\vec{B}$ perpendicular to the particle velocity gives:

$$F = qvB = \frac{\gamma m v^2}{\rho} \tag{2.2}$$

where $v$ is the speed of the particle with charge $q$, $\gamma$ is the Lorentz factor, $m$ is the mass of the particle and $\rho$ the radius of curvature. Rewriting this equation, the *magnetic rigidity*

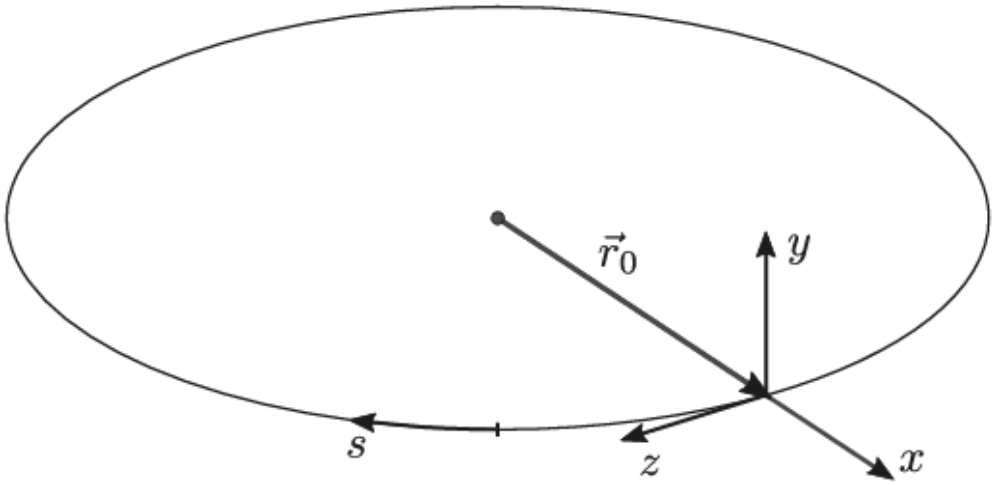


Figure 2.2: Right-handed moving reference system.

can be defined:

$$B\rho = \frac{p}{q} \tag{2.3}$$

This represents the resistance of the beam when subject to a magnetic field. It highlights the direct relation between the magnetic field and the radius of curvature: to keep a particle on a circular trajectory with a given radius $\rho$, a stronger magnetic field $B$ is required for particles with higher momentum.
In the following, the derivation of the general equation of particle motion in the transverse plane with respect to the design orbit is presented using a moving coordinate system.
In transverse beam dynamics, the longitudinal motion and the energy variation are neglected. Therefore the electric field $\vec{E}$ is not considered and only the magnetic field is taken into account.
In a circular accelerator, usually only the transverse components of the magnetic field are non-zero, i.e. $B = (B_x, B_y, 0)$, where $B_x$ and $B_y$ are the horizontal and vertical components of the field.
For small variations around the design orbit, $B_x$ and $B_y$ can be expanded in a first-order Taylor series:

$$B_x(x, y, s) = B_{x0} + \frac{\partial B_x}{\partial x}x + \frac{\partial B_x}{\partial y}y \tag{2.4}$$

$$B_y(x, y, s) = B_{y0} + \frac{\partial B_y}{\partial x}x + \frac{\partial B_y}{\partial y}y \tag{2.5}$$

where:

- $B_{x0}$ and $B_{y0}$ represent the dipole fields, which bend the particles in vertical and

horizontal plane.

- $\frac{\partial B_x}{\partial y}$ and $\frac{\partial B_y}{\partial x}$ represent the quadrupole field, focusing in one plane and defocusing in the other.
- $\frac{\partial B_x}{\partial x}$ and $\frac{\partial B_y}{\partial y}$ represent skew quadrupole fields, which couple the horizontal and vertical motion of the particles.

From Maxwell's equations, assuming a magnetic field with only transverse components ($B_z$=0), an electric field equal to zero ($\vec{E}$ =0) and no currents in the region of interest ($\vec{J}$ =0) , the following relations are obtained:

$$\frac{\partial B_x}{\partial x} = -\frac{\partial B_y}{\partial y} \tag{2.6}$$

$$\frac{\partial B_y}{\partial x} = \frac{\partial B_x}{\partial y} \tag{2.7}$$

In a circular accelerator, usually the vertical dipole field is used to bend the particles in the horizontal plane and the quadrupole field provide focusing. Therefore the horizontal dipole field ($B_{x0}$) and the skew quadrupoles components ($\frac{\partial B_x}{\partial x}$ and $\frac{\partial B_y}{\partial y}$) can be neglected. Eq. 2.4 and Eq. 2.5 can be rewritten as:

$$B_x = \frac{\partial B_y}{\partial x} y = B_1 y \tag{2.8}$$

$$B_y = -B_0 + \frac{\partial B_y}{\partial x} x = -B_0 + B_1 x \tag{2.9}$$

where $B_0$ represents the dipole field and $B_1$ represents the quadrupole gradient.
Considering only particles with design momentum and keeping only the linear terms, the transverse motion can be described by the following equations:

$$x'' + K_x(s)x = 0, \quad K_x(s) = \frac{1}{\rho(s)^2} - \frac{B_1(s)}{B\rho(s)} \tag{2.10}$$

$$y'' + K_y(s)y = 0, \quad K_y(s) = -\frac{B_1(s)}{B\rho(s)} \tag{2.11}$$

where $x'' = \frac{d^2x}{ds^2}$, $y'' = \frac{d^2y}{ds^2}$, with $s$ the longitudinal coordinate along the reference orbit.
The functions $K_x(s)$ and $K_y(s)$ represent the focusing strengths in the horizontal and vertical planes and $\rho(s)$ is the bending radius of the reference orbit. For constant $\rho(s)$ and $K_{x,y}(s)$ within each magnetic element, these equations describe a harmonic oscillator or an exponential function, depending on the sign of $K_{x,y(s)}$.

When the focusing functions $K_{x,y}(s)$ are periodic along the accelerator lattice, as in most circular accelerators, the equations 2.10 and 2.11 are known as Hill's equations.
The solution of the Hill's equation in the horizontal plane is [30]:

$$x(s) = A_0 \sqrt{\beta_x(s)} \sin\left(\varphi_x(s) + \varphi_0\right) \tag{2.12}$$

where $\beta_x(s)$ is the *betatron function*, a periodic function that modulates the amplitude $A_0$ of the transverse oscillations, and $\varphi_0$ is an initial phase constant.
The phase advance $\varphi_x(s)$ is given by:

$$\varphi_x(s) = \int_0^s \frac{ds'}{\beta(s')} \tag{2.13}$$

Other parameters related to the $\beta$ function can be defined:

$$\alpha(s) = -\frac{1}{2}\frac{d\beta(s)}{ds}, \tag{2.14}$$

$$\gamma(s) = \frac{1+\alpha(s)^2}{\beta(s)} \tag{2.15}$$

The functions $\alpha(s)$, $\beta(s)$ and $\gamma(s)$, known as *Twiss parameters*, describe the transverse beam dynamics and are defined by the machine optics.
In the transverse phase space (*x,x'*), the motion of a single particle can be represented by an ellipse, shown in Fig. 2.10 (2.2)
The phase space ellipse is described by the following equation:

$$\varepsilon_x = \gamma_x(s)\, x^2(s) + 2\alpha_x(s)\, x(s)x'(s) + \beta_x(s)\, x'^2(s) \tag{2.16}$$

The shape of the ellipse depends on the position $s$ along the accelerator, while its area remains constant.
All the particles of the beam can be statistically represented by a Gaussian distribution in the transverse phase space. The corresponding *betatronic beam size* $\sigma_x$ and divergence $\sigma'_x(s)$ at a certain position $s$ are expressed as:

$$\sigma_x(s) = \sqrt{\varepsilon_{x,\mathrm{rms}}\, \beta_x(s)} \tag{2.17}$$

$$\sigma'_x(s) = \sqrt{\varepsilon_{x,\mathrm{rms}}\, \gamma_x(s)} \tag{2.18}$$

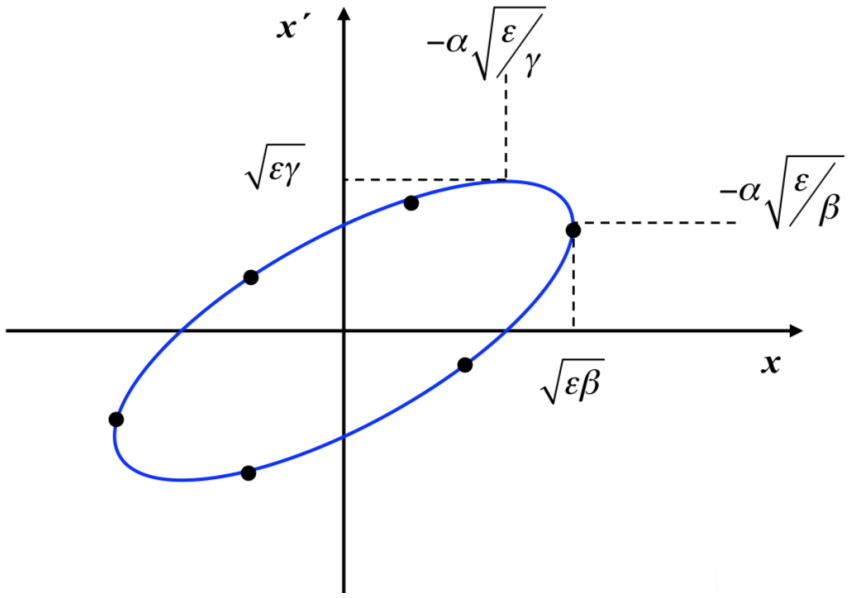


Figure 2.3: Elliptical trajectory in the transverse phase space.

where $\varepsilon_{x,\mathrm{rms}}$ is the *root mean square emittance* which is defined as:

$$\varepsilon_{x,\mathrm{rms}} = \sqrt{\langle x^2\rangle\langle x'^2\rangle - \langle xx'\rangle^2} \tag{2.19}$$

The terms $\langle x^2\rangle$, $\langle x'^2\rangle$ and $\langle xx'\rangle^2$ correspond, respectively, to the variance of the transverse position, the variance of the divergence and the covariance between the position and angle. The beam core is defined as the region containing the particles within $3\sigma_x(s)$ from the beam centre, while the particles outside this region form the beam halo.
A *normalised emittance*, invariant with respect to energy, is defined as:

$$\varepsilon_{x,norm} = \gamma_{rel}\beta_{rel}\varepsilon_{x,rms} \tag{2.20}$$

where $\beta_{rel} = v/c$, $v$ is the speed of the particle, $c$ is the speed of light in vacuum and $\gamma = \frac{1}{\sqrt{1-\beta_{rel}^2}}$.
The betatron tune is defined as the number of betatron oscillations that a particle performs throughout the length $L$ of the full machine:

$$Q = \frac{\varphi(L)}{2\pi} = \frac{1}{2\pi}\int_0^L \frac{ds}{\beta(s)} \tag{2.21}$$

Chromaticity describes how the betatron tune varies with the particle momentum. It is defined as:

$$Q = \frac{dQ}{d\delta}, \tag{2.22}$$

where $\delta$ is the relative momentum deviation. Since quadrupoles focus particles differently depending on their momentum, even small variation in $\delta$ lead to corresponding tune shifts. In the LHC, the first-order chromaticity is controlled by dedicated sextupole magnets.

### 2.1.2. Dispersion and off-momentum transverse dynamics

The beam particles do not have the same momentum, but are characterised by a small spread around the design value $p_0$:

$$p = p_0(1 + \delta) \tag{2.23}$$

where $\delta$ is the momentum variation and is defined as:

$$\delta = \frac{p - p_0}{p_0} \tag{2.24}$$

Recalling Eq. 2.3, a small variation in momentum causes a proportional change in the angular kick of a dipole magnet:

$$\theta = \frac{qB}{p} = \frac{qB}{p_0(1 + \delta)} \approx \theta_0(1 - \delta) \tag{2.25}$$

Particles with $\delta>0$ (momentum larger than the nominal one) are bent less than the ideal particle, while those with $\delta < 0$ (momentum lower than the nominal one) are bent more. This effect is known as *dispersion*, it is produced by dipole magnets and causes particles with different momentum to have different closed orbits along the accelerator.
In the transverse plane, a momentum offset leads to a distortion of the closed orbit around which the particles perform betatron oscillations.
For small deviations in momentum, the horizontal Hill's equations becomes inhomogeneous:

$$x'' + K(s)x = \frac{\delta}{\rho(s)} \tag{2.26}$$

The solution of this equation is:

$$x(s) = x_\beta(s) + x_\delta(s) \tag{2.27}$$

where $x_\beta$ is the betatron oscillation around the on-momentum orbit and $x_\delta$ is the particular solution of the inhomogeneous equation associated to the momentum variation. It can be written as:

$$x_\delta = D(s)\delta \tag{2.28}$$

where D(s) is the *dispersion function* that satisfies the equation:

$$D'' + K(s)D = \frac{1}{\rho(s)} \tag{2.29}$$

The dispersion is usually negligible in the vertical plane, since it is produced by dipole magnets, which mainly act in the horizontal plane.
As a consequence, the horizontal beam size depends on both the betatron motion and the dispersion, as follows:

$$\sigma_x = \sqrt{\epsilon_x \beta_x(s) + (D_x(s)\frac{\Delta p}{p_0})^2} \tag{2.30}$$

## 2.1.3. Collimation theory

### 2.1.3.1. Geometrical and dynamic aperture

In an accelerator ring, the particle beam is confined inside a physical space defined by the vacuum chamber and by other elements installed along the machine. This region is called *geometrical aperture* $A_{geo}$. The aperture is typically expressed in units of the beam size. For a generic transverse plane $z = (x, y)$, the beam size $\sigma_z$ is expressed by 2.30.
In order to ensure that the particle beam remains within the vacuum chamber, at any position of the machine the maximum transverse oscillation amplitude must be lower than the geometrical aperture.
A particle is lost when its oscillation amplitude is larger than the available aperture, so

when the condition below is fulfilled:

$$A_z(s) \geq A_{geo}(s)\sigma_z(s) \tag{2.31}$$

The concept above refers to the physical limits of the machine. In addition to this physical aperture constraint, the *dynamic aperture* defines the region in phase-space where particle motion is stable. It defines the maximum oscillation amplitude up to which particles remain confined indefinitely. However, in a real accelerator, non-linear magnetic fields (such as sextupoles, octupoles and alignment errors) can cause the particle amplitudes to exceed this stability limit.

### 2.1.3.2. Beam halo population

In an ideal accelerator, beam core particles perform stable motion with oscillation amplitude $A << A_{geo}$. However, there are several processes that can cause particles to move away from the core, leading to the formation of the beam halo.
The population of the beam halo is dangerous for accelerator operation. Far from the beam core, magnet non-linearities become more relevant and can cause particles to have an unstable motion, increasing the risk of beam halo losses in the machine.

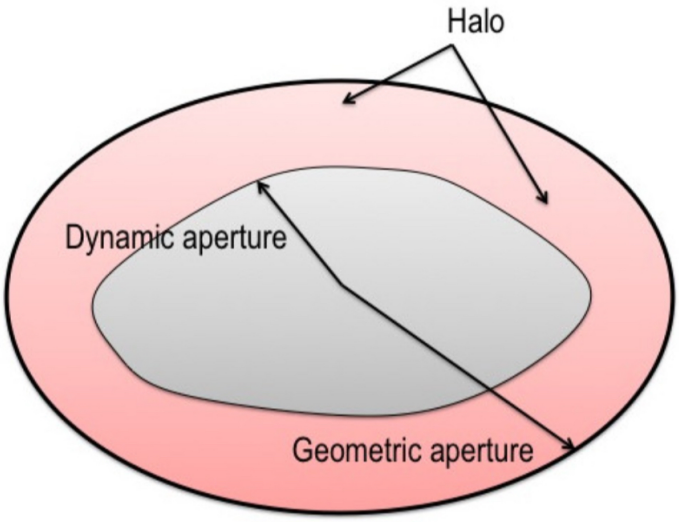


Figure 2.4: Geometric and dynamic aperture.

The main processes that cause the beam halo population and the emittance growth of the circulating beam are:

- Intrabeam scattering: the beam particles are deflected by small angles due to Multiple Coulomb sattering between particles in the same bunch.
- Beam-gas interaction: elastic and inelastic scattering between beam particles and gas molecules inside the vacuum chamber can lead to the population of beam halo.
- Beam-beam effects: after the bunches collide, elastically particles can populate the beam halo, leading to a decrease of luminosity.

If halo particles hit the machine components, they can deposit large amounts of energy, causing radiation damage and reducing the lifetime of impacted components.
Energy deposition in superconducting magnets can lead to quenches, leading to a transition from superconducting to resistive state. Moreover, halo particles can contribute to background in high-energy physics experiments, which can interfere with detector measurement.
Therefore, an efficient collimation system is required, with the main objective of ensuring that particles are lost in robust locations.

#### 2.1.3.3. Collimation cleaning performance

Collimators are blocks of material, called *jaws*, placed between the circulating beam and the mechanical aperture of the accelerator. The distance between the beam center and the surface of each jaw is the *half gap*, which is usually expressed in units of beam size $\sigma$, and defines the *collimator setting*.
The choice of the collimator setting is essential: the outer limit of the settings is determined by the machine aperture that must be protected and by the cleaning performance that needs to be reached. In accelerators with high brightness beams, the inner limit is instead constrained by the contribution of collimators to machine impedance, that can lead to beam instabilities, and, when operating at very small gaps, by the increased loss rates in the collimators themselves.
Therefore, the choice of collimators settings normally results from a trade-off between reaching a sufficient cleaning performance and minimizing the contribution to machine impedance.
To achieve the required cleaning performance, the LHC collimation system is designed as a multistage system, where halo particles are intercepted in successive stages. This configuration relies on a well-defined hierarchy among collimators, which ensures that particles are efficiently absorbed at the intended stage and do not reach sensitive machine components. A detailed description of the LHC multistage collimation system is provided in Section 2.2.2.

Different parameters are defined to quantify the collimation cleaning performance.
The first parameter to be mentioned is the *Global cleaning Inefficiency*, which is defined as:

$$\eta_g(A_i) = \frac{N_p(A > A_1)}{N_{abs}} \tag{2.32}$$

where $N_p$ is the number of particles escaping the cleaning insertion with a betatron oscillation amplitude $A$ larger than an amplitude $A_i$, and $N_{abs}$ is the total number of particles absorbed in the collimation system.
The smaller the Global cleaning inefficiency $\eta_g(A_i)$, the more efficient the cleaning system is.
Another important parameter is the *Local Cleaning Inefficiency*, which provides the distribution of the losses around the ring and is defined as:

$$\eta_c = \frac{N_{loss}}{\Delta s N_{abs}} \tag{2.33}$$

where $N_{loss}$ are the number of particles that are lost over a length of $\Delta s$.
In addition to providing a general protection of the machine, the goal of the collimation system of the LHC is to keep losses in the superconducting magnets below the quench limit. To avoid magnet quenches, the value of $\eta_c$ must fulfill the following condition:

$$\eta_c < \frac{R_q \tau}{N_{tot}} \tag{2.34}$$

where $R_q$ is the quench limit in units of particle lost per metre, $\tau$ is the beam lifetime and $N_{tot}$ is the total beam intensity. Considering $I(t)$ the beam intensity, the beam lifetime can be expressed as:

$$\frac{1}{\tau} = \frac{1}{I}\frac{dI}{dt} \tag{2.35}$$

Therefore, $\tau$ is the characteristic time at which the beam intensity reduces to $1/e$ of its initial value.

### 2.1.4. Impedance

When a high-intensity beam travels through the accelerator, it induces electromagnetic fields in the surrounding vacuum chamber. These fields act back on the beam, and

can influence its longitudinal and transverse motion. This interaction is known as beam impedance. Two main mechanisms contribute to impedance: the geometric contribution, generated by discontinuities or variations in the aperture of the vacuum chamber, and the resistive wall-impedance, which arises from the finite conductivity of the materials. The impedance can drive collective effects that can lead to emittance growth and beam instabilities.
In the LHC, collimators are the main contributors to impedance because of their small gaps around the circulating beam. Higher electrical conductivity jaw materials help reduce the impedance, but the tight apertures required for the efficient halo cleaning still make the collimation system the main machine impedance contributor.

## 2.2. The LHC and its collimation system

The primary goal of the LHC was to discover the last missing piece of the Standard Model, the Higgs boson, whose existence was confirmed in 2012, after only a few years of operation.
Today, the LHC aims to explore new physics beyond the Standard Model, trying to explain several phenomena observed in nature that remain unsolved, such as the matter-antimatter asymmetry.
Two counter-rotating beams circulate along two parallel vacuum pipes, bent and focused by superconducting magnets cooled to 1.9 K in a bath of superfluid helium. The beams collide at four interaction points (IPs), where the main experiments are located: ATLAS, ALICE, CMS and LHCb.

### 2.2.1. The LHC accelerator complex

The LHC is the last of a complex accelerator chain. Protons are initially taken from a hydrogen source, where they are extracted at an energy of about 50 keV. They are then accelerated in the 35 metre long Linear Accelerator (LINAC), reaching an energy of 160 MeV. After that, the beam is injected into the Proton Synchrotron Booster (PSB), which increases the energy to 2 GeV. From there, the particles are transferred to the Proton Synchrotron (PS), where they are grouped into trains of bunches with 25 or 50 ns spacing and accelerated to 26 GeV. Finally, the protons are sent to the Super Proton Synchrotron (SPS), where they reach 450 GeV before being injected into the LHC [12].
The LHC is composed of eight sections, called Interaction Regions (IRs), and eight arcs. The particle beams collide at four Interaction Points (IPs), where the detectors are placed. The two general purpose experiments are ATLAS (A Toroidal LHC ApparatuS, *IP1*) and

Table 2.1: Main LHC design parameters (at injection and collision) and main LHC parameters during 2025 operation [10] [14].

| **Parameter** | **Injection** | **Design Collision** | **Collision (2025)** |
|---|---|---|---|
| **Beam data** | | | |
| Energy [GeV] | 450 | 7000 | 6800 |
| Relativistic gamma | 479.6 | 7461 | 7250 |
| Number of particles per bunch [$10^{11}$] | 1.15 | | 1.62 |
| Number of bunches | 2808 | | 2460 |
| Transverse normalized emittance [$\mu$m rad] | 3.5 | 3.75 | 2.50 |
| Circulating beam current [A] | 0.582 | | 0.72 |
| Stored energy per beam [MJ] | 23.3 | 362 | 434 |
| **Peak Luminosity Related Data** | | | |
| Peak luminosity [$10^{34}$ cm$^{-2}$ s$^{-1}$] | – | 1.0 | 2.25 |
| **Geometry** | | | |
| Ring circumference [m] | 26658.883 | | |
| **Magnets** | | | |
| Number of main dipoles | 1232 | | |
| Field of main dipoles [T] | 0.535 | 8.33 | 8.09 |
| Bending radius [m] | 2803.95 | | |


Figure 2.5: The Large Hadron Collider on the Swiss-French border.

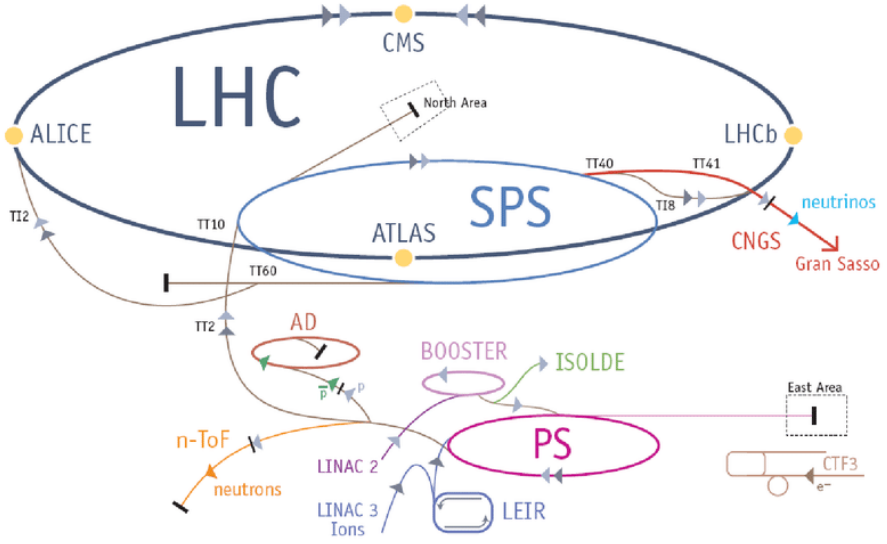


Figure 2.6: Accelerator complex at CERN [12].

CMS (Compact Muon Solenoid, *IP5*). LHCb (Large Hadron Collider beauty, *IP8*) is dedicated to the study of B-meson decays and ALICE (A Large Ion Collider Experiment, *IP2*) is optimized for heavy ion collisions. The two counter-rotating beams are injected to the machine in IR2 (*Beam 1*) and IR8 (*Beam 2*), and are consequently accelerated

by RF cavities installed in IR4. The beam dumping system is located in IR6, where the beams are safely extracted from the accelerator. IR3 and IR7 insertions are dedicated to momentum and betatron cleaning, respectively.
When the two counter-rotating beams collide at the interaction points, a large number of collisions occur per unit time. This rate of interaction is quantified by the *Reaction Rate* $R$ and depends on both the cross-section $\sigma$ and the luminosity $\mathcal{L}$:

$$R = \sigma\mathcal{L} \tag{2.36}$$

The cross-section represents the probability that a specific reaction occurs and depends only on the physics process and on the beam energy. Luminosity $\mathcal{L}$ is, instead, a beam-specific parameter and is defined as:

$$\mathcal{L} = \frac{f_{rev} n_b N_b^2}{4\pi\sigma_x\sigma_y} F, \tag{2.37}$$

where $N_b$ is the number of particles per bunch, $n_b$ is the number of bunches per beam, $f$ is the revolution frequency, $\sigma_x$ and $\sigma_y$ are the rms transverse beam sizes at interaction points and $F$ is the geometric reduction factor accounting for the crossing angle that is imposed to the colliding bunches to avoid parasitic collisions around the IP.
As shown in Eq. 2.37, luminosity depends on the beam parameters of the collider. In general, the goal is to maximize it to increase the collision rate. This improves the probability of observing rare events and provides a higher statistical significance.
In 2011, with a beam energy of 3.5 TeV, the LHC reached a peak luminosity of $4 \times 10^{33}\text{cm}^{-2}\text{s}^{-1}$. In 2012, operating at 4 TeV, the peak luminosity increased to $7.7 \times 10^{33}\text{cm}^{-2}\text{s}^{-1}$, still below the design value of $10^{34}\text{cm}^{-2}\text{s}^{-1}$, but sufficient to produce enough events for the discovery of the Higgs Boson.
In Run 2 (2015-2018), the LHC exceeded its designed luminosity. After reaching the nominal value of $1 \times 10^{34}\text{cm}^{-2}\text{s}^{-1}$ in 2016, the machine achieved a peak luminosity of $2.07 \times 10^{34}\text{cm}^{-2}\text{s}^{-1}$ in 2018, more than twice the design target [25]. Run 3 (2022-present) reached a peak luminosity of approximately $2.1 \times 10^{34}\text{cm}^{-2}\text{s}^{-1}$ in 2024, confirming the excellent performance achieved during Run 2 [17].

### 2.2.2. Collimation system of the LHC

The collimation system has multiple roles, such as cleaning of the betatron and off-momentum beam halos, providing passive machine protection and intercepting the collision products. The first step in designing an effective collimation system is to identify

the main objective it has to fulfill. For the LHC, the main design requirement is the cleaning of halo particles, in order to keep the particle losses below the quench limit of the superconducting magnets.
Indeed, the LHC operates with high stored beam energy (450 MJ at 6.8 TeV) which, on the one hand, represents the extraordinary potential of the accelerator, but, on the other hand, makes the beam highly destructive.
The superconducting magnets would quench even if a small amount of energy (about $30\text{mJ/cm}^3$) is deposited in the superconducting coils. Therefore an efficient collimation system is required to intercept and absorb the beam losses in a safe and controlled way.

#### 2.2.2.1. The LHC collimator design

The LHC collimators consist of two blocks of materials, called *collimator jaws*, which are independently movable. Their relative position defines the gap through which the beam passes. The surface of each jaw consists of a flat part, which defines the active length, and a tapering part at both ends to minimize its contribution to the machine impedance. The collimator jaws must be precisely centered and aligned with respect to the beam envelope and the actual beam orbit. The jaw aperture and the tilt angle are adjusted by four stepper motors installed on each collimator.
The two collimator jaws are put in a vacuum tank. The cooling of the jaws is provided by a heat exchanger with metallic pipes. The mechanical stress caused by the contact between materials with different thermal expansion coefficients (the jaws and the heat exchanger) is mitigated by means of a GlidCop support bar, a copper alloy containing finely dispersed alumina particles. This bar presses the cooling pipes against the jaw material through clamping elements. This design also improves the thermal contact between the two components.
Fig 2.8 shows the original LHC collimator design, where the GlidCop support bar is pressed against the cooling pipes by springs. The same mechanical principle is still employed today, but the clamping system uses screws instead of springs [11].
Depending on their orientation with respect to the beam axis, collimators can be horizontal, vertical or skew.
One important aspect in the design of collimators is the choice of the jaw material. The jaw material depends on the role of the collimator in the system hierarchy, as will be discussed in the next section. In general, high-Z and high-density materials, such as tungsten, are preferred if the main purpose of the collimator is absorption of particles, since they provide a high interaction probability. Low Z materials, such as graphite, are preferred instead to reduce energy deposition in the jaw and to ensure higher robustness

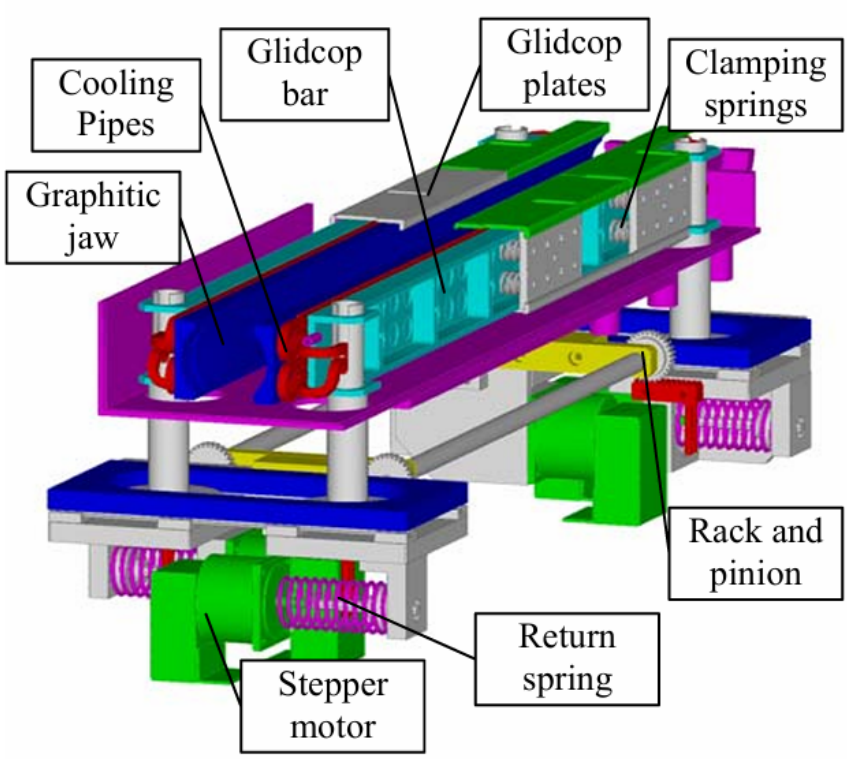


Figure 2.7: LHC Collimator scheme [5].

in case of beam impacts.
For the LHC, most primary and secondary collimators are made of fiber-reinforced graphite (CFC). However, in IR7 some primary collimators have been upgraded to Molybdenum Graphite (MoGr) to reduce impedance. Some secondary collimators have also been replaced with MoGr jaws [1].
Absorbers are made of high Z materials to maximize particle absorption.
The choice of the jaw material also affects the beam impedance. Materials with high electrical conductivity, such as copper or tungsten, help reduce the impedance, but are less robust against beam impacts. Materials with low electrical conductivity, such as CFC, are more robust against mechanical damage but contribute more to the machine impedance.

#### 2.2.2.2. The multi-stage collimator system of LHC

The LHC collimation system is a multi-stage system whose main goal is to intercept and absorb beam losses.
One of the key aspects of a multi-stage collimation system is a well-defined collimator hierarchy, which ensures that each collimator performs its specific function in the overall

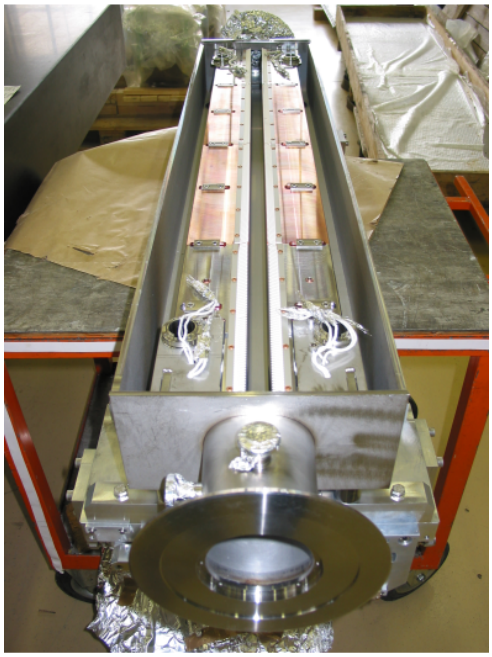

Figure 2.8: Top collimator view [13].

cleaning process.
The aperture of the collimator is expressed in units of the standard deviation of the beam in the collimator plane, which for a plane $i$ is defined as:

$$\sigma_i = \sqrt{\beta_{x,i}\epsilon \cos^2\theta_i + \beta_{y,i}\epsilon \sin^2\theta_i} \tag{2.38}$$

where $\beta_{x,i}$ and $\beta_{y,i}$ are the betatron functions, $\theta_i$ is the tilt angle of the $i$-th collimator, and $\varepsilon$ the geometrical emittance, resulting from $\varepsilon = \varepsilon_n/\gamma_{\text{rel}}$, with $\varepsilon_n = 3.5$ $\mu$m rad the normalized emittance at 6.8 TeV. It is important to note that, in this context, the beam size is defined only by the betatron contribution. The dispersive term is not included, therefore this expression 2.38 does not represent the RMS beam size.

Fig 2.9 shows three different orientations of collimator jaws in the transverse plane.
The angle $\theta$ defines the rotation of the collimator jaws with respect to the horizontal axis $x$.
For an horizontal collimator, the jaws are parallel to the $x$ axis ($\theta = 0°$), for a vertical collimator the jaws are parallel to the $y$ axis ($\theta = 90°$) and for a skew one, the jaws are tilted by an angle $\theta$ with respect to the $x$ axis.
Therefore, in Eq 2.38, $\sigma$ is the transverse beam size along the collimator orientation.
The setting of the collimator jaw is usually expressed in unit of $\sigma$ and the jaws of a collimator are set at $\pm n\sigma$ from the beam center.

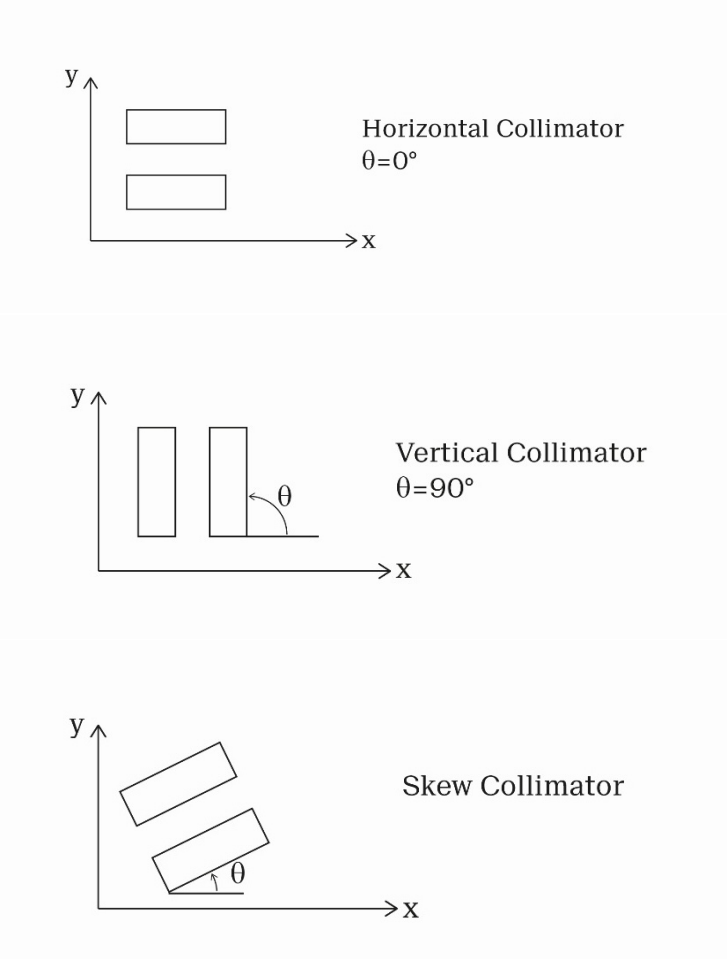


Figure 2.9: Schematic representation of three collimator orientations in the transverse plane.

Different $n$ values are assigned to different collimators to ensure the cleaning hierarchy. The LHC houses two dedicated insertions for beam cleaning: the betatron cleaning and the momentum cleaning insertions. The first captures particles with high betatron amplitudes, while in the second particles with large momentum deviations are cleaned. The two insertions are located in two different regions of the LHC ring and are designed to independently perform their tasks.

- *Betatron cleaning insertion* (IR7): region with small dispersion, meaning that the transverse displacement due to momentum offset is negligible. Particles located far from the beam center are characterized by large betatronic amplitudes.
- *Momentum cleaning insertion* (IR3): region with large dispersion, so the halo particles are characterized by a high momentum offset. Due to optical constraints, the beta function is not negligible in this region.

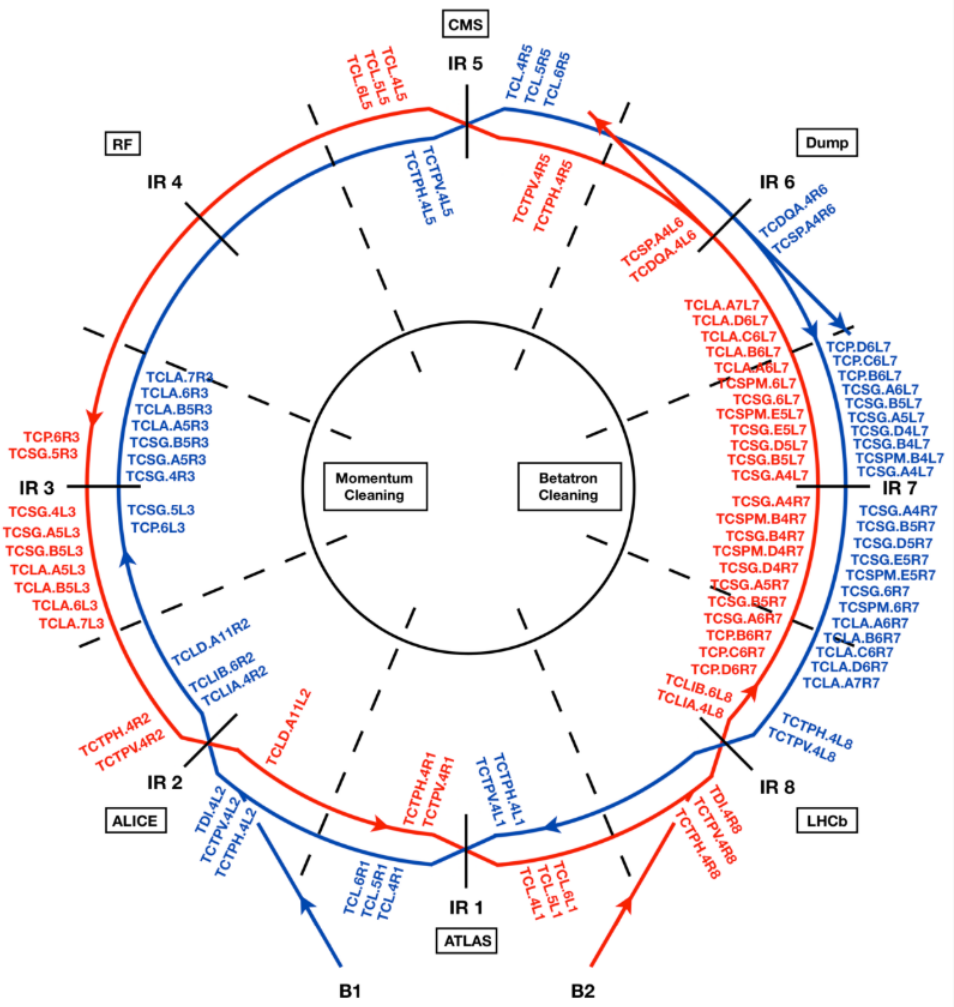


Figure 2.10: Collimation layout of the LHC [4].

A multi-stage collimation system is implemented in both the betatron cleaning and momentum cleaning insertions.

The primary collimators (TCP, 'target collimator,primary') are the first collimators

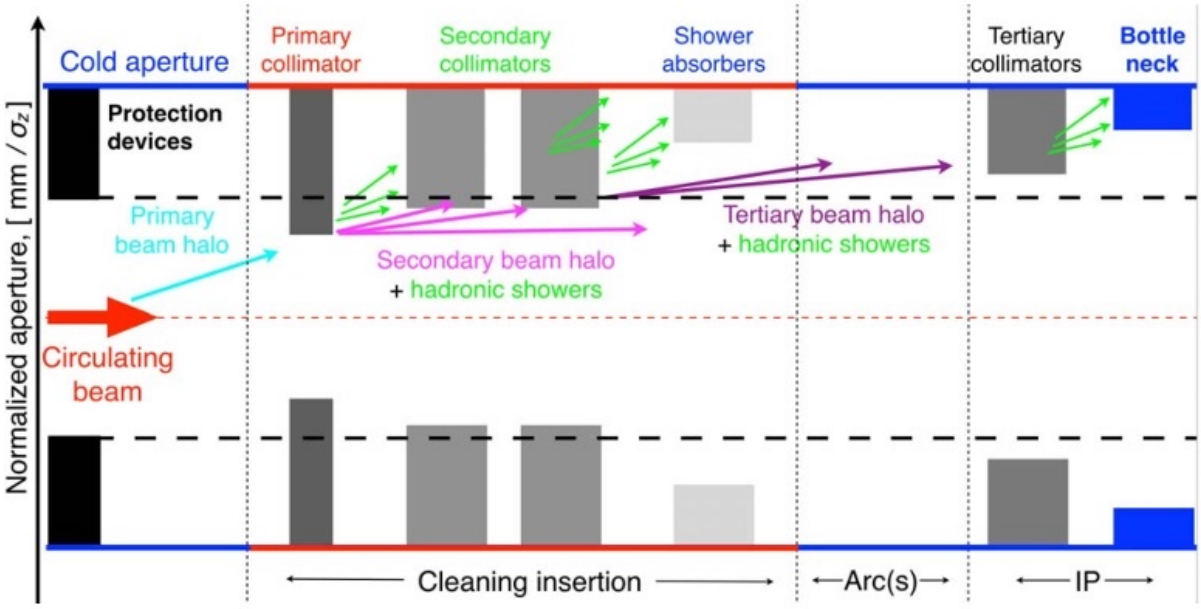


Figure 2.11: LHC multistage collimation system [24].

placed along the beam path, designed to intercept the primary beam halo particles.
Downstream, secondary collimators (TCS, 'target collimators, secondary') are placed, with the specific role of intercepting the particles that are out-scattered at TCPs, called secondary halo. TCSs are longer than TCPs to maximize the interception of secondary beam halo. Their aperture is larger than the one of TCPs, in order to ensure the collimator hierarchy.
These two types of collimators are made of Molibdenum-Graphite (MoGr), Mo-coated Molibdenum-Graphite or Carbon Fibre Composite (CFC), materials that provide high robustness and increase thermal conductivity, reducing the contribution to machine impedance.
The primary collimators have an active length of 60 cm, the secondary collimators of 1 m.
Further downstream, absorbers called TCLA are installed to absorb the tertiary beam halo and the particle showers produced by inelastic interactions of the protons in upstream collimators. These collimators have a larger aperture than secondaries and are made of Inermet180, a high-density tungsten alloy, to maximize the particle absorption rate.
While the collimators described above perform the cleaning function of the LHC, additional collimators are installed in particularly sensitive areas of the ring. Their role is to protect the machine from beam losses that could result from equipment failures or

operational errors.
The Target Dump Injection Segments (TDIS) are vertical collimators equipped with 4.2 m long Cu-coated graphite jaws. They are installed to prevent the failure of one or more injector kickers. In these cases, the upper jaw intercepts bunches that are not sufficiently deflected by the kickers, while the lower jaw intercepts a miskicked circulating beam. In addition, two-sided vertical collimators (TCLIs) are placed downstream of the LHC injection points, in IR2 for *Beam 1* and IR8 for *Beam 2*. These collimators are moved in during the beam injection and are retracted before the acceleration phase starts.
In IR6, a dump protection system is installed and is composed of three collimators, called TCDQ, followed by a secondary collimator (TCSPM). Each TCDQ is a one-sided horizontal collimator 3 m long, resulting in a total active length of 9 m. This system protects the machine in case of malfunction of the beam extraction system.
In addition, two tertiary collimators (target collimators, tertiary, pick-up, TCTPs) are installed upstream of the collision points for all the experiments, one TCTP in the horizontal plane (TCTPH) and one in the vertical plane (TCTPV). Their primary function is to protect the quadrupole triplets that squeeze the beams before they go into collision [23]. In addition, TCTPs also contribute to background mitigation: by intercepting halo particles, they can reduce the background in the experimental detectors. However, when protons interact with the jaw material, the particle showers that are generated may still reach the experiments. They are two-sided collimators with 1 m Inermet180 jaws.
Downstream of the two high luminosity experiments, in IR1 and IR5, physics debris absorbers (target collimator, long TCL) are installed to protect the machine from particle showers coming from the collisions.
The collimators described above are placed inside the beam vacuum, which intercept beam particles. In addition to them, masks, absorbers and other shielding elements are installed outside the beam vacuum to further protect the magnets and the experimental areas.

| Position (IR) | Name | Collimator type | Material | Half-gap [$\sigma$] (collision) | Half-gap [$\sigma$] (flat top) |
|---|---|---|---|---|---|
| IR7 | TCP | Primary | Mo-Gr/CFC | 5.0 | 5.0 |
| | TCSG | Secondary | CFC | 6.5 | 6.5 |
| | TCSPM | Secondary | Mo-Gr | 6.5 | 6.5 |
| | TCLA | Absorber | IT-180 | 10.0 | 10.0 |
| IR3 | TCP | Primary | Mo-Gr/CFC | 15.0 | 15.0 |
| | TCSG | Secondary | CFC | 18.0 | 18.0 |
| | TCLA | Absorber | IT-180 | 20.0 | 20.0 |
| IR6 | TCDQ | Dump protection | graphite | 7.3 | 7.3 |
| IR1 | TCTH | Tertiary (H) | IT-180 | 8.5 | 18.0 |
| | TCTV | Tertiary (V) | IT-180 | 8.5 | 18.0 |
| IR2 | TCTH | Tertiary (H) | IT-180 | 37.0 | 37.0 |
| | TCTV | Tertiary (V) | IT-180 | 37.0 | 37.0 |
| IR5 | TCTH | Tertiary (H) | IT-180 | 8.5 | 18.0 |
| | TCTV | Tertiary (V) | IT-180 | 8.5 | 18.0 |
| IR8 | TCTH | Tertiary (H) | IT-180 | 11.5 | 18.0 |
| | TCTV | Tertiary (V) | IT-180 | 11.5 | 18.0 |

Table 2.2: Collimator settings expressed in units of beam size $\sigma$ at 6.8 TeV for collision and flat-top configurations (2025).

## 2.3. The HL-LHC upgrade challenges

To extend its discovery potential, the LHC will undergo an upgrade to achieve unprecedented luminosity levels with the High-Luminosity LHC (HL-LHC) project.
Run 1 and Run 2 have been completed by the LHC and its experiments since it came into operation in 2011, Run 3 is still ongoing at the time of this thesis.
Each Run is separated by a Long Shutdown (LS) period, during which the accelerator complex and the experiments are maintained and upgraded. The final steps of the HL-LHC upgrade will take place during LS3 from 2026 to 2030, in parallel with the ATLAS and CMS upgrades.
Over the years, the LHC has increased both its collision energy and luminosity.
In Run 2 the instantaneous luminosity increased to about $2 \times 10^{34}\text{cm}^{-2}\text{s}^{-1}$ and an integrated luminosity of 190 fb$^{-}$1 was reached [9]. The present Run 3, currently operated at a beam energy of 6800 TeV, is expected to deliver approximately 350 - 400 fb$^{-}$1 [9].
The HL-LHC aims to reach the following luminosity targets:

- A peak luminosity of $5 \times 10^{34} cm^{-2} s{-}1$ with levelling [9].
- An integrated luminosity of 250 $fb^{-1}$ per year, with the goal of 3000 $fb^{-1}$ in about 12 years after the upgrade. This value is about ten times the luminosity reach of the LHC in its first twelve years [9].

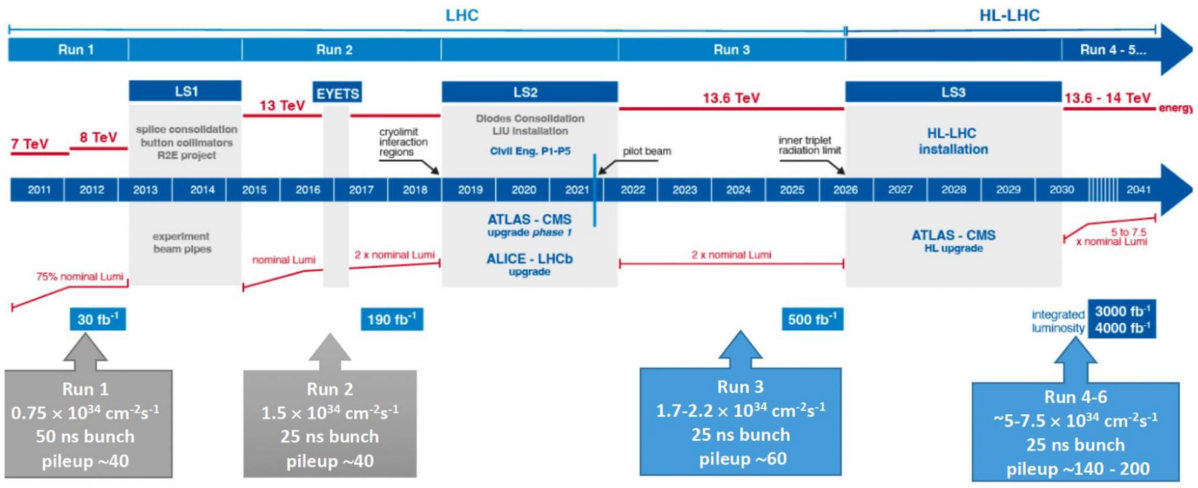


Figure 2.12: LHC and HL-LHC plan including Runs and Long Shutdowns (LS).

The general expression of the instantaneous luminosity was introduced in Eq. 2.37. Assuming round beams, it can be re-written as:

$$\mathcal{L} = \frac{n_b N^2 f_{rev} \gamma}{4\pi \epsilon_n \beta^*} F \tag{2.39}$$

A key factor to increase the luminosity is the bunch intensity $N$, which in the HL-LHC project will be increased from $1.15 \times 10^{11}$ to $2.2 \times 10^{11}$ for proton beams. Another strategy to maximize the luminosity is reducing the $\beta^*$, which is the $\beta$ function at the collision points (IPs).
In principle, also the number of bunches $n_b$ could be consider a parameter to be increased. In practice, there are several aspects that limit its significant increase. For example, there is a minimum bunch spacing (25 ns) at the interaction point that the detectors can handle and there is also a maximum number of bunches that can be safely transferred from SPS to LHC.
The geometric reduction factor F can also be optimized to increase the luminosity.
In the following Tab the main parameters for the High Luminosity LHC for proton beams is shown:

| **Parameter** | **Nominal** LHC | **Nominal HL-LHC** |
|---|---|---|
| Beam energy in collision [TeV] | 7 | 7 |
| Stored beam energy [MJ] | 362 | 700 |
| Particles per bunch | 1,15E+11 | 2,2E+11 |
| Number of bunches per beam | 2808 | 2760 |
| Total beam population [$10^{14}$] | 3.2 | 6.1 |
| Beam current [A] | 0.58 | 1.1 |
| Instantaneous luminosity [$10^{34}$ $cm^{-2}s^{-1}$] | 1 | 5.0 |
| Minimum $\beta^*[m]$ | 0.55 | 0.15 |
| $\epsilon_n$ [$\mu m$] | 3.75 | 2.50 |
| Half-crossing angle in IP1 and IP5 [$\mu rad$] | 142.5 | 250 |
| Peak dipole field of magnets [T] | 8.33 | 11 to 12 |

Table 2.3: Comparison of the design parameters for the LHC and the High-Luminosity LHC

The main hardware upgrades for the HL-LHC project involve:

- Detector upgrades
- Superconducting Magnets: replacement of the inner triplets (IT) quadrupoles with $Nb_3Sn$ superconductors in IP1 and IP5. They will provide a peak field of about 11.5 T and an aperture of 150 mm [9]. The larger aperture is the key upgrade: it allows to increase the crossing angle required to mitigate beam-beam effects from the higher bunch intensity. Furthermore, the larger aperture allows also the accomodation of a larger beam size resulting from the reduced $\beta^*$ at collision. The use of $Nb_3Sn$ is required in order to keep a sufficient focusing gradient with the larger aperture.
- Crab cavities: RF cavities that tilt the bunches with respect to their direction of motion, maximizing the bunch overlap at the interaction point (IRs), and compensating for the geometric reduction factor F [9]. They will be installed in IP1 and IP5.
- Collimators:
  - Secondary collimators: most of secondary collimators have already been updated with Molybdenum-graphite (MoGr) jaws to reduce their contribution to machine impedance, reducing the risk of beam instabilities. Additional Cu-coated MoGr secondary collimators will be installed to achieve an even lower

machine impedance.

- Tertiary collimators: to cope with the new triplet configuration, an additional set of TCTs will be installed in IP1 and IP5, providing effective protection to the inner triplet magnets.
- Crystal collimators: Crystal primary collimators, aimed at improving the cleaning performance during heavy-ion operation, have already been installed.

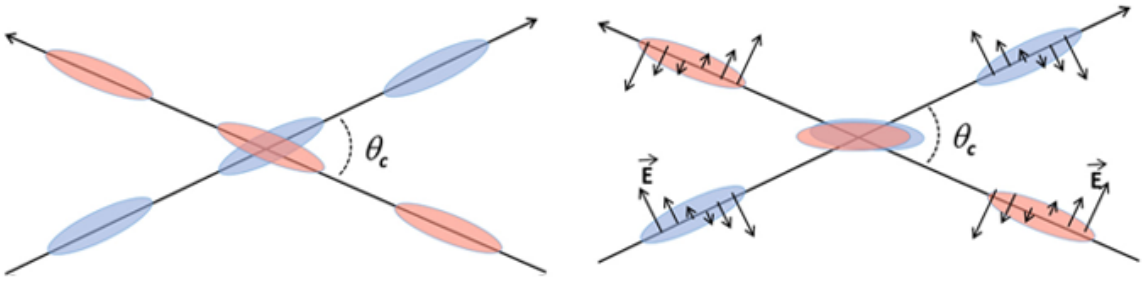


Figure 2.13: Comparison between bunch collision geometries: without crab cavities (left) and with crab cavities (right). [9].

### 2.3.1. Scope of this thesis work within the HL-LHC Project

The HL-LHC will operate with increased beam intensity, raising concerns about leakage of beam losses out of the IR7 collimator insertion to the dispersion suppressor (DS) regions, potentially leading to quenches in the superconducting magnets.
To mitigate this, the installation of collimators in the DS (TCLDs) was originally proposed.
This entailed replacing one main dipole with two shorter 11 T dipoles, in order to create sufficient space to insert the collimator. This plan was however descoped from the baseline due to issues associated with the construction of the new 11 T dipoles [9].
In addition to beam losses, impedance represents another concern for the machine operation with HL-LHC beam intensity, for which collimator jaws account for about half of the total machine impedance. [9].
Some mitigation strategies have already been identified, such as those mentioned above, and are foreseen for the HL-LHC upgrade to reduce the overall impedance contribution of the collimation system.
In order to further mitigate both these two challenges, beam losses and impedance, a new optics configuration for IR7 has been developed. Its design principles, implementation and performance will be discussed in the following chapters.

# 3 | Design of new collimation optics for the energy ramp

## 3.1. Improved optics at top energy

### 3.1.1. Design and constraints of the new IR7 optics

A new optics in the betatron collimation insertion (IR7) for proton beams has been developed to mitigate two already mentioned challenges of the HL-LHC: reduce loss leakage from the collimation system to the downstream superconducting magnets and mitigate the collimator contribution to the machine impedance. An optics is a specific magnet configuration designed to control the beam parameters, such as the $\beta$ function or the dispersion. The main goals of the new IR7 optics are:

- Increase of the beta function at the primary collimators [20]: particles scattered by TCP will receive a larger normalized kick, which scales as $\Delta x'[\sigma] \propto \sqrt{\beta_x}$ and are therefore more likely intercepted by secondary collimators, resulting in an improved collimation performance. The resistive-wall impedance depends on the physical gap $a$ of the collimators, which is given by $a = n\sigma$. Since the beam size scales as $\sigma \propto \sqrt{\beta}$, the impedance follows $Z \propto 1/a^3 \propto \beta^{-3/2}$. Increasing the beta function therefore increases the physical gap for the same collimator setting in units of beam size, which reduces the effective impedance.

- As particles are scattered by the TCP, they generally lose a fraction of their momentum. Downstream of the TCP they will then start to follow a dispersive trajectory, which is determined by the *single pass dispersion* from the TCP and onwards. By increasing the single pass dispersion, off-momentum particles deviate further from the nominal trajectory, which can enhance their likelihood of being intercepted by the downstream collimators, rather than leaking into the arc [20].

The improvements in cleaning and impedance are primarily required at top energy, where the stored beam energy is maximum and the collimator gaps are smallest, leading to a

larger contribution to machine impedance. For this reason, the new IR7 optics is first optimized at top energy.

Two versions of the new IR7 optics considered for operation have been developed for the HL-LHC project. In the first one, only the optics in the IR7 insertion is modified, making its integration relatively transparent. The second version removed the phase advance constraint over the insertion, allowing more flexibility in the optics design and a further improved optics. Removing the phase advance constraint, however, means that the phase change must be compensated for elsewhere in the machine, such as the arcs surrounding the IR7 insertion. As shown in 3.1, the simulated cleaning inefficiency for the two new IR7 optics versions, together with the reference optics configuration with the TCLD collimator installed, is improved compared to the reference optics. In addition, version 2 provides a further reduction of the cleaning inefficiency for Beam 2 in the horizontal plane compared to version 1.

In this thesis, the two circulating beams are denoted as Beam 1 and Beam 2. The notation B1H, B1V, B2H and B2V is used to refer to their horizontal (H) and vertical (V) planes.

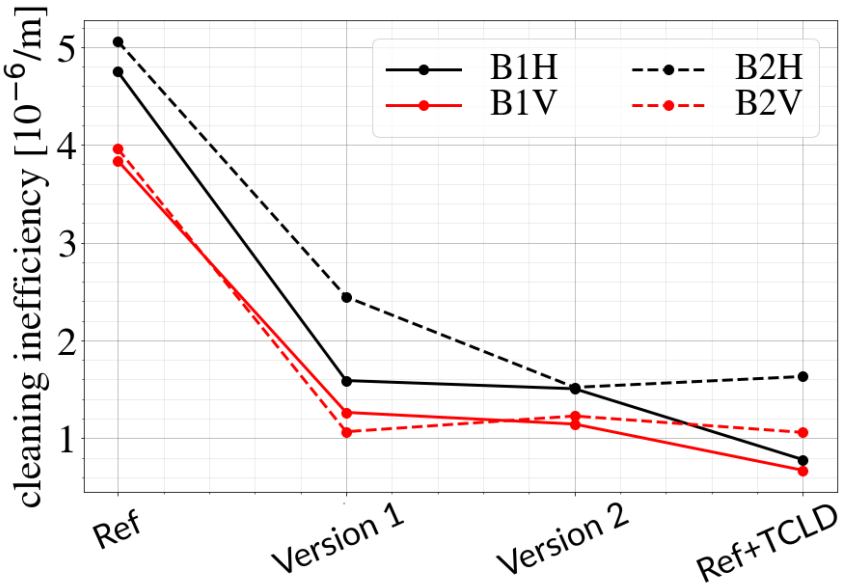


Figure 3.1: Cleaning inefficiency for the reference optics, the two versions of the new IR7 optics and the reference optics with TCLD configuration.

In the present thesis, the first version of the new IR7 optics is analyzed, since it is the one integrated into the LHC operational cycle for 2025.

In order to achieve the new optics configuration, the optics must be rematched, meaning that the currents of the quadrupoles must be varied to obtain the desired optical func-

tions in IR7 insertion. The rematching is performed using quadrupoles located in the IR7 insertion, up to cell 13, including both individually powered magnets , which can be tuned separately for Beam 1 and Beam 2, and quadrupoles on a common power supply, which affect both beams simultaneously.
This procedure has some constraints related to the optics design. First, the optics downstream of IR7 must remain matched to the arc in order to ensure that the optical functions return to the periodic conditions of the arc, keeping continuity with nominal optics. This ensures that the optics change only has a local effect in IR7, without perturbing the global optical configuration of the machine.
Second, the peak of the beta functions must remain reasonably small to avoid aperture limitations and to mitigate the effects of magnetic field errors. In addition to these constraints, the new optics must also respect a limitation on the maximum value of the $\beta$ function at top energy. Although a larger $\beta$ function improves cleaning and reduces impedance, the increase of $\beta$ is ultimately limited by the available aperture.

### 3.1.2. The new work of this thesis on the IR7 Optics Implementation

The new optics defines the target IR7 configuration required at top energy and is provided as the starting point to this work. The task of this part of the thesis is to develop a smooth transition from the reference optics to the new optics.
To determine how this transition can be performed, it is first necessary to assess whether the new optics is compatible with the aperture at injection energy, where the beam size is largest. The aperture in unit of beam size $A_i[\sigma]$ where $i = x, y$ for *Beam 1* and *Beam 2* is shown in Fig. 3.4 and 3.5. It is calculated as:

$$A_x[\sigma] = \frac{x\,[\mathrm{m}] - \Delta_{orbit} - \Delta_{mech}}{\sqrt{\beta_x \epsilon_n \frac{m_p}{E(450\,\mathrm{GeV})}}}, \tag{3.1}$$

where $x$ [m] is the mechanical half-gap in the horizontal plane. $\Delta_{orbit}$ and $\Delta_{mech}$ represent the allowed orbit error and the mechanical tolerance that need to be taken into account and therefore are subtracted from the available aperture. Typical values for these quantities are of the order of 2 mm for the orbit allowance and 1 mm for the mechanical tolerances, although the latter varies from element to element. As shown in Figs. 3.4 and Figs. 3.5, the aperture goes below the threshold (fixed at $12.6\sigma$ [6]), meaning that the beam does not have sufficient aperture at injection energy. As a consequence, the new optics can not be inserted at injection energy. Since $\sigma \propto \frac{1}{\sqrt{E}}$, as the beam energy increases, the

beam size decreases, resulting in a larger available aperture in units of $\sigma$ at higher energy. This means that the new optics need to be inserted during the energy ramp, requiring a combined ramp and "de-squeeze" of the collimation insertion: a delicate and complex procedure which has never been done before at CERN.
There is also an operational motivation for introducing the optics transition during the energy ramp: performing the "de-squeeze" at top energy would require a dedicated IR7 "de-squeeze" phase, which takes time, while carrying it out during the ramp helps to optimize the operational cycle duration.

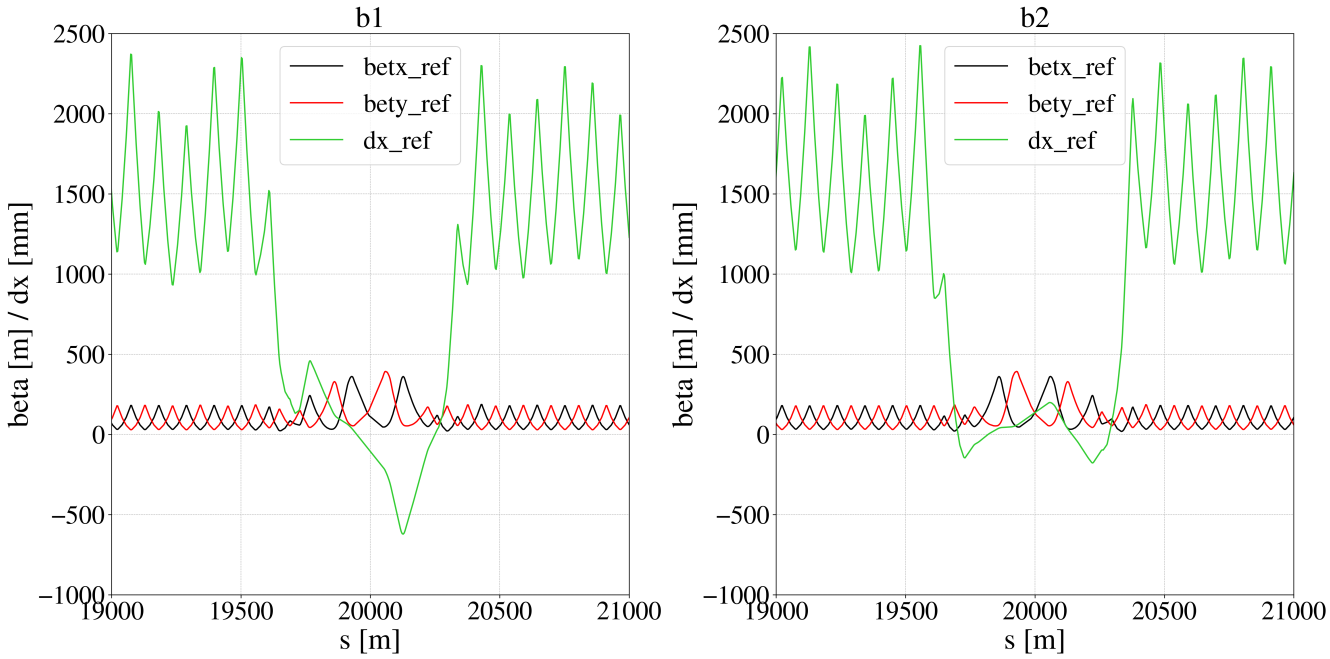


Figure 3.2: Betatron and dispersion functions as function of the longitudinal coordinate $s$ around IR7 for the reference optics (Beam 1 on the left and Beam 2 on the right).

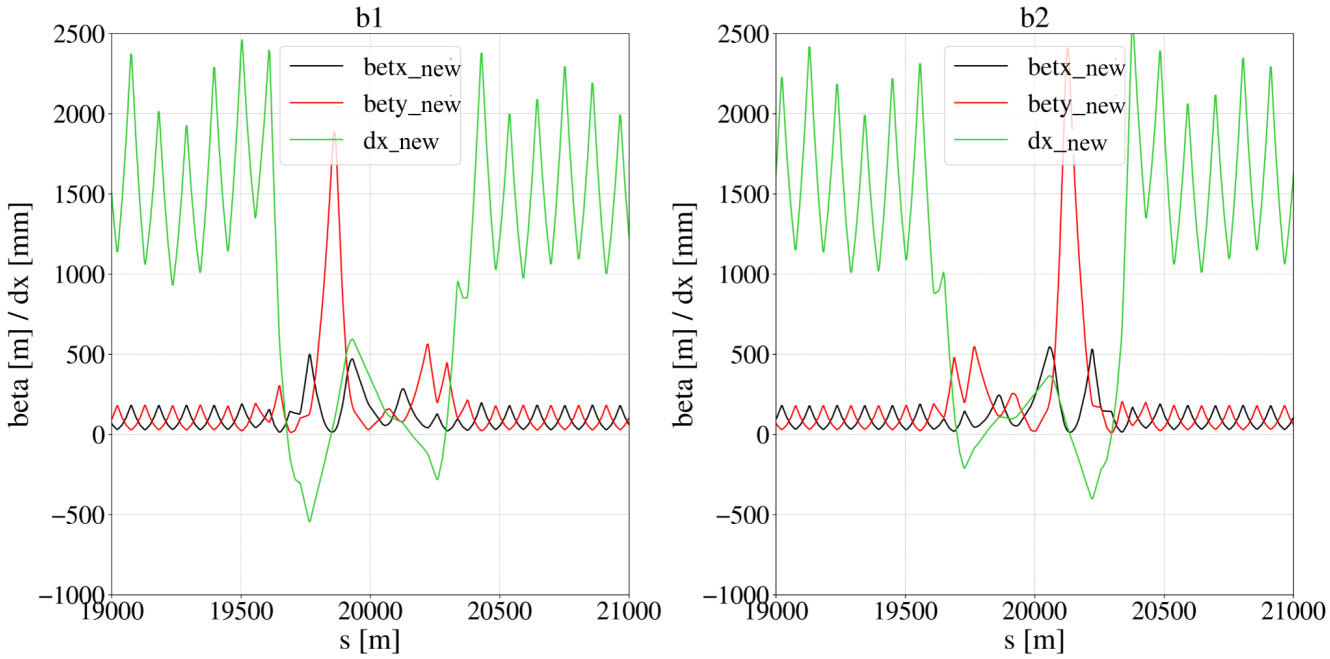


Figure 3.3: Betatron and dispersion functions as function of the longitudinal coordinate $s$ around IR7 for the new IR7 optics (Beam 1 on the left and Beam 2 on the right).

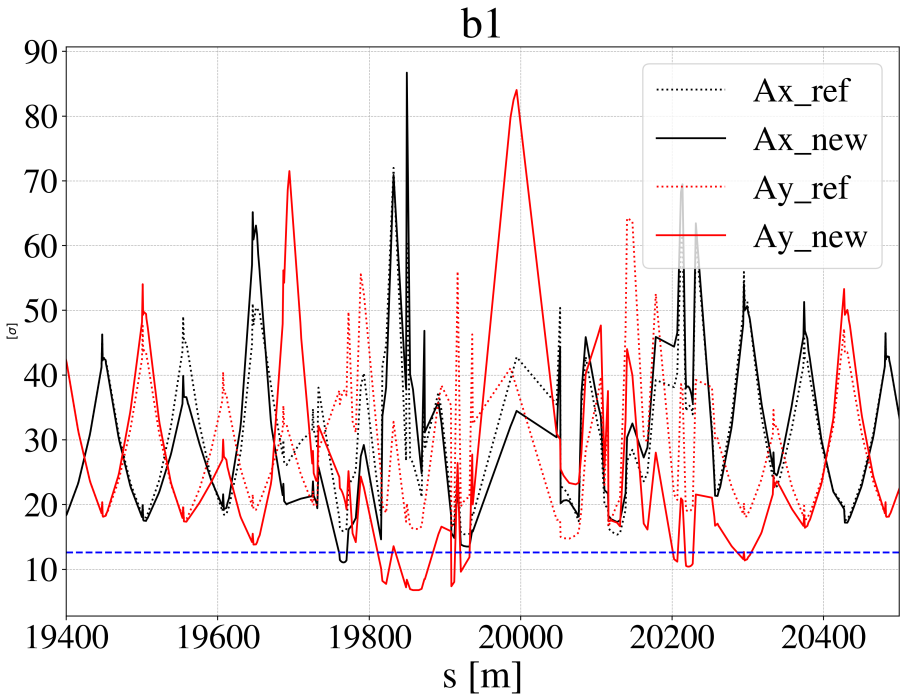


Figure 3.4: Aperture at injection energy for Beam 1 for reference and new optics.

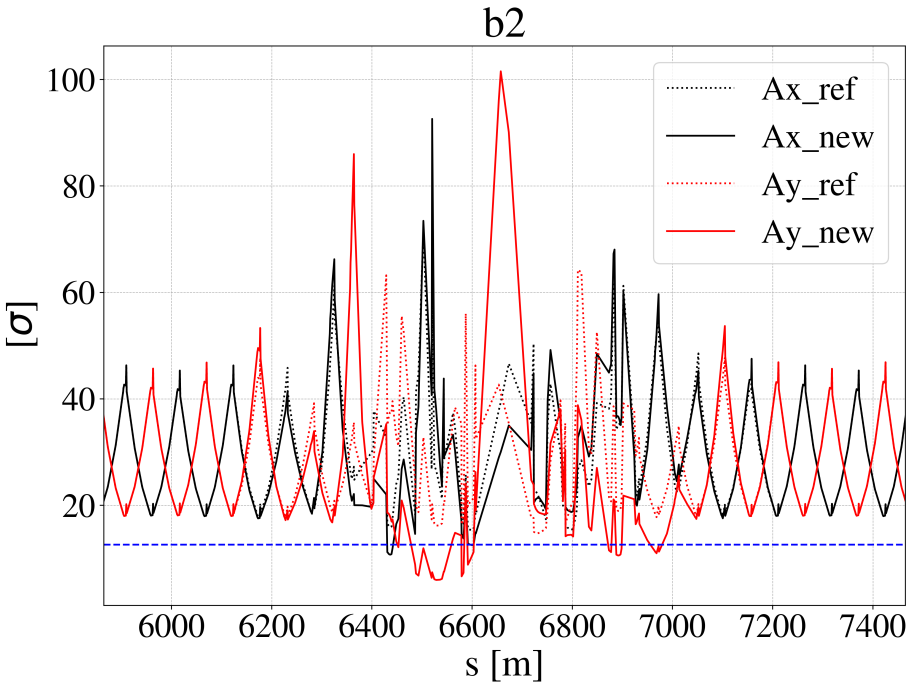


Figure 3.5: Aperture at injection energy for Beam 2 for reference and new optics.

## 3.2. New optics for the LHC 2025 energy ramp

### 3.2.1. Tools developed for the optics matching procedure

While the optimized IR7 optics at top energy has been developed prior to this thesis work and successfully tested at the LHC [19], an optics transition needed to be developed to move from the reference optics, at injection energy, to the new IR7 optics configuration, at top energy. A previous work was based on an optics transition, called "de-squeeze", performed at top energy. This process has, however, some drawbacks. First, as discussed in the previous section, it increases the operational cycle time. Second, carrying out the transition at top energy is considered operationally risky, since it involves delicate collimator movements when the stored beam is maximum. A more elegant solution is to incorporate the "de-squeeze" in the energy ramp, the same strategy adopted for the collision points.

To explain the procedure performed for this development, a description of the tools used is provided below. In developing the optics transition, the match method implemented in Xtrack was used. Xtrack is a Python module included in the Xsuite [18] package, which was developed at CERN for the simulation of beam dynamics in particle accelerators. Xtrack performs single-particle tracking in accelerator beam lines, provides tools to model and simulate accelerator components, compute optics functions and optimize

lattice configurations.
The match module implements a numerical optimizer that adjusts accelerator parameters to satisfy a set of constraints. The user defines the variables to be varied, the so-called *knobs*, that typically involve quadrupole magnet strengths, and a set of desired targets to be achieved, such as the Twiss parameters. For each target, the user defines a tolerance, which represents the maximum acceptable deviation from the desired value. Through iterative calculations, the numerical optimizer minimizes the difference between actual values and desired values. The procedure stops when the difference between the computed and target values is smaller than the specified tolerance for all the targets. At this point, the optimizer returns a new configuration of the variables.
The matching configuration that was used for the following work is:

```
opt=line.match(
    start=[s.ds.l7.b1]
    end=[e.ds.r7.b1]
    init=twref
    targets=[xt.TargetSet(['betx', 'bety', 'alfx', 'alfy', 'dx', 'dpx', 'dy', 'dpy','mux','muy'], value=twref, at=xt.END)],
    vary=knobs_list
)
```

The optimizer is called by the command *line.match()*. The matching is performed using the quadrupoles in IR7 up to cell 13, and the Twiss parameters are matched over the IR7 section delimited by the start *(s.ds.l7.b1)* and the end *(e.ds.r7.b1)* markers, using the Twiss parameters provided by *twref* as initial conditions at the start of the section.
The *TargetSet* defines the optical functions that must match the reference values contained in *twref* at the end of the section ($at = xt.END$) .
The optical functions defined in *TargetSet* are the $\beta$ functions ($\beta_x$, $\beta_y$), the $\alpha$ functions ($\alpha_x$, $\alpha_y$), the phase advances ($\mu_x$, $\mu_y$), the dispersion function ($D_x$, $D_y$) and the derivatives of the dispersion function ($D'_x$ and $D'_y$).
Once the matching setup has been defined, the command:

```
opt.solve()
```

executes the matching procedure.
The optimizer iteratively adjusts the set of variables listed in $knobs\_list$, until the optical functions at the end of the section match the values in *twref*.
The new configuration of knobs is returned to the user by the command:

```
opt.get_knob_values()
```

The optics transition was developed by interpolating the quadrupole strengths between the reference optics at injection energy and the new optics at top energy. The idea is to represent the transition through a parameter $x$ ranging from 0 to 1, where $x = 0$ corresponds to the reference optics and $x = 1$ corresponds to the new optics. First, a linear interpolation between the two sets of quadrupole strengths was performed, shown in Fig. 3.6. Nine evenly spaced intermediate steps are defined, taking the corresponding quadrupole strength at each step, and matching them with the tool described above, ensuring that the optical functions remain matched to the arc optics. In principle, a perfect optic transition would require an infinite number of intermediate steps and each one would need to be matched, which is clearly impractical. On the other hand, taking too few steps would result in large optics errors between two consecutive matched configurations. Therefore, the choice of nine steps was taken as a good balance. As shown in Fig. 3.7, the linear interpolation is not good enough to keep the optics matched during the transition. Following this, a polynomial interpolation of order 3 is done on the knobs matched from the previous step. The intermediate steps are again matched, and a final polynomial interpolation is done on these results. The final interpolation is shown in Fig. 3.8. A good approximation of the matched intermediate optics and a smooth transition from the reference to the new configuration is achieved.

For operational reasons, and to ensure a monotonic change of the optics functions, it is important that the magnet strengths follow smooth and ideally monotonic functions. An example of a non-monotonic transition matching is shown in Fig. 3.9. In this case, to overcome this, the common quadrupoles between Beam 1 and Beam 2 were forced to follow the linearly interpolated curves. Furthermore, instead of applying the global limits to the magnet currents, each knob had an individual limit with a small tolerance around the initial value taken from the interpolation. This helped achieve the well-behaved functions shown in Fig. 3.8.

The LHC energy ramp increases beam energy from 450 GeV to 6.8 TeV in 1275 seconds. Fig. 3.10 shows the evolution of the beam energy as a function of time during the ramp, with $t = 0$ defined at the start of the ramp. The markers indicate the times at which the matched optics configurations are implemented. Therefore, each intermediate optics configuration, or *matched point*, corresponds to a specific time during the ramp. The choice of of these times must satisfy two main requirements. First, the aperture must

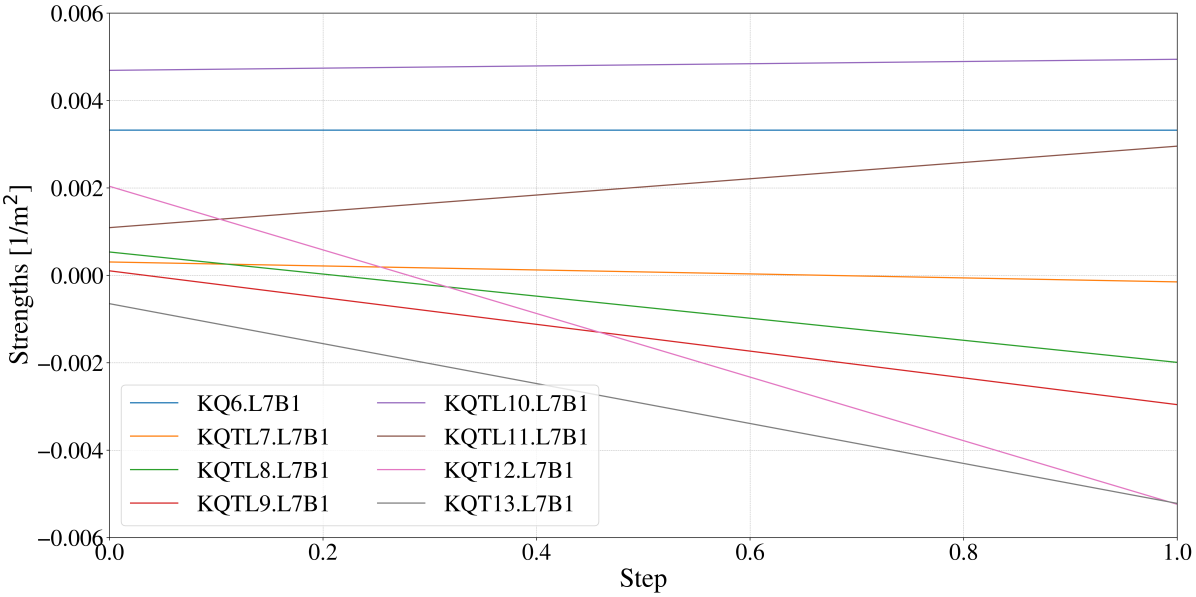


Figure 3.6: Linear interpolation between quadrupole strengths for reference and new optics.

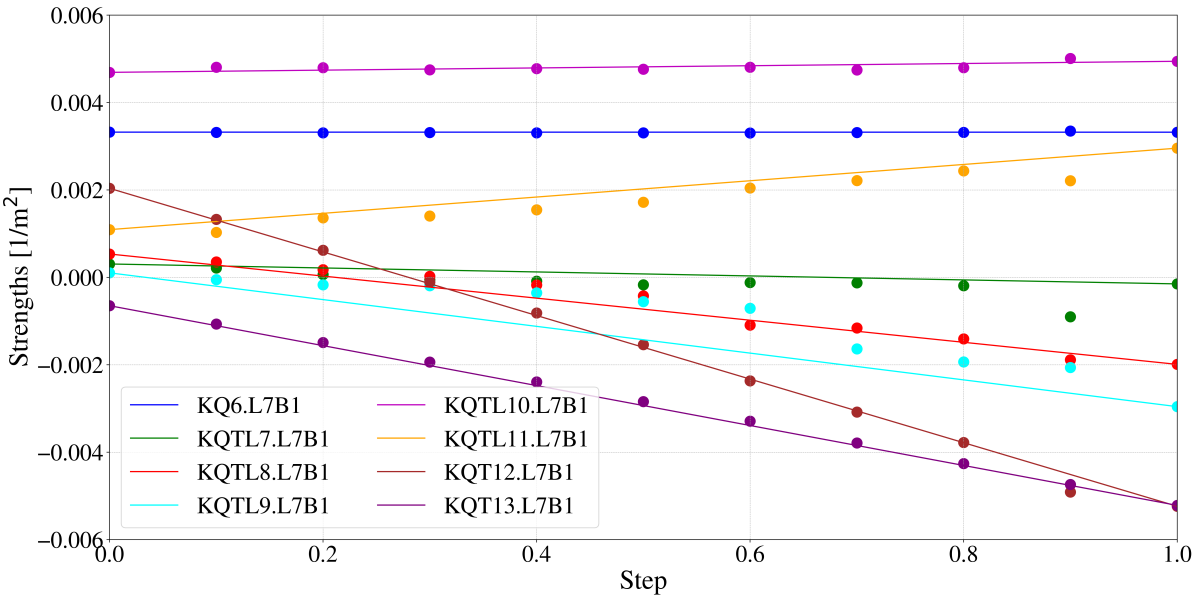


Figure 3.7: The lines represent the linear interpolation of the quadrupole strengths, while the points correspond to the matched optics solutions computed at each of the nine intermediate steps.

remain above the defined limit at all points of the transition, so the intermediate optics configuration can only be introduced once the available aperture is sufficient. Second, the collimator jaw movement should be monotonic over time, in order to avoid reversal of motion that can cause operational issues. Starting from the matched points obtained

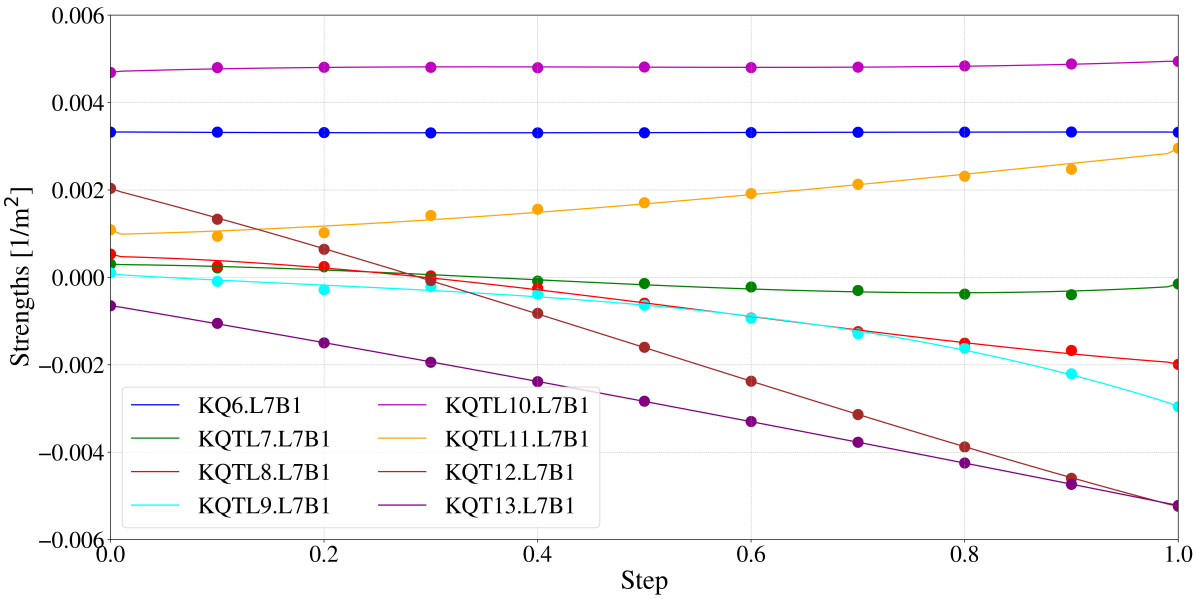


Figure 3.8: The lines represent the polynomial interpolation of the quadrupole strengths, while the points correspond to the matched optics solutions computed at each of the nine intermediate steps

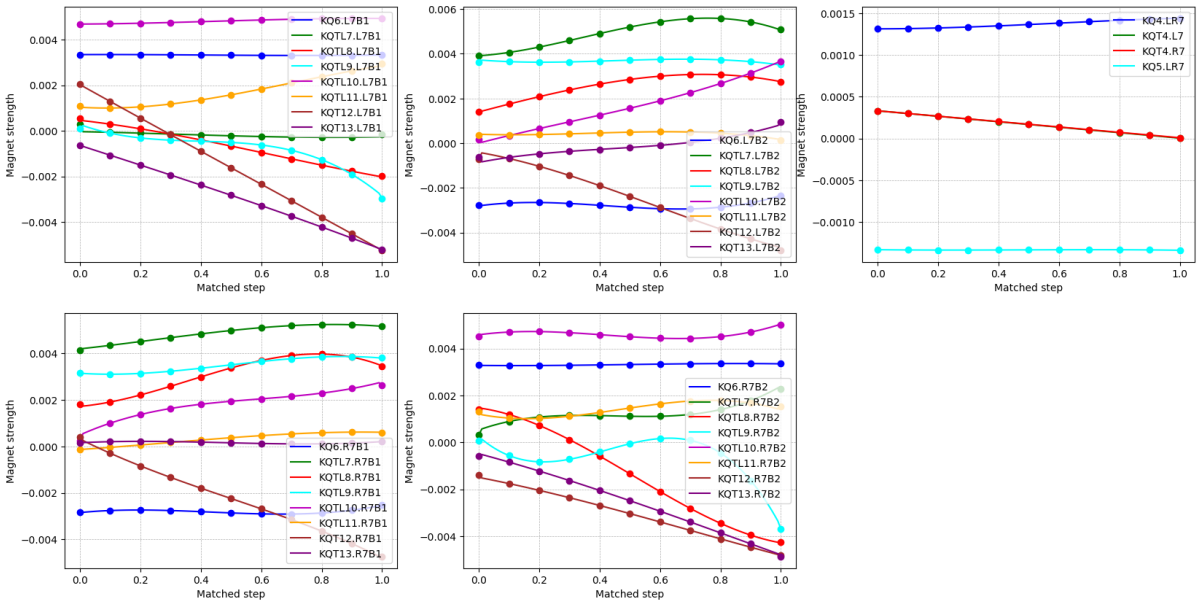


Figure 3.9: Example of the optics transition showing non-smooth interpolations of the quadrupole strengths.

with the procedure described above, a set of candidate times along the ramp was defined. The aperture and the collimator gaps were evaluated at these times, and the timing of the matched points was adjusted until both the aperture constraint and monotonicity of the collimator functions were fulfilled. Once the times of the matched points were defined,

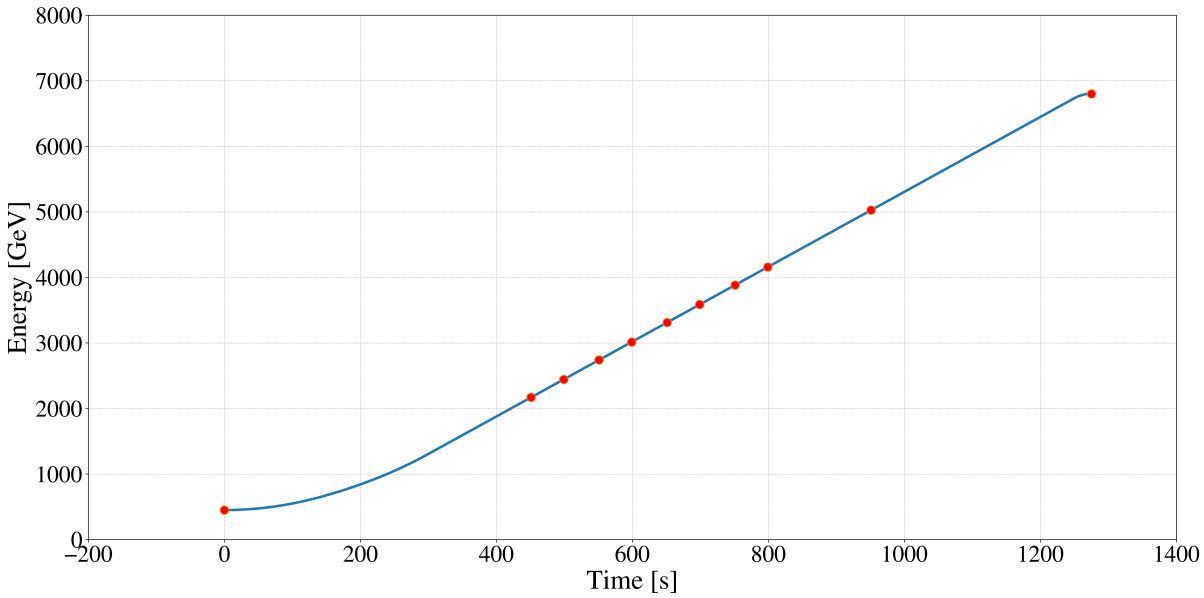


Figure 3.10: Beam energy as a function of time during the LHC energy ramp. The red markers indicate the times at which the matched optics configurations are implemented.

the polynomial interpolation of the quadrupole strengths was mapped to these times, resulting in a time-dependent function. A final matching was then performed, obtaining the final ramp functions of the quadrupoles. The first optic configuration is introduced at about 400s and the subsequent ones are inserted at later times, with the final optics implemented at the end of the ramp.
For each intermediate optics configuration, the jaw positions $p_{left,right}$ of each collimator in IR7 were computed according to the Eq. 3.2 and then plotted as a function of time during the energy ramp.

$$p_{left,right} = \pm n[\sigma]\sigma \tag{3.2}$$

where $n[\sigma]$ is the setting of the collimator in unit of beam size and $\sigma$ is the beam size corresponding to each optics configuration. The beam size is computed as:

$$\sigma = \sqrt{\frac{\epsilon_n m}{E}\left(\beta_x \cos^2\theta + \beta_y \sin^2\theta\right)}$$

where both the energy $E$ and the $\beta$ functions are those corresponding to each optics configurations, and $\theta$ is the angle of the collimator jaw with respect to the horizontal axis $x$. Despite the monotonicity requirement, some collimators have a non-monotonic movement during the energy ramp, with the jaw first moving inward and then outward, as shown in Fig. 3.12. A monotonic collimator movement, such as the one shown in Fig. 3.11 is

preferred during the energy ramp.
Indeed, a non-monotonic collimator movement can lead to some issues. The first issue is related to the mechanical backlash: each jaw is moved by two stepper motors and the mechanical backlash happens because of a small mechanical play between the moving parts. When the stepper motor inverts his direction of motion, the first part of the motion is "absorbed" by this mechanical play before a real displacement of the jaw occurs. This leads to a delay in the jaw response that can cause the jaw to not reach the desired final position.
An earlier insertion of the optics transition in the ramp was developed and resulted in monotonic collimator movements. Although this option was not implemented for operational reasons, future developments for the HL-LHC project will address this aspect.

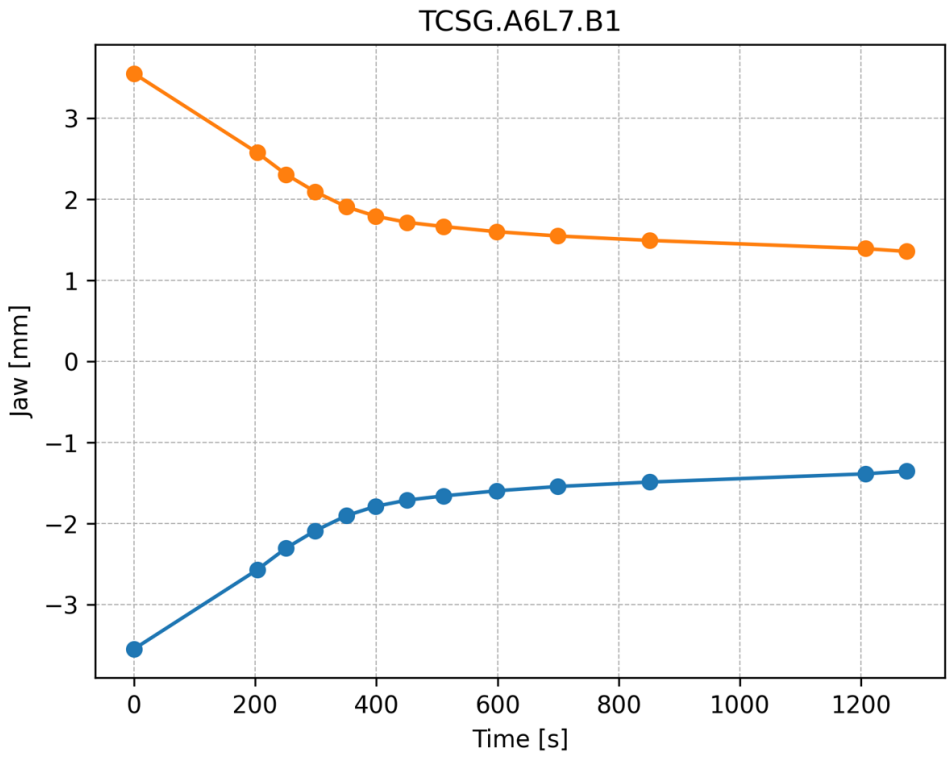


Figure 3.11: Example of monotonic collimator movement.

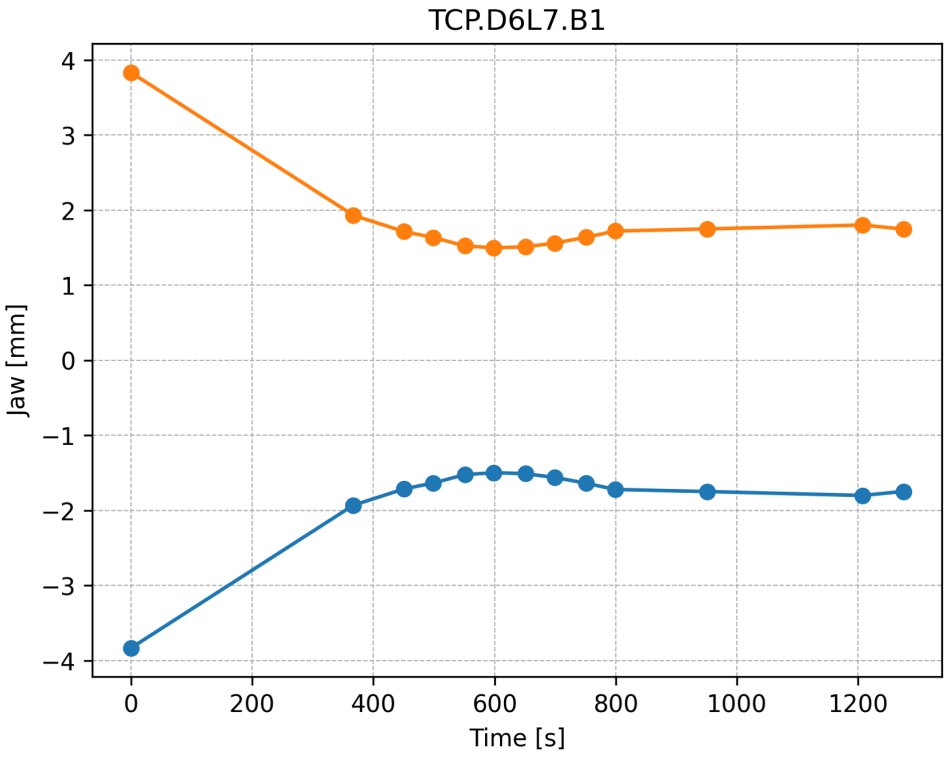


Figure 3.12: Non-monotonic collimator movement.

The final step, before the optics can be introduced in the machine, is to provide tune and chromaticity corrections throughout the transition. Figure 3.13 shows how the chromaticity varies over the ramp. This is produced by the changing quadrupole strengths in IR7, which is not compensated for in the linear optics matching described above. In the LHC, there are dedicated sextupoles for correcting chromaticity, and these were used together with the tune correctors to create a correction at each matched point.

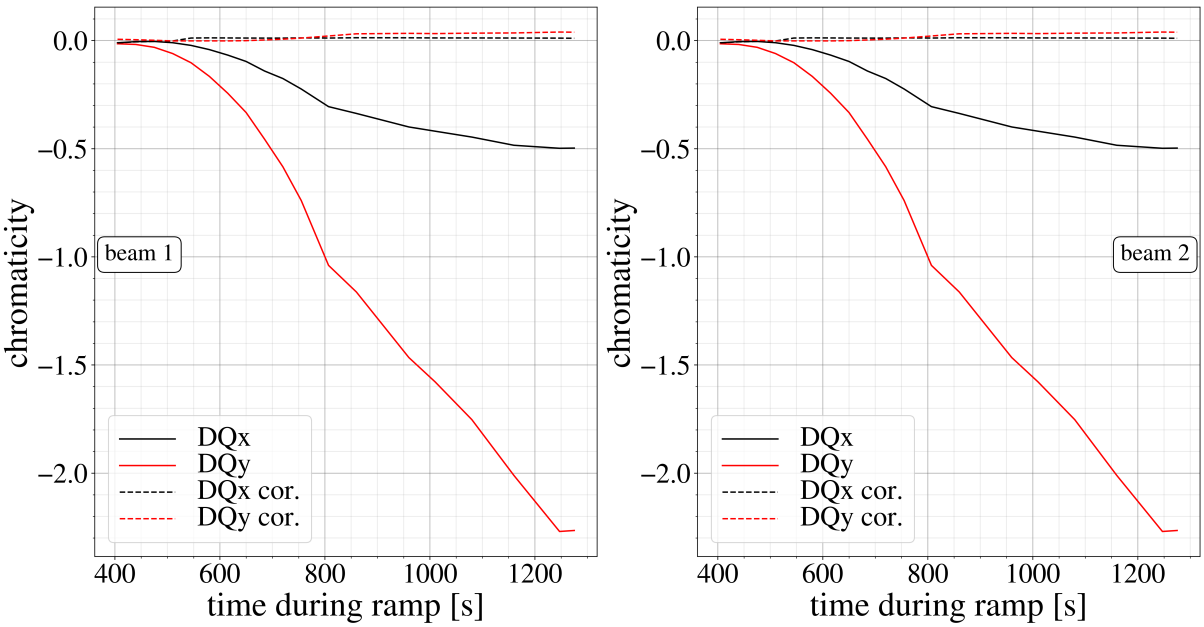


Figure 3.13: Chromaticity during the energy ramp.

## 3.3. Strengths and Currents evolution during the energy ramp

The LHC energy ramp brings the beams from 450 GeV to 6.8 TeV in approximately 1275 seconds. Fig. 3.14 and Fig. 3.15 show the quadrupole strengths and the quadrupole currents plotted as a function of time during the ramp. Their evolution is smooth and continuous, as desired. Both first and second derivatives of currents are within the operational limits of both warm and superconducting magnets used for the matching.

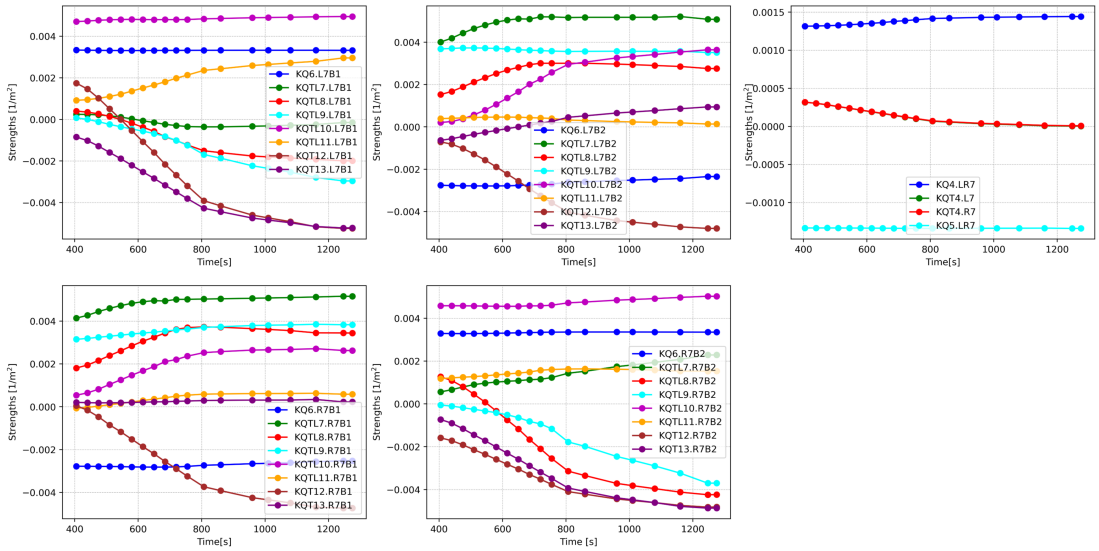


Figure 3.14: Strength evolution during energy ramp. The plot illustrates the behaviour starting from 400s, corresponding to the time at which the first optics configuration is inserted.

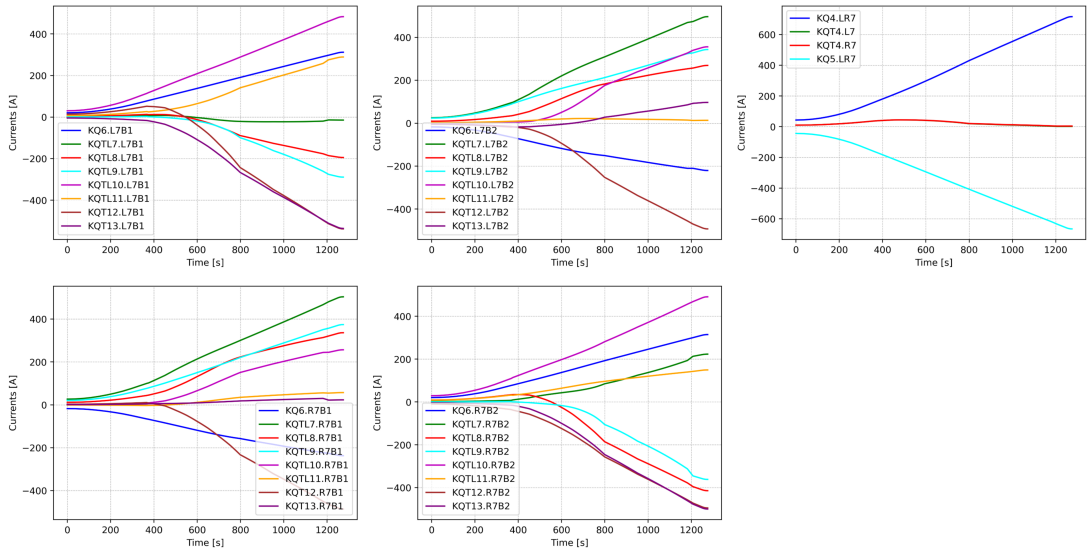


Figure 3.15: Currents evolution during energy ramp.

# 4 | Simulations of collimation performance

A detailed theoretical understanding of the collimation system and the ability to predict local beam losses are essential to ensure an efficient and safe operation of the LHC. This is even more important considering the higher beam intensity foreseen for the High-Luminosity upgrade. Therefore, simulations are required to investigate beam losses and evaluate the performance of the collimation system.

## 4.1. Simulation tools for collimation cleaning

The simulations performed in this chapter use XColl, the XSuite module dedicated to modelling particle-matter interactions in collimators and other devices. Collimators can be loaded from a database and installed in the accelerator lattice.
When a particle hits the jaw of a collimator, the interaction with the collimator jaw material is modeled by the physics engine Everest. Everest simulates the main interactions, including Multiple Coulomb Scattering, Nuclear Scattering and Ionization energy loss. For more detailed and realistic scenarios, Xcoll can be coupled to FLUKA or Geant4, to simulate the generation of secondary particles and radiation effects. For the purpose of the thesis, which focuses on beam losses far from the collimators and collimation studies, the Everest engine is sufficient.
To study the cleaning performance of the collimation system, an initial particle distribution is generated at the primary collimator, representing the beam impinging on the jaw. In the simulations performed in this thesis, an initial pencil beam distribution was used. This means that all the particles have same position and same angle, corresponding to a point in the phase-space. The pencil beam can be generated either in the horizontal or vertical plane. Horizontal and vertical halo are simulated separately, with a pencil beam defined in the corresponding plane, while the particle distribution in the other planes have a Gaussian profile. In both cases, all particles are generated so that they interact with

the IR7 primary collimators at the first turn.
Once the initial distribution of particles has been defined, particles are tracked along the accelerator lattice through Xtrack. Whenever a particle hits the collimator, it can be absorbed or scattered. If it is not absorbed it continues to be tracked. If the particle is absorbed, the position and the element where the absorption happens are recorded. The collection of these absorption events forms the loss map, a plot that provides the longitudinal distribution of the beam losses along the accelerator. Loss maps are tools to identify where the losses occur and to quantify them at each location. Horizontal loss maps are obtained from simulations with a horizontal pencil beam, while vertical loss maps result from simulations with a vertical pencil beam. This allows the cleaning performance to be assessed separately in the two transverse planes.
An example of the simulation setup is shown in the following script, which illustrates how the particle distribution is generated, tracked and how losses are recorded using Xtrack and XColl.

```
import xtrack as xt
import xcoll as xc

NUM_PARTICLES=10000

# Load the line
lhc = xt.Line.from_json('/.../line.json')

# Load and install collimators from collimator database
colldb = xc.CollimatorDatabase.from_yaml('/.../database.yaml', beam=1)
colldb.install_everest_collimators(line=lhc, verbose=True)

#Build the tracker and assign the optics to collimators
lhc.build_tracker()
lhc.collimators.assign_optics()

#Generate an initial particle distribution: pencil distribution on a horizontal TCP
print('Generating particles...')
particles = lhc['tcp.c6l7.b1'].generate_pencil(NUM_PARTICLES)

# Enable scattering and track for N turns
lhc.scattering.enable()
num_turns=200
lhc.track(particles, num_turns=num_turns, with_progress=1)
lhc.scattering.disable()

#Create and save the lossmap for the analysis
LM = xc.LossMap(lhc, line_is_reversed=False, part=particles)
LM.to_json(file=Path(f'lossmap_B1H.json'))
```

Figure 4.1: Example of a simulation setup.

As mentioned above, the output of this script is a loss map. Based on the simulation setup shown in Fig. 4.1, simulations were performed both for the new optics and reference optics in IR7, during the energy ramp and at top-energy.

The resulting loss maps, shown in the following section, are analyzed to assess the collimation cleaning performance with the new IR7 optics.

## 4.2. Simulated IR7 cleaning performance

The loss map show the local cleaning inefficiency $\eta_c$, defined in Eq. 2.33, along the length of the machine. The simulated loss maps at top energy (6.8 TeV) for the new optics and the reference optics for Beam 1 and Beam 2, horizontal and vertical case are shown in Figs. 4.2–4.9. The red lines are the *warm losses* and identify the beam losses on normal conducting magnets that work at room temperature. The blue lines represent the *cold losses* and show the particles that are lost in superconducting magnets. The black lines represent beam losses on collimators. To prevent the quench of the superconducting magnets, the *cold losses* must not exceed the quench limit defined in Eq. 2.34.
The region downstream of IR7 (for Beam 1) is called Dispersion Suppressor (DS) and is a transition area between the straight section and the arc. Due to the main dipole magnets located here, the dispersion rises in this region, increasing from its nominally zero value in the betatron insertion to the typical arc value of about 2 m (see Fig. 5.8.
The DS is the most critical area in terms of beam losses because any off-momentum particles generated at the collimators that are not intercepted, will be lost here if they do not fulfill the momentum acceptance of the LHC arcs, roughly 1% energy deviation. Leaked particles lost here can have momentum deviations up to tens of percent. Three clusters of particle losses can be identified in the DS, corresponding to the dispersion peaks and is where beam losses are concentrated.
For the analysis of the cleaning performance the loss maps are zoomed in the betatron insertion region.
The local cleaning inefficiency $\eta_c$ quantifies the fraction of losses occurring in the superconducting magnets downstream of IR7. Since lower values of $\eta_c$ indicate a better-performing cleaning system, the goal is to minimize this quantity. The maximum cleaning inefficiency $\eta_{max}$ is the highest value of the local cleaning inefficiency and is typically observed in the cold region downstream of the collimation insertion.
Looking at the loss maps, $\eta_{max}$ and the cleaning inefficiency $\eta_c$ in the cold region are lower for the new optics scenario compared to the the reference optics scenario for both beams (Beam 1 and Beam 2) and both planes, meaning that the cleaning performance is improved with the new IR7 optics at top energy.

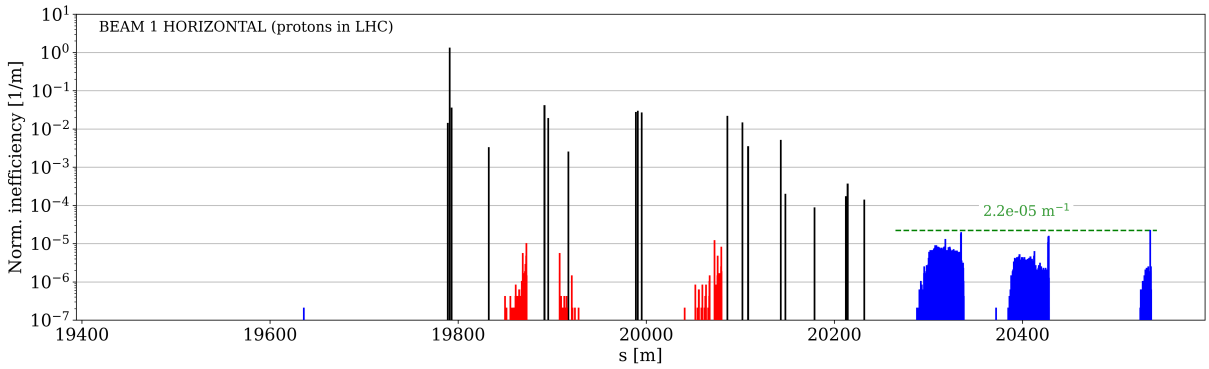


Figure 4.2: Simulated B1H lossmap at top energy in IR7 with new optics.

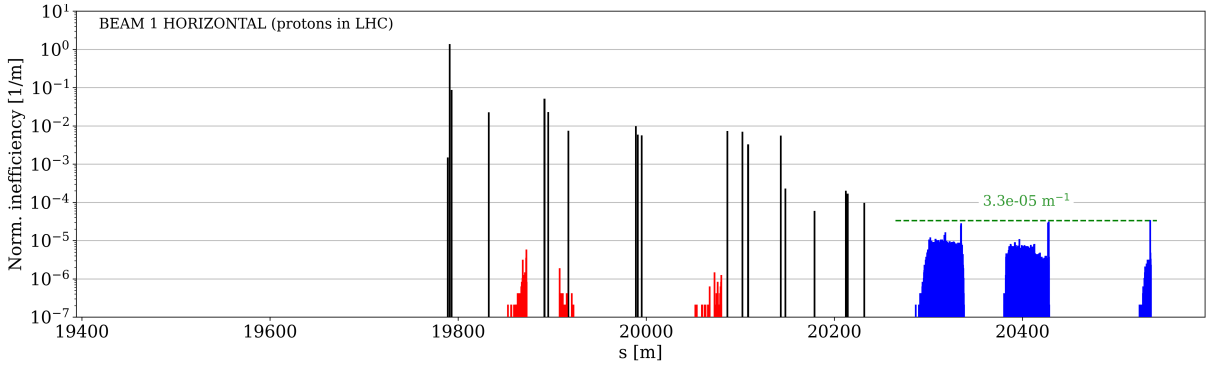


Figure 4.3: Simulated B1H lossmap at top energy in IR7 with reference optics.

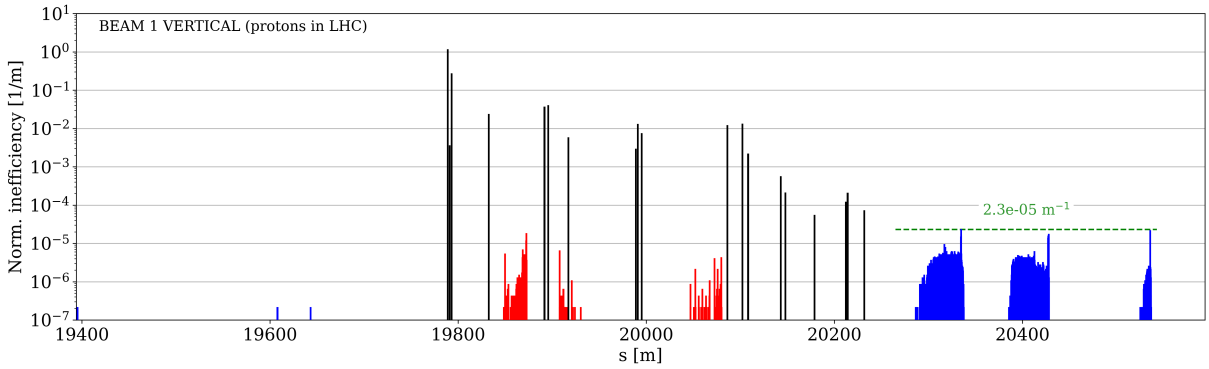


Figure 4.4: Simulated B1V lossmap at top energy in IR7 with new optics.

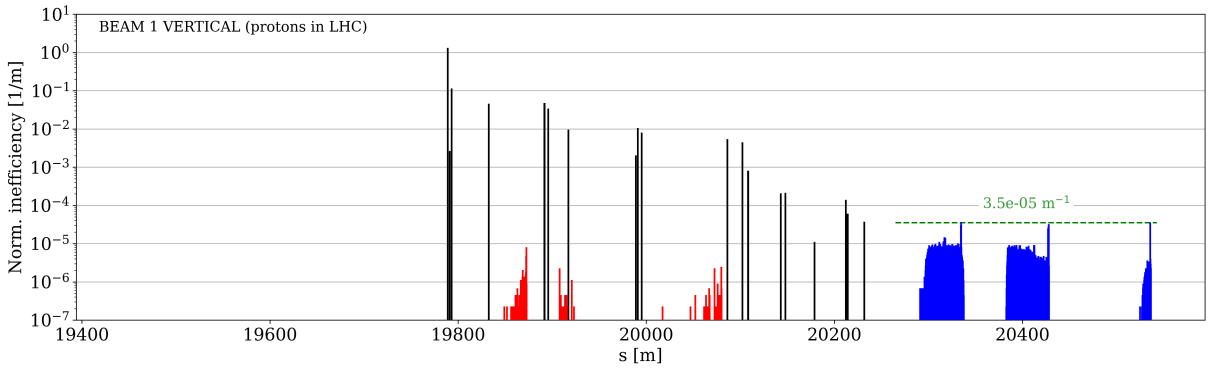


Figure 4.5: Simulated B1V lossmap at top energy in IR7 with reference optics.

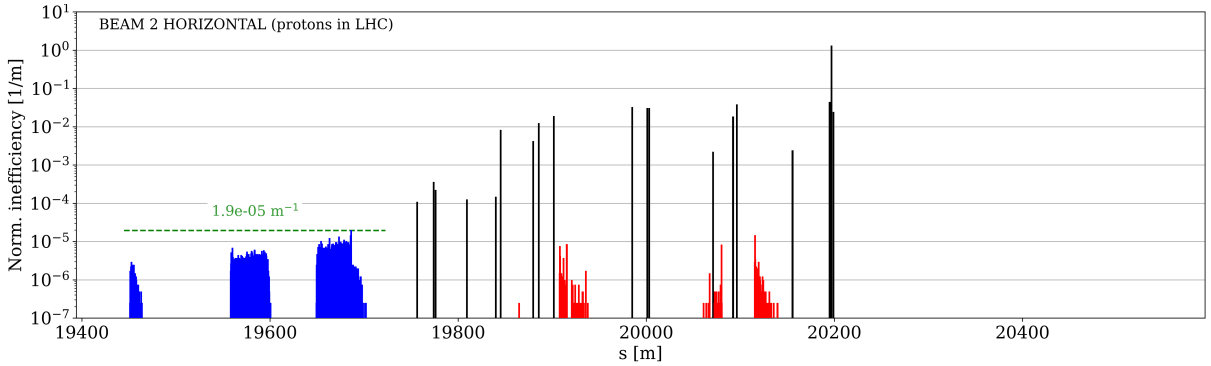


Figure 4.6: Simulated B2H lossmap at top energy in IR7 with new optics.

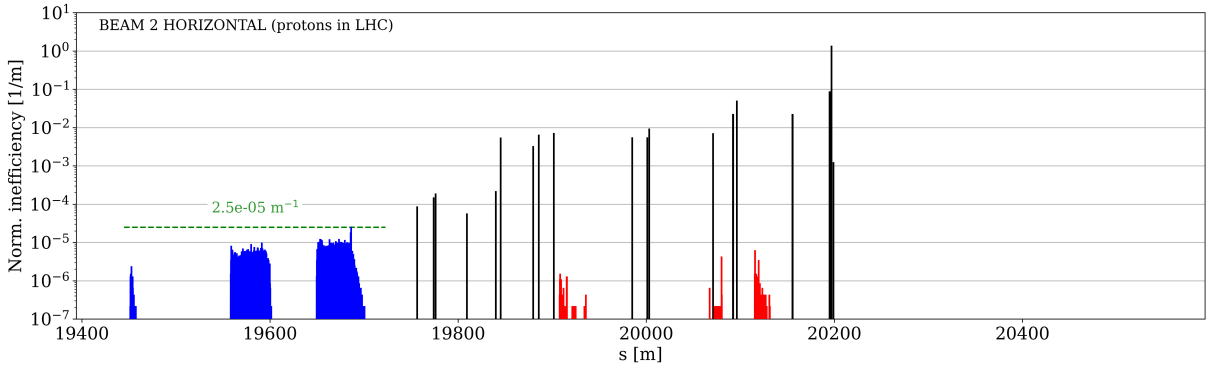


Figure 4.7: Simulated B2H lossmap at top energy in IR7 with reference optics.

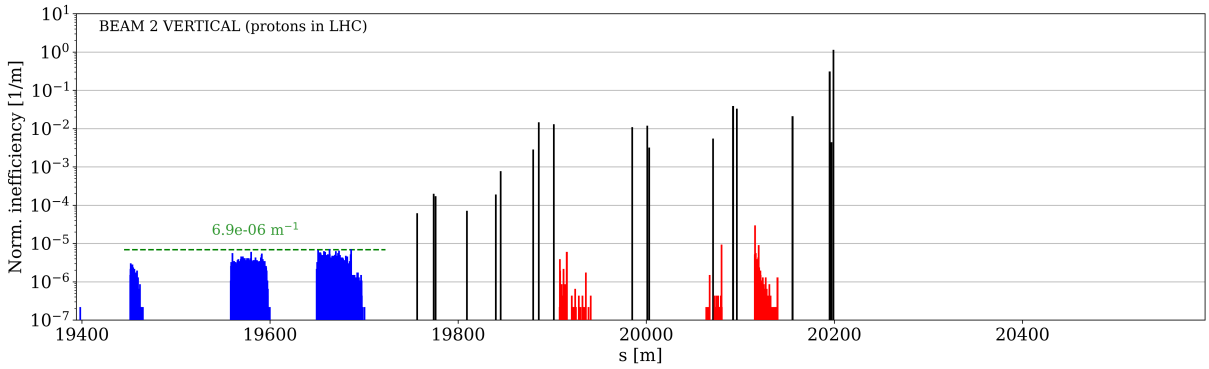


Figure 4.8: Simulated B2V lossmap at top energy in IR7 with new optics.

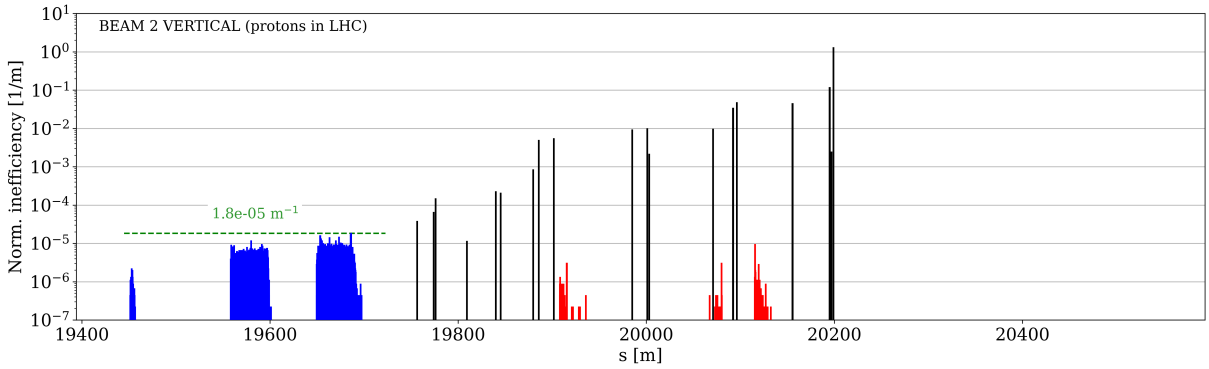


Figure 4.9: Simulated B2V lossmap at top energy in IR7 with reference optics.

To quantify the improvement of the cleaning performance with the new IR7 optics, the relative reduction of the maximum cleaning inefficiency $R$ was calculated for each case:

$$R = \frac{\eta_{ref} - \eta_{new}}{\eta_{ref}} \times 100 \tag{4.1}$$

where $\eta_{ref}$ and $\eta_{new}$ are the maximum cleaning inefficiencies for the reference and the new optics. A higher value of $R$ implies a higher reduction of the cleaning inefficiency, therefore a higher improvement in the cleaning performance. For Beam 1, the relative reduction $R$ is 33% for the horizontal plane and 34% for the vertical plane. For Beam 2, $R$ is 24% for the horizontal plane and 62% for the vertical plane.
These results show that the new IR7 optics provides a significant improvement in the cleaning performance at top-energy.
The cleaning performance must also be assessed during the energy ramp, to ensure that there is no degradation during the optics transition. This was simulated and the average

losses in each cluster $f_{cluster}$ of the dispersion suppressor were calculated as:

$$f_{\text{cluster}} = \frac{\sum_{i \in \text{cluster}} N_{\text{lost,i}}}{N_{\text{coll}} \Delta s_{\text{cluster}}} \tag{4.2}$$

where $N_{\text{lost,i}}$ is the number of particles lost at position $i$ in the cluster, $N_{\text{coll}}$ is the number of particles absorbed by the collimation system and $\Delta s_{\text{cluster}}$ is the longitudinal length of the cluster, defined as the region with non-zero losses. This quantity represents the average losses per unit length in a given cluster, normalized to the total number of particles lost at collimators, thus providing the local losses relative to the total losses in the collimation system. Since the first cluster of the DS typically shows the highest beam losses and represents the first location where particles leaking out of the collimation system are lost, the analysis focuses on this region, corresponding to the range $20290 \leq s \leq 20350$ m for Beam 1 and $19640 \leq s \leq 19700$ m for Beam 2, as shown in Figs. 4.2-4.9.

The evolution of the average losses during the energy ramp, while the optics transitions from the nominal to the new one, can be observed from the solid lines in Fig. 4.10. The same calculations have been performed with the reference optics, and the comparison is shown in Fig. 4.10.

The solid lines represent the new optics case, while dashed lines corresponds to the reference optics. The lines are shown starting from 400s, which is the time of the first matched point with a change to the IR7 optics. All beams and all planes, except for Beam 2 Horizontal, show a similar trend: the average losses in the first cluster increase at the beginning of the ramp and then, at about 700s, start decreasing.

The initial increase is explained by the increase of the beam energy during the ramp, leading to higher losses in the DS.

The subsequent reduction is due to the progressive deployment of the new optics, which improves the collimator efficiency and therefore reduces the leakage in the cold region. The behaviour results from a combined effect of the increasing beam energy and gradual improvement of the collimation performance.

Except for the beginning of the energy ramp, where Beam 1 horizontal and vertical show slightly higher values with respect to the reference, the solid line remains below the dashed ones for the rest of the ramp.

This indicates that, throughout the ramp, the new optics is equivalent or better than the reference one, which is an excellent result.

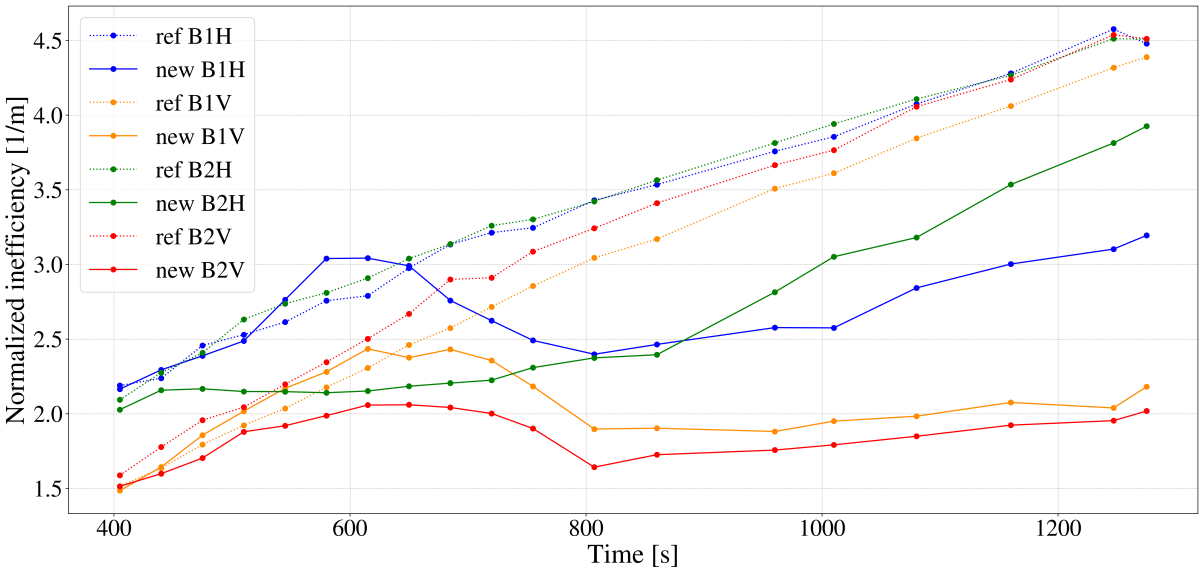


Figure 4.10: Cleaning inefficiency at the first IR7 DS cluster as a function of time in the energy ramp for both beams and planes. Old (dashed lines) and new (solid lines) optics were simulated for comparison.

However there is a redistribution of the losses between IR7 and IR3: with the new optics a larger fraction of on-momentum particles scattered out of the TCPs, which are not directly intercepted within IR7 or lost in the DS, can circulate along the ring and be lost in IR3. Therefore, a slight increase of the beam losses in IR3 with the new optics is not excluded.
A Loss Distribution Ratio for the new and reference IR7 optics was calculated for every simulated energy as:

$$Ratio_{\mathrm{IR3/IR7}} = \frac{\text{Total losses at IR3 collimators}}{\text{Total losses at IR7 collimators}}. \tag{4.3}$$

This ratio quantifies how the losses are shared between the two cleaning insertions.[1] As shown in Fig. 4.11, for the scenario of primary losses in IR7 (betatron losses), for the new optics the ratio shows an increasing trend along the energy ramp for all the beams and all the planes. The same evolution is also found for the reference optics.

[1]Off-momentum losses are still lost at IR3.

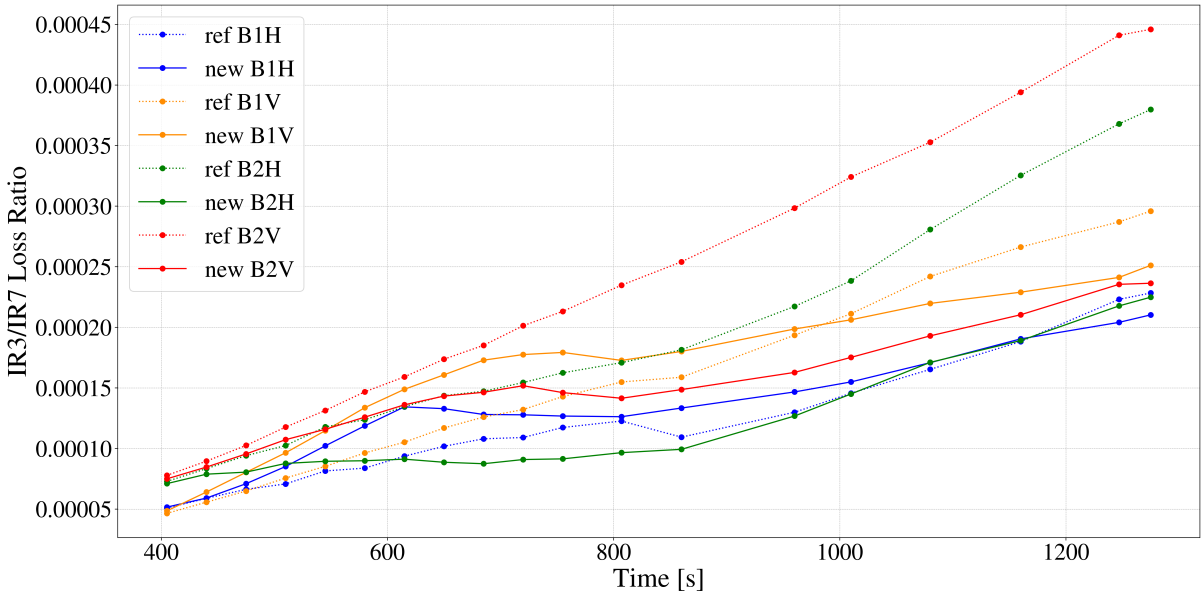


Figure 4.11: IR3/IR7 loss ratio as function of time in the energy ramp for both beams and planes. Old (dashed lines) and new (solid lines) optics were simulated for comparison.

In addition to the cleaning performance, it is important to assess the beam losses at the tertiary collimators (TCTs) upstream of the collision points. Particles lost on the TCTs can produce secondary showers that reach the experimental detectors, contributing to the experimental background. Some increase can be tolerated by the experiments, but losses at the TCTs should be carefully controlled.
The losses at the tertiary collimators are computed as the ratio between the total losses at the TCTs in IP1, IP2, IP5, IP8 and the total losses at collimators:

$$f_{\mathrm{TCT}(IP_i)} = \frac{N_{\mathrm{TCTs}(IP_i)}}{N_{\mathrm{coll}}}, \quad i \in \{1, 5, 8\} \tag{4.4}$$

where $N_{\mathrm{TCTs}(IP_i)}$ are the losses on TCTs at each collision point $i$ and $N_{\mathrm{coll}}$ are the total losses on collimators around the ring. Note that IP2 TCT losses are omitted from the following analysis, since the IP2 TCTs are retracted during proton operations and see negligible losses.
In Fig 4.12 $f_{\mathrm{TCT}(IP_i)}$ of Eq. 4.4 is shown at flat-top for IP1, IP5, IP8 compared to the reference optics. It can be observed that the TCTs losses increase compared to the reference case in all cases. In particular, the largest increase is observed for Beam 2 in the vertical plane, where the losses on TCTs increase by two orders of magnitude at IP1 (from about $6 \times 10^{-5}$ to $7 \times 10^{-3}$) and IP5 (from about $10^{-5}$ to $10^{-3}$). Beam 1 in the vertical plane also shows a significant increase, in particular in IP1 ( from $2 \times 10^{-4}$ to

$3 \times 10^{-3}$) and IP5 (from $3 \times 10^{-5}$ to $2 \times 10^{-3}$).
The increase of losses at the TCTs can be mitigated by optimizing the phase advance from the primary collimators to the tertiary collimators. This is foreseen for the final HL-LHC optics, but were not included in these tests in the LHC. In addition, HL-LHC will house an additional set of TCTs around IPs 1 and 5 that can help optimize the losses and the resulting background. It is important to note that these values must be validated by the experiments before drawing any conclusions on potential issues, and dedicated beam tests are planned before the end of Run III.

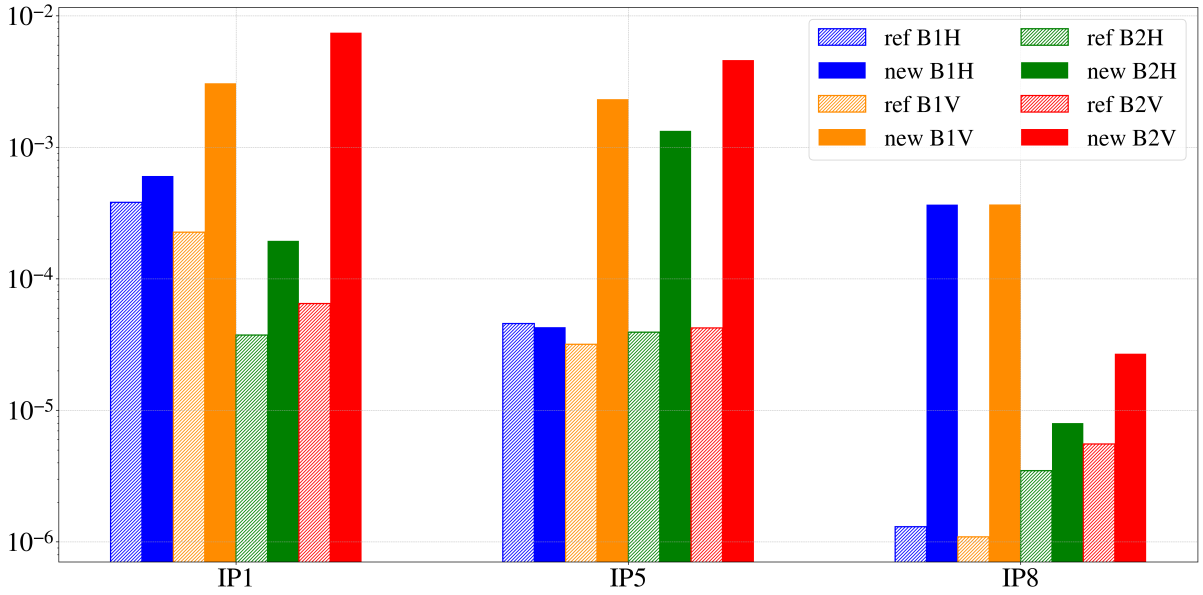


Figure 4.12: Comparison of tertiary collimator losses at top energy between the new and reference optics with tight TCT settings (logarithmic scale).

## 4.3. Performance for different setting scenarios

The same simulations have been performed for both the new optics and the reference optics using tighter settings for tertiary collimators. It was not possible, within the timeline of this thesis work, to study the TCT losses at the smallest $\beta^*$ values used for physics operation, where the TCTs are set tighter. For this reason, an intermediate scenario was conceived, featuring tight TCT settings together with larger $\beta^*$ values, and was used for simulation benchmark purposes. The collimator settings used for this intermediate scenario are the ones corresponding to the collision settings reported in Tab. 2.2.

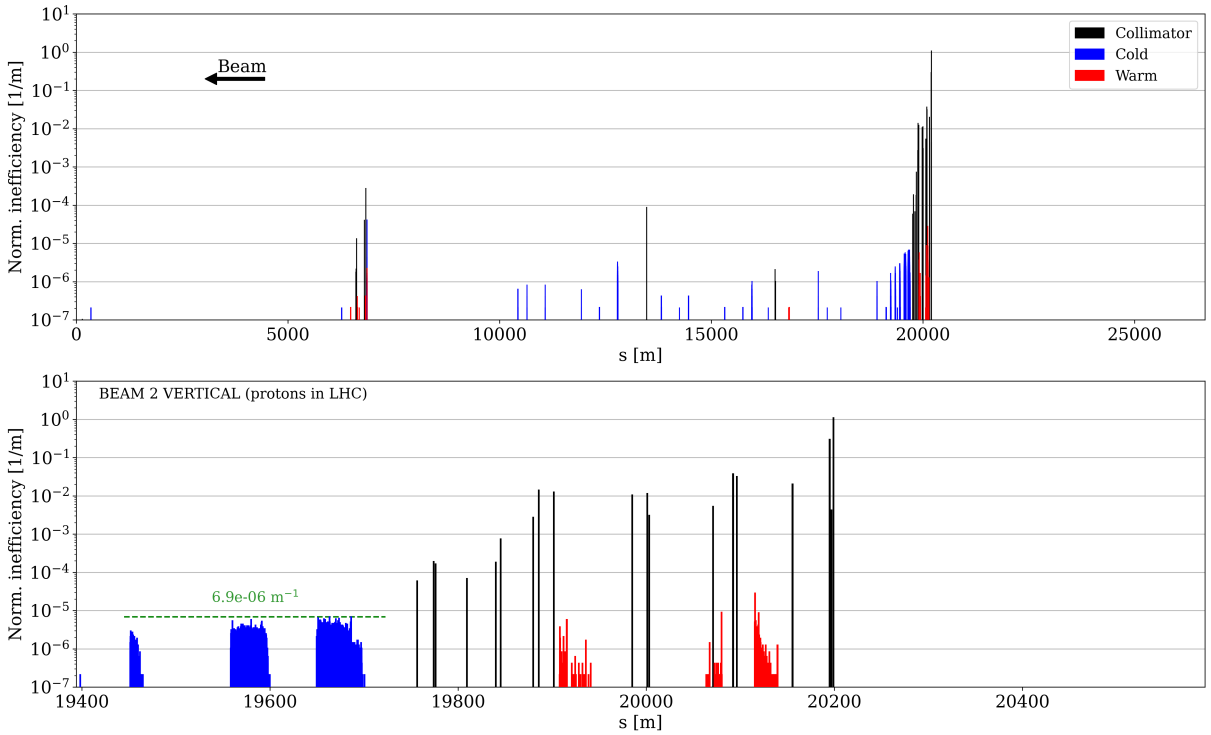


Figure 4.13: Simulated B1H lossmap at top energy in IR7 with new opticss.

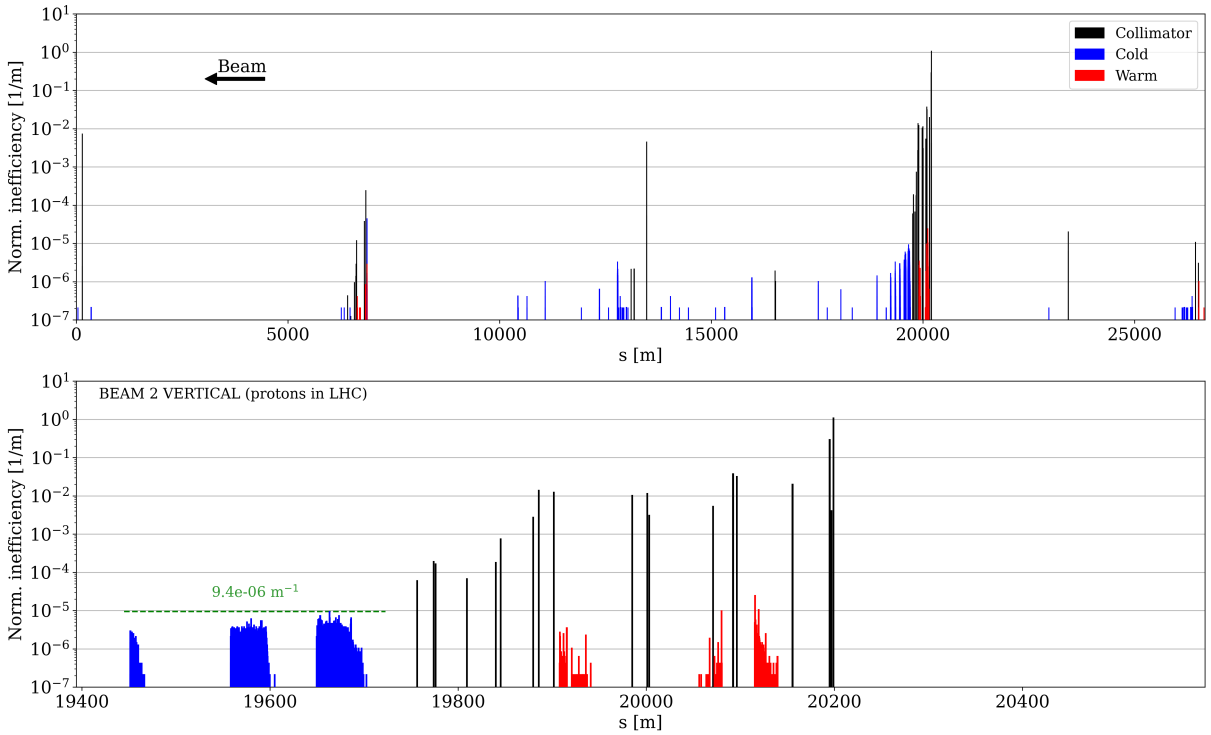


Figure 4.14: Simulated B1H lossmap at top energy in IR7 with new optics with tight TCTs settings.

As shown in Fig. 4.15, the average losses in the first DS cluster remain essentially unchanged comparing the nominal and tight TCT settings. This confirms that the tight TCT settings have no impact on the losses in this region.

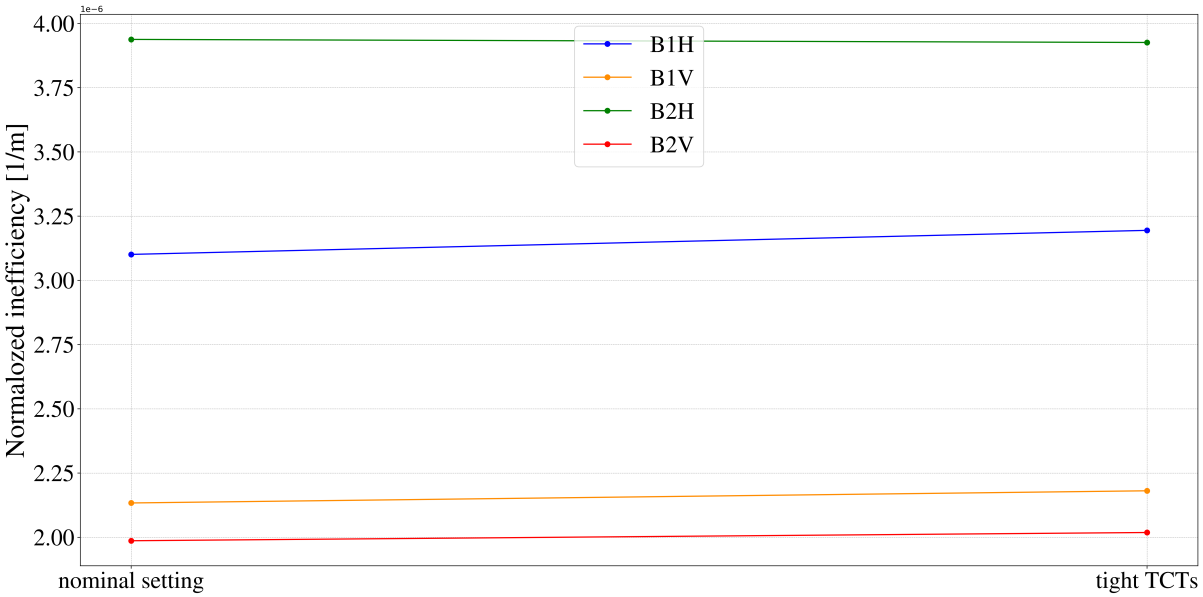


Figure 4.15: Comparison between the average losses in the first DS cluster with new optics for nominal settings and tight TCTs settings.

# 5 | Validation with LHC beam measurements

## 5.1. Short intro of MD time allocated in 2025

During 2025, Machine Development (MD) sessions were performed to test and validate the combined ramp and desqueeze developed for the new IR7 optics compatible with the Run III optics configuration. These are necessary tests to assess a potential operational deployment in 2026, which is under evaluation at the time of writing. Important tests were carried out in 2025 with the main objective of demonstrating that the cycle based on the improved IR7 optics is compatible with high intensity operation. Achieving this goal requires completing successfully various phases:

- Validation loss maps with low intensity beams: low intensity beams, with a total intensity below $3 \times 10^{11}$ protons per beam, were used to validate the cleaning performance during the energy ramp.
  Betatron and off-momentum loss maps were measured at intermediate energy steps (from 1000 to 6000 GeV) and at flat-top. An important milestone of this MD was the successful first operation of the new ramp functions without issues.
  These tests allowed the identification of loss spikes and assessment of the cleaning efficiency and the beam lifetime measured by the Beam Loss Monitors (BLMs) during the ramp. These low intensity tests are part of the machine protection requirements in the LHC before higher beam intensities are allowed to be used for a particular configuration or optics [29].

- Validation of combined ramp and desqueeze with high intensity beams. The combined ramp and desqueeze was tested with increasing beam intensity:
  - 12 nominal bunches per beam
  - 75 nominal bunches per beam
  - 444 nominal bunches per beam

In this session, the focus was on evaluating the cleaning performance and the impedance, which are the goals of the new IR7 optics, and on assessing the experimental background. Since the collimators in IR7 represent the effective physical aperture bottleneck of the machine, modifying the optics in this region, and doing it while the beam energy is ramped, a phase during which many machine parameters change, arises the concern that small errors in the optics or in the collimator movement could lead to sudden large loss spikes. For this reason, the analysis also aimed to assess the operational feasibility of the combined ramp and desqueeze with high intensity beams, focusing on any unforeseen loss spike or degradation of the cleaning performance during the energy ramp.

## 5.2. Measured optics performance

In the following section, the tools used to obtain loss maps are described.
For the betatron loss map measurements, the beam is excited transversely to generate controlled losses, so that halo particles can hit the primary collimators. The excitation is applied using the ADT, a system of electric kickers normally used to damp transverse oscillations of the bunches. For loss maps, a white noise excitation is instead applied through the kickers on selected bunches, leading to a larger emittance. This is referred to as *blowing up* the bunches. A horizontal excitation drives particles onto the horizontal TCP, yielding a horizontal loss map; the same applies to the vertical plane.
The beam losses are detected by the Beam Loss Monitors (BLMs), a system of about 4000 ionization chambers installed downstream of the most probable loss locations around the ring, such as quadrupoles, collimators and other sensitive components, and continuously measure secondary shower particles produced when protons impact machine elements [8, 28]. The measured signals provide the intensity and the distribution of the losses as a function of the longitudinal position along the ring, forming the loss map.
For off-momentum loss maps measurements, the RF frequency of the machine is purposely shifted from its nominal value. This frequency change causes the beam to become off-momentum with respect to the nominal energy, leading to controlled beam losses that are detected by the BLMs. The RF sweep is done with both positive and negative signs, to measure both signs of the off-momentum losses. The measured signals provide an off-momentum loss map.
The two types of measurements described above are used to assess the performance of the collimation system with two different loss mechanisms: betatron loss maps are used to study beam losses from transverse halo particles, off-momentum loss maps are used to analyze losses from particles having an energy offset with respect to the nominal energy.
In the following, considering the objectives of the this thesis, only the measured betatron

loss maps are analyzed.

The measured loss maps at top-energy (6.8 TeV) for the new optics and the reference optics, zoomed in IR7, are shown for Beam 1 and Beam 2 in both horizontal and vertical plane. The y-axis represents the Normalized BLM signal, which is the measured BLM signal normalized to the total losses at the collimators, and the x-axis is the longitudinal position along the machine. The statistical error of the normalized BLM signal in the loss maps is estimated to be ±7% [21], while the systematic error has not been estimated.

The maximum cleaning inefficiency $\eta_{max}$ in the DS region is lower for the new optics scenario with respect to the reference optics scenario for Beam 1 (horizontal and vertical) and Beam 2 vertical. However, the measured loss maps for Beam 2 horizontal obtained with the new and reference optics show a comparable maximum cleaning inefficiency.

The measured relative reduction of the maximum cleaning inefficiency in the DS region is approximately 46%, 55% and 52% for B1H, B1V and B2V. Overall, these improvements are consistent with expectations from the simulations (see Section 4.2), with the exception of B2H, which is not understood.

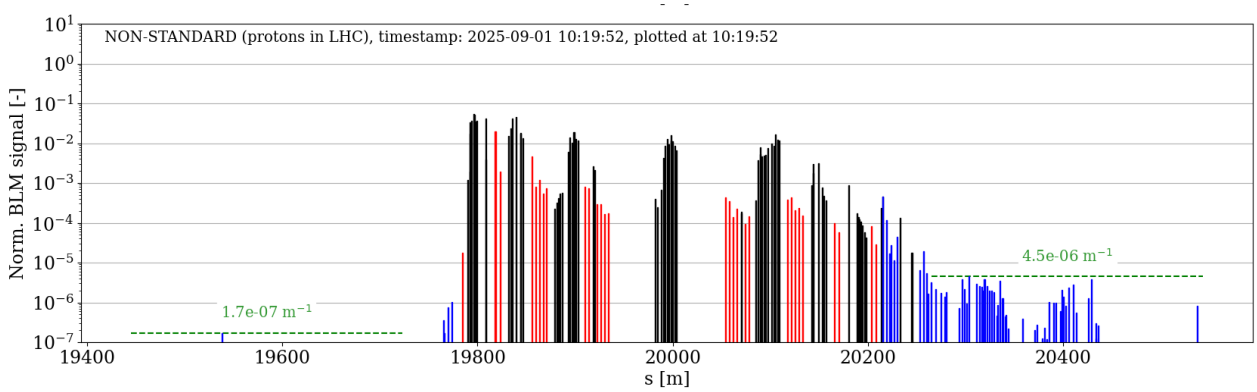


Figure 5.1: Measured B1H lossmap in IR7 with new optics.

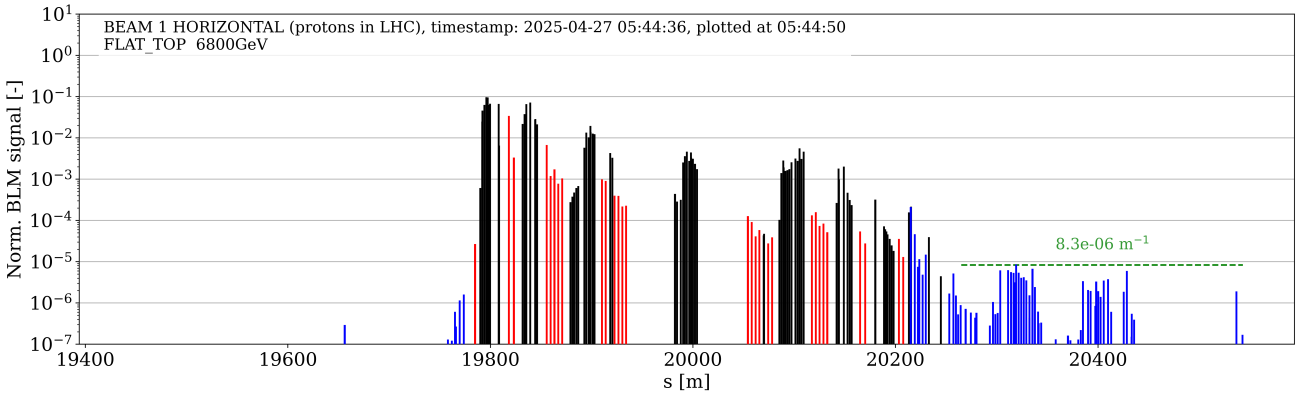


Figure 5.2: Measured B1H lossmap in IR7 with reference optics.

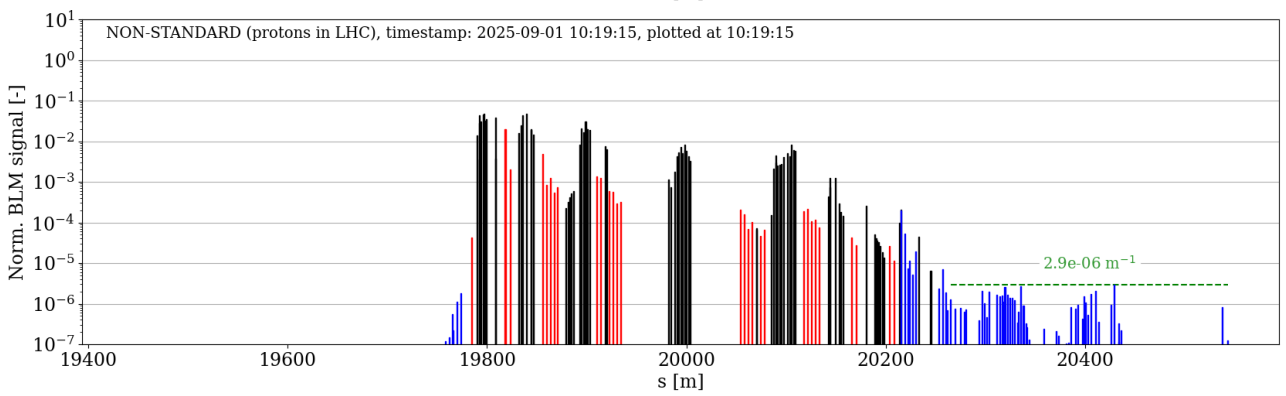


Figure 5.3: Measured B1V lossmap in IR7 with new optics.

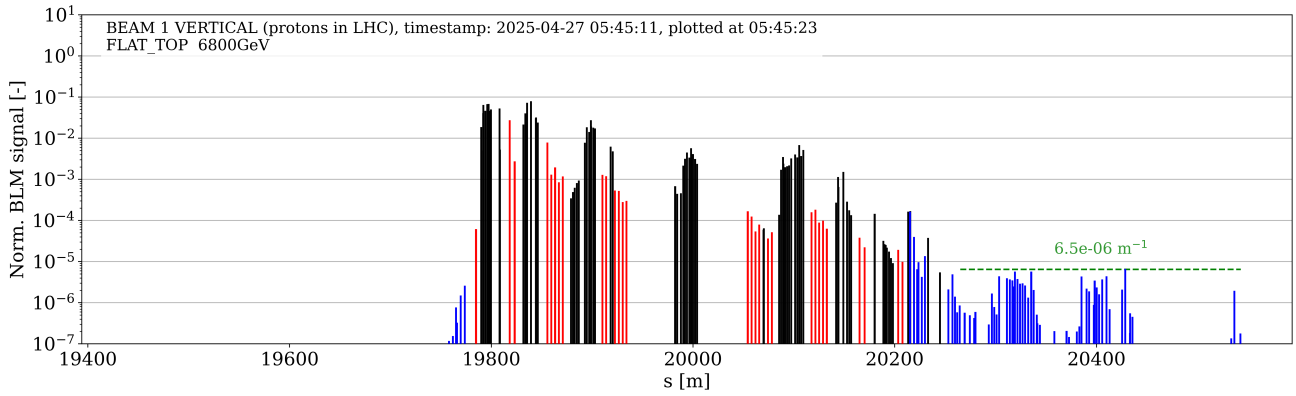


Figure 5.4: Measured B1V lossmap in IR7 with reference optics.

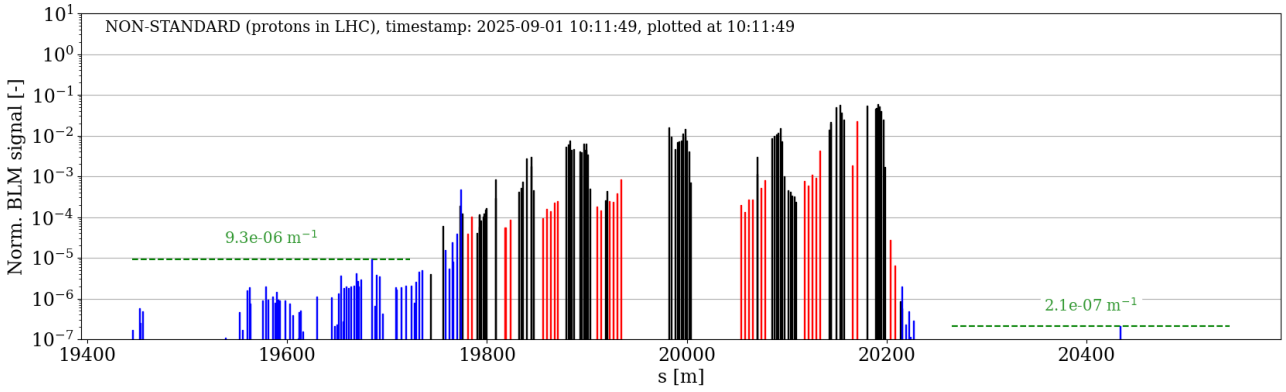


Figure 5.5: Measured B2H lossmap in IR7 with new optics.

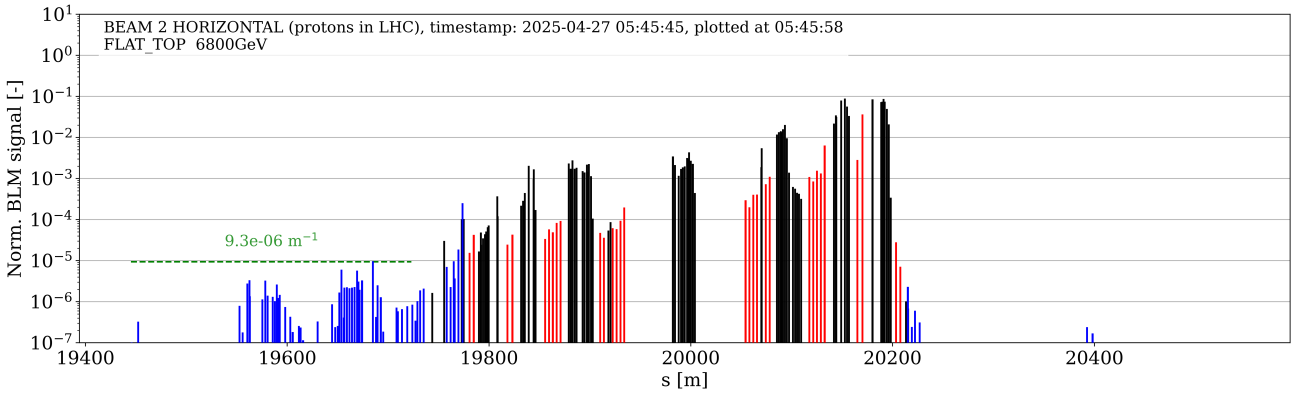


Figure 5.6: Measured B2H lossmap in IR7 with reference optics.

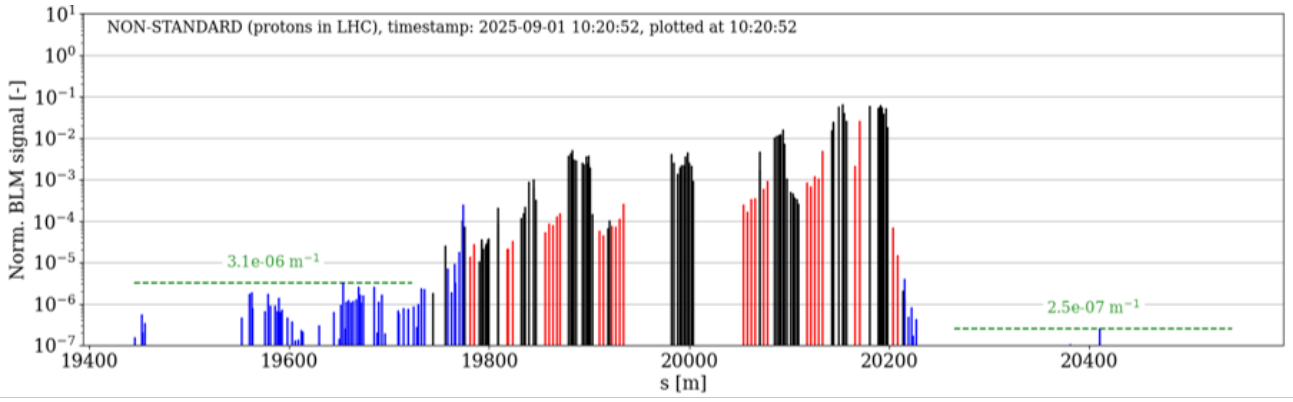


Figure 5.7: Measured B2V lossmap in IR7 with new optics.

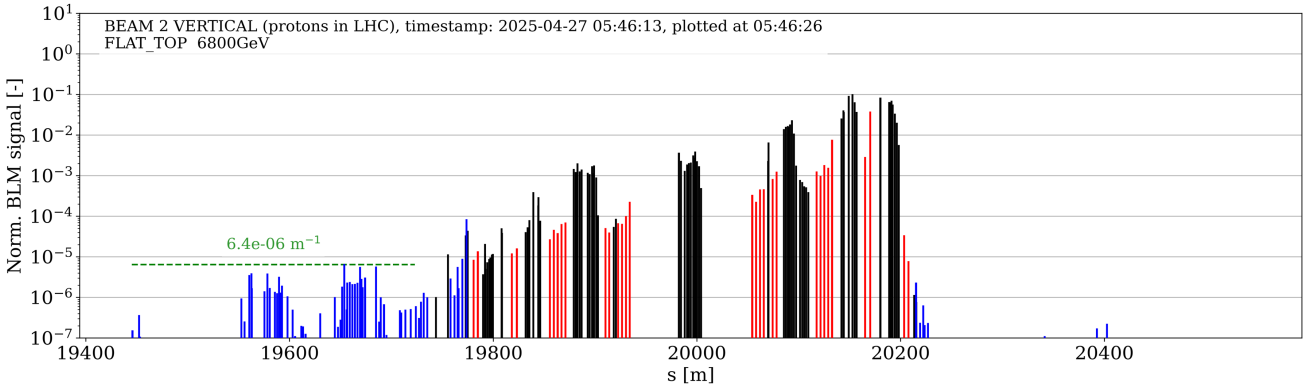


Figure 5.8: Measured B2V lossmap in IR7 with reference optics.

### 5.2.1. Optics validation during the LHC energy ramp

The $\beta$-beating quantifies the difference between the measured $\beta$ functions and those predicted by the optics model. It is used in the LHC to quantify optics errors and to evaluate

how the machine reproduces the design optics [27]. In practice, optics errors can generate large $\beta$-beating, while a well-matched optics typically shows small deviations, on the order of few percent [15].

During the implementation of the new optics at the LHC, the relative beta-beating $\Delta\beta/\beta_{\text{ref}}$ was measured for both beams and both planes at intermediate energies along the LHC ramp. Figure 5.9 shows the relative beta-beating inside the IR7 insertion. Figure 5.10 shows the relative beta-beating measured outside IR7, indicating how the rest of the machine behaves during the IR7 optics transition.

The measured beta beating was initially measured up to 25% for B1, prompting the calculation of a new global correction for B1. Following correction, the beta beating stayed below 20%, the maximum allowable tolerance generally specified for the LHC [26], showing that the combined ramp and desqueeze was succesfully implemented in the machine. Locally in IR7 the beta beating at top energy was below 6%, indicating that any discrepancies between measurements and simulations are unlikely due to optics errors.

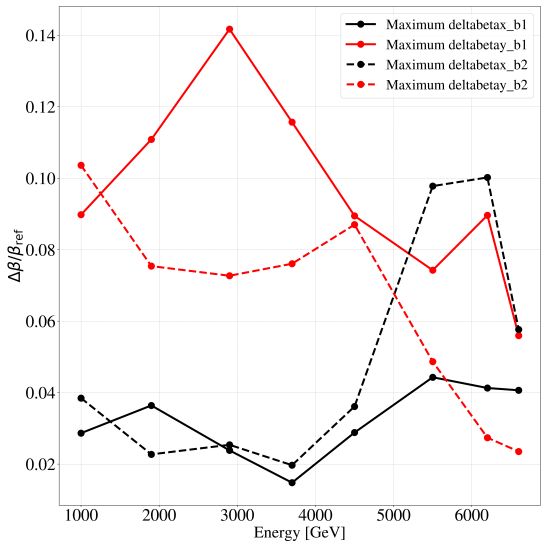


Figure 5.9: Maximum relative $\beta$-beating inside IR7 insertion for both beams and planes as function of energy during the ramp.

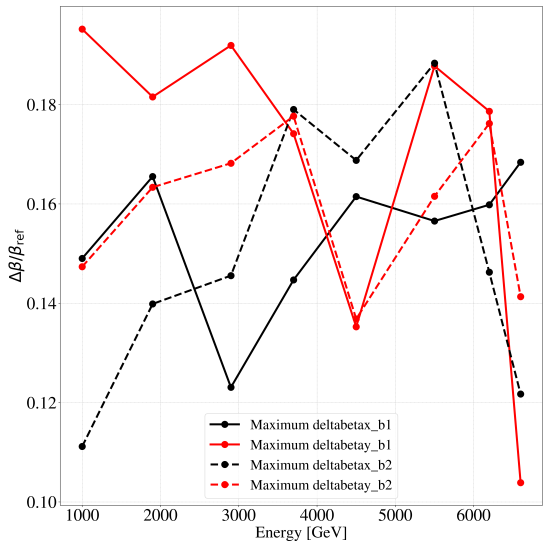


Figure 5.10: Maximum relative $\beta$-beating outside IR7 insertion for both beams and planes as function of energy during the ramp.

## 5.3. Cleaning performance during ramp and at 6.8 TeV

To quantify the cleaning performance of the collimation system with the new IR7 optics during the energy ramp, the average losses in the DS clusters were computed using Eq. 4.2 at specific time steps along the ramp. These measurements were performed by exciting

the beam on the fly during the execution of the ramp functions.
The time evolution is shown in Fig. 5.11. The dashed lines represent the reference optics, while the solid lines correspond to the new IR7 optics.
Starting from around 400s, when the first intermediate optics configuration is inserted and the optics in IR7 start to change, Beam 1 in both planes and Beam 2 vertical show an improvement of the cleaning inefficiency compared to the reference optics throughout the energy ramp, up to top-energy.
Beam 2 horizontal initially improves as well, but worsens towards the top energy. Further analysis is required to understand this, since it is not observed in simulations.

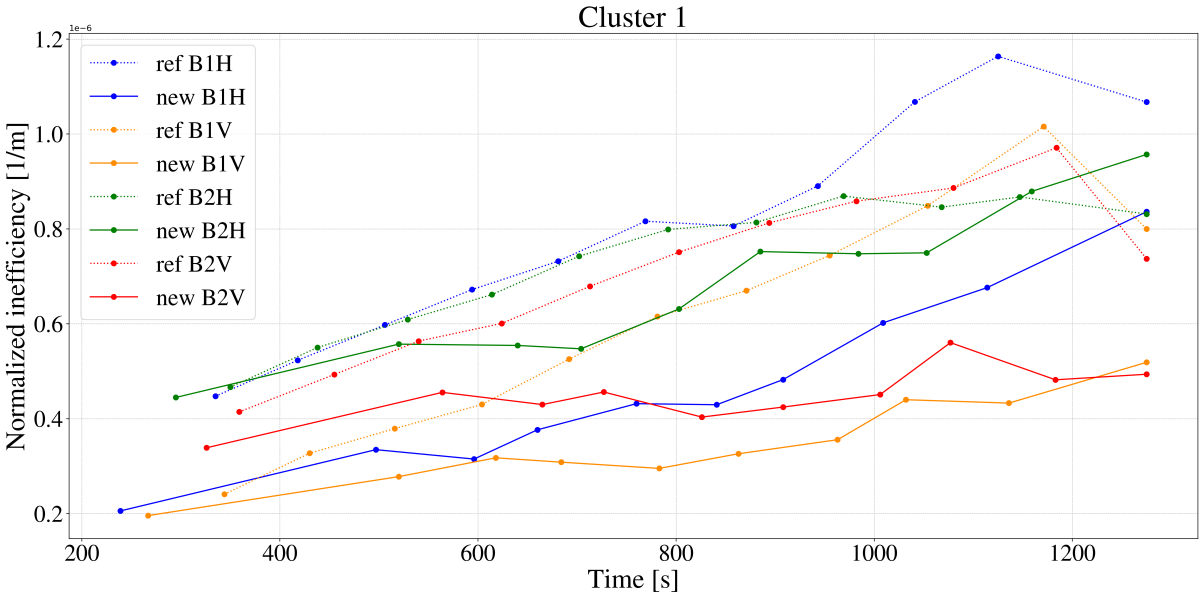


Figure 5.11: Comparison of measured cleaning performance in first DS cluster between the new optics and reference optics.

The distribution of losses between IR3 and IR7 during the energy ramp, computed with Eq 4.3, is shown in Fig. 5.12 for both the new and the reference optics. For all beams and all planes, the distribution loss ratio remains essentially constant throughout the energy ramp.

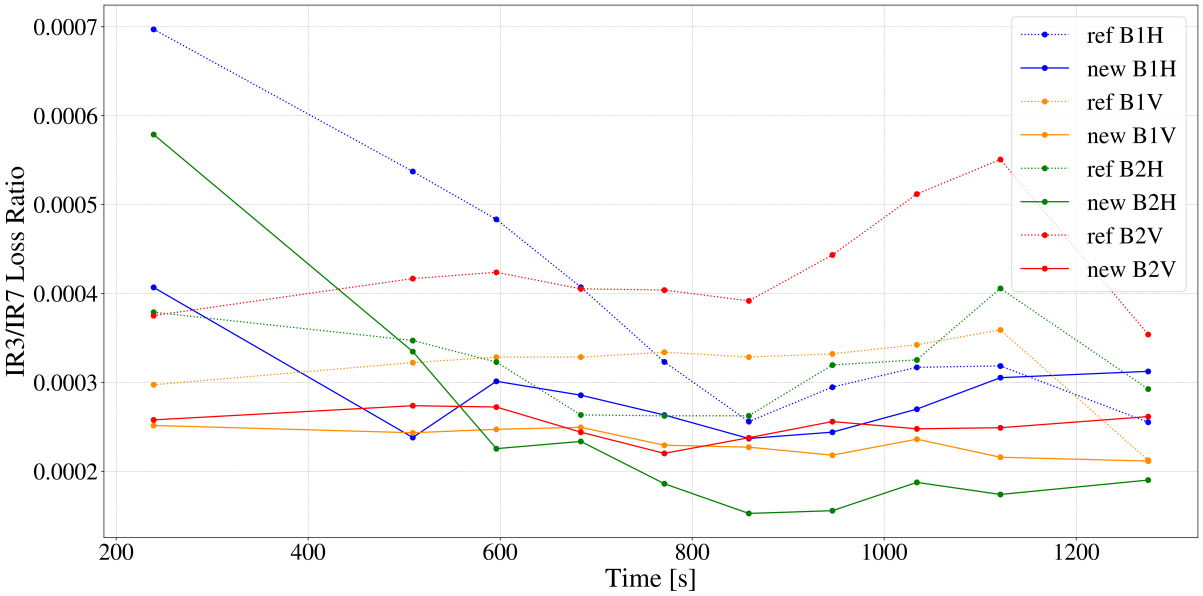


Figure 5.12: Comparison of the measured IR3/IR7 loss ratio between the new optics and the reference optics.

The analysis of the collimation performance continues with the evaluation of the losses at the tertiary collimators. The TCT losses have been evaluated using the definition given in Eq. 4.4. Figure 5.13 shows the ratio $f_{TCT}$ for both the new optics and the reference at IP1, IP5 and IP8 at top-energy. As predicted by simulation, an increase of the TCT losses is observed with the new optics configuration compared to the reference for all beams in each IP. In particular, the largest increase is observed at IP1, from about $5 \times 10^{-5}$ to $1.7 \times 10^{-3}$, and IP5, from about $2 \times 10^{-5}$ to $1.6 \times 10^{-3}$, for Beam 2 vertical. Beam 1 vertical shows a significant, yet smaller, increase at IP1, where the TCT losses increase from $1 \times 10^{-4}$ to $1.1 \times 10^{-3}$.
Smaller but still significant increases are observed in the horizontal plane, for Beam 1 at IP1 (from $2.5 \times 10^{-4}$ to $5.6 \times 10^{-4}$) and Beam 2 at IP5 (from $4 \times 10^{-5}$ to $6.3 \times 10^{-4}$).

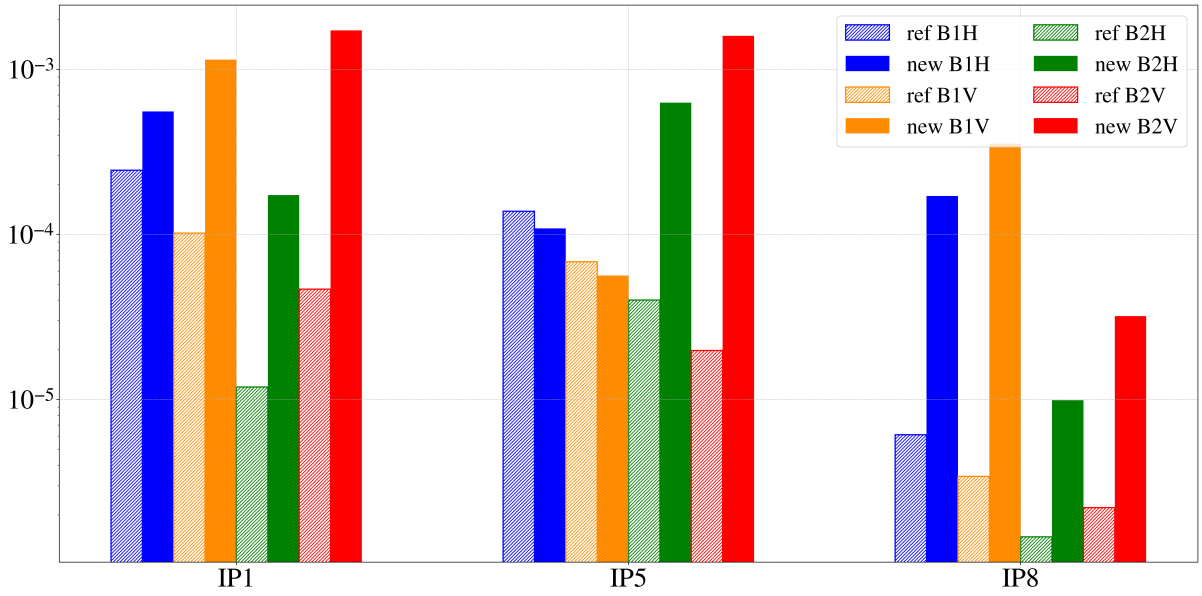


Figure 5.13: Comparison of measured tertiary collimator losses at top energy between the new and reference optics with tight TCT settings (logarithmic scale).

## 5.4. Impedance

The impedance measurements were carried out by the Accelerator and Beam Physics colleagues. The new IR7 optics at flat-top reduces the impedance-induced tune shift by 25% in the horizontal plane and 20% in the vertical plane for Beam 1, and 30% in the horizontal plane and 35% in the vertical plane for Beam 2 [2, 3]. These results show that the new optics is effective in mitigating the contribution of collimator impedance at flat-top.

## 5.5. Comparison measurements and simulations

Accurate predictions of beam losses are essential for assessing the cleaning performance of the collimation system. Previous studies have shown that a good agreement with measurements is important to build confidence in simulation tools to reliably predict beam loss patterns [8].

In the present work, the simulations were performed using the Everest scattering engine in Xcoll, which models the interaction of protons with collimators, providing the number and location of primary proton losses. The BLM system measures, instead, the secondary particles produced in the showers caused by protons lost in the collimators and surrounding machine components. Since the full showers are not simulated there are

certain limitations, in particular a comparison of the absolute energy deposition cannot be done. However, relative comparisons of the DS losses for different configurations have been shown empirically to be in good quantitative agreement with measurements [7]. The evolution of the cleaning inefficiency during the energy ramp is shown in Fig. 5.14 for simulated and measured results. The solid curves indicate the measured cleaning inefficiency, while the dashed ones correspond to the simulated one. Each curve was normalised to its mean value, allowing their trend to be compared. Beam 2 shows a good agreement, with the two curves closely following each other along the ramp. For Beam 1, the two curves show a less close agreement, although the overall behaviour remains similar. Overall, the comparison shows a good agreement between simulations and measurements.

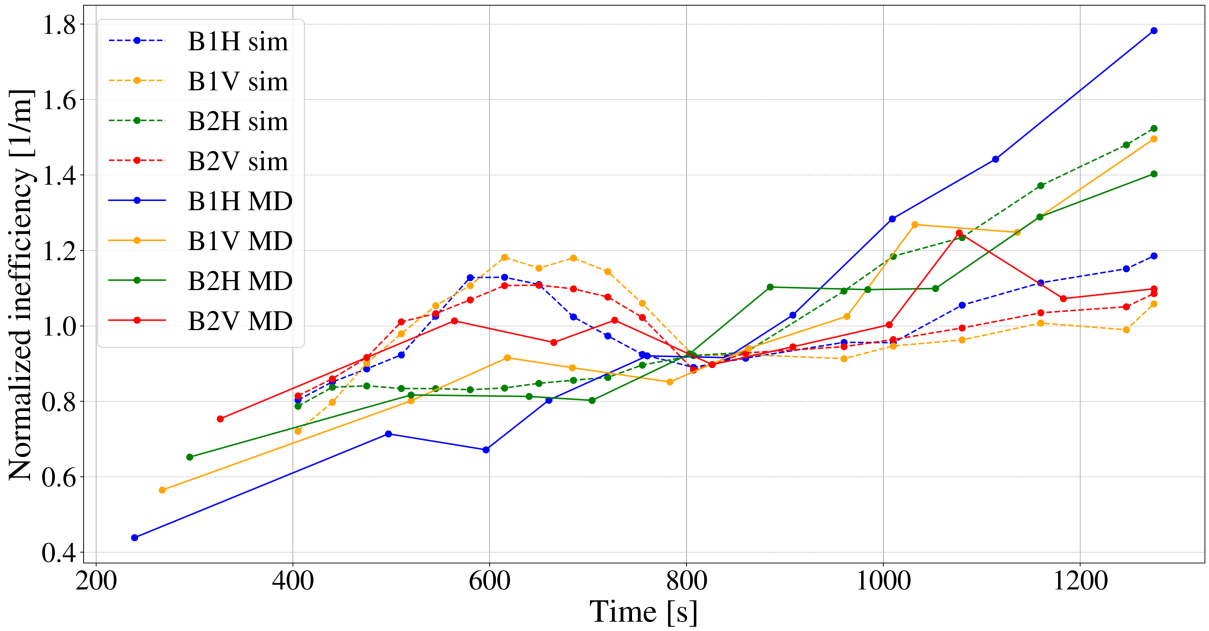


Figure 5.14: Comparison of cleaning performance in first DS cluster between MD results and simulation results (losses are normalized by their mean).

The ratio between the tertiary losses obtained with the new optics and those obtained with the reference optics is shown in Fig. 5.15 for IP1, IP5 and IP8. Most beams and planes show a good agreement between simulations and measurements, and only few cases show a clear difference. In particular, for B2V in IP1, B1V in IP5 and B1H/V in IP8 the simulated tertiary losses overestimate the measured ones.
In summary, the quantities analysed show a good agreement between simulations and measurements. In particular, the cleaning inefficiency comparison shows that the cleaning performance of the new optics is well-predicted by simulations.

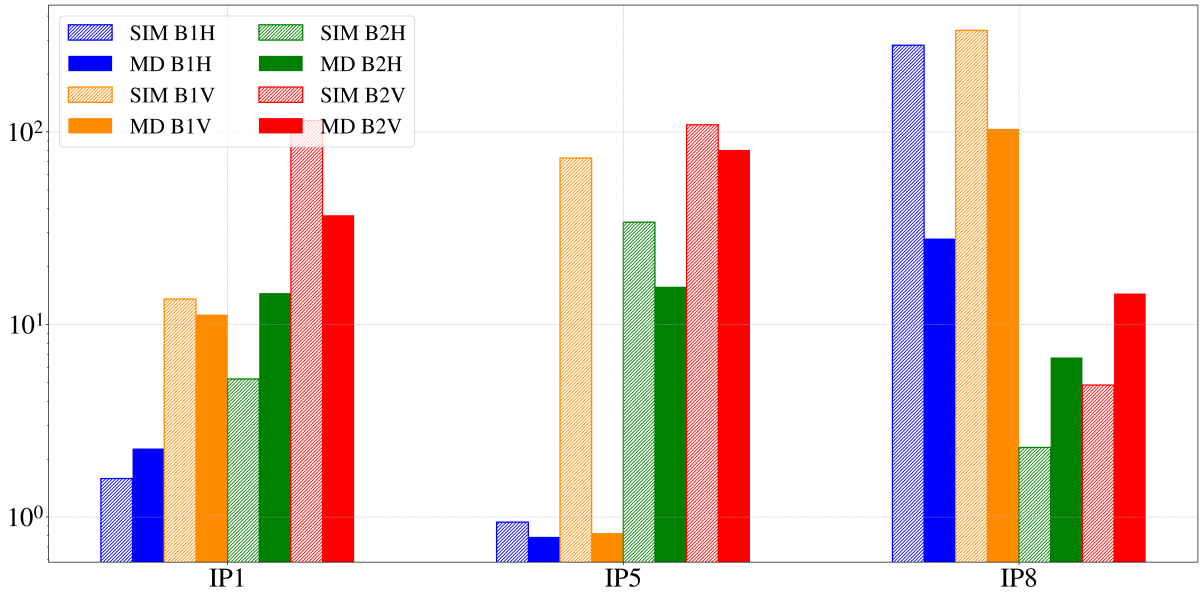


Figure 5.15: Comparison of tertiary collimator losses from measurements and simulations, expressed as the ratio between the new and the reference optics (logarithmic scale).

## 5.6. Beam loss performance with unsafe beams

The Beam Loss Monitoring (BLM) system plays a central role in the machine protection of the LHC, since it measures particle losses around the machine and ensures that they remain below the thresholds required to protect sensitive accelerator components, such as the superconducting magnets.

In addition to this, its high sensitivity and large dynamic range makes it a powerful tool to monitor beam losses during operation of the machine, providing accurate information about the intensity and the location of the beam losses.

The BLM signal is recorded in units of dose rate (Gy/s), which represents the energy deposited in the detectors by secondary particles. Through dedicated calibrations, the signals recorded immediately downstream of primary collimators, can be converted to the corresponding number of lost protons, allowing a measure of the proton loss rate from the beam [16]. Based on this, the beam lifetime and the power deposited in the collimation system can be calculated.

The beam lifetime is an essential indicator to assess the overall beam losses during the energy ramp. As defined in Eq. 2.35, it represents the characteristic time over which the beam intensity decreases. A shorter lifetime indicates a faster decrease of the beam intensity. During the energy ramp, the measured BLM signals are used to detect any significant reduction of the beam lifetime and to ensure that it remains within the oper-

ational safety limits.

The beam lifetime provides a global measure of the overall loss level in the machine. The individual BLM signals allow the analysis of specific loss locations, in order to verify whether any of them appear in critical or unexpected regions. In the LHC, each complete accelerator cycle from beam injection to beam dump is referred to as a *fill*. The plots show the high intensity fills taken during the MD session with the new optics. These are compared with reference fills of comparable intensities with reference optics.

Figure 5.16 shows the beam lifetime, expressed in hours, measured with the BLM system during the energy ramp for Beam 1 and Beam 2. The colored lines represent the new optics fills, with 12, 74, 444 bunches per beam, while the gray lines represent the reference fills. It can be observed that, for both beams, the lifetime with new optics is consistent with reference fills throughout the energy ramp. This consistency shows that the gradual transition toward the new optics configuration along the ramp does not lead to higher beam losses compared to the reference optics configuration.

For Beam 1, a reduction of the lifetime is observed in all the new optics fills around the middle of the ramp, approximately between 650 s and 800 s. However, the lifetime remains well above 300 hours, ensuring that the losses remain safely within operational limits.

The vertical dashed lines correspond to the intermediate matched points, i.e. times where the optics are explicitly matched to satisfy all machine constraints. Small drops in the lifetime occur around several of these points. The origin of this feature is not fully understood and further analysis is required.

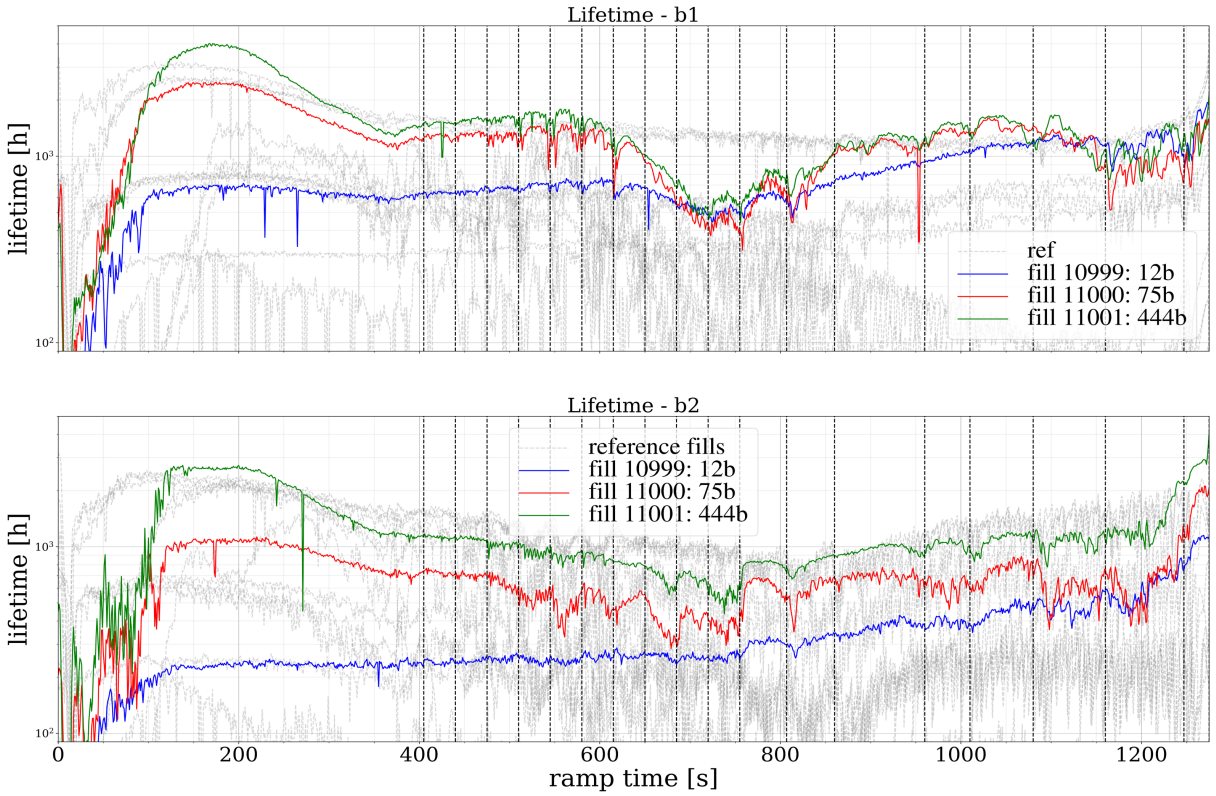


Figure 5.16: BLMs losses measured during energy ramp (coloured lines are new optics fills and grey lines are reference fills).

Since the lifetime gives the overall beam losses during the ramp, the BLM signals of individual collimators in IR7 are analysed to investigate the local distribution of losses in more detail.

Figures. 5.17 and 5.18 show the beam losses measured at the indicated collimators during the energy ramp for both beams. In general, the losses for Beam 2 are higher than those for Beam 1 throughout the ramp.

Analysing the individual collimator losses in more detail, some patterns between Beam 1 and Beam 2 can be observed. In particular, the loss pattern at TCSPM.6R7.B1, a secondary collimator for Beam 1), in Fig. 5.17, has a similar loss profile to TCP.C6R7.B2, a primary collimator for Beam 2. This suggests that the losses measured at TCSPM.6R7.B1 are induced by Beam 2.

The same behaviour is observed for Beam 1 collimators TCP.D6L7, TCSG.D4L7, TCSPM.B4L7 and TCSPM.E5R7 (orange, green, brown and pink lines), which show the same loss pattern. This profile matches the one observed at TCP.D6R7.B2, primary collimator for Beam 2, indicating that these losses originate from Beam 2.

In conclusion, these observations indicate the presence of consistent loss patterns in IR7,

with losses detected in one beam that are induced by the other due to secondary shower propagation.

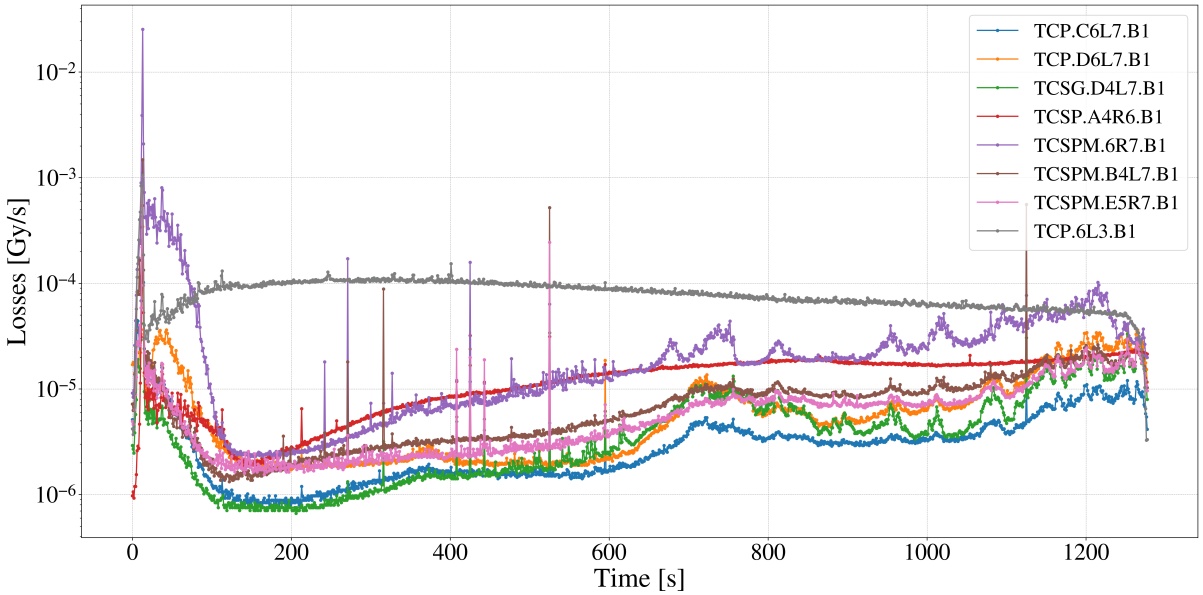


Figure 5.17: BLMs individual signals (Beam 1 ).

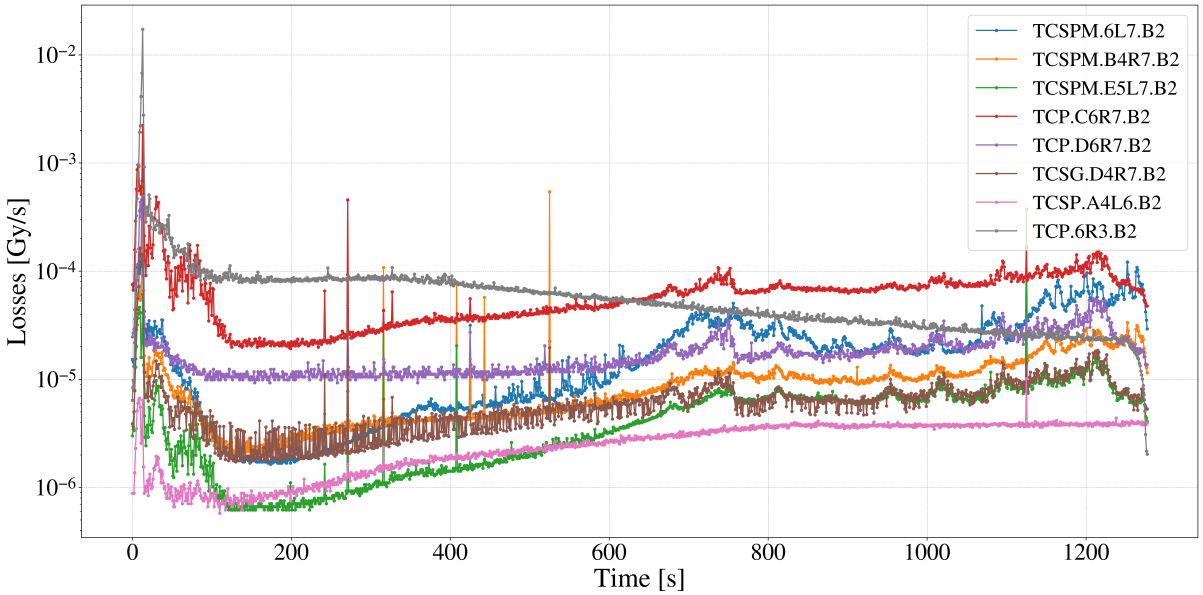


Figure 5.18: BLMs individual signals (Beam 2 ).

To further investigate the loss patterns, the primary collimator TCP.D6R7.B2 is examined in detail.

Figure 5.19 shows the BLM signal at this collimator together with the orbit measured by the Beam Position Monitors (BPMs). BPMs are electrodes installed around the beam pipe that measure the transverse position of the circulating beam with respect to the centre of the vacuum chamber. BPMs provide a measurement of the beam orbit, which is the actual transverse trajectory travelled by the protons along the accelerator.
A correlation can be observed between orbit jumps and loss spikes in the BLM signal: when the orbit suddenly drops, a corresponding loss spike appears, indicating that orbit changes can enhance particle losses. This is in particular a concern for the primary collimators, since they define the maximum extent of the beam halo and represent the global aperture bottleneck. Figure 5.20 shows the difference between the motor position of the collimator, which is the requested jaw position, and the LVDT position, which is the measured jaw position. Around 600s there is a sudden change of about 50 $\mu m$, and looking at the orbit measurement, there is a shift at the same time. Since the collimator motion is non-monotonic during the ramp, the motor reverses direction at that time. Because of the mechanical backlash, the actual jaw position does not follow the commanded position immediately, leading to a sign change in the motor-LVDT difference when the motor starts moving in the opposite direction. Overall, the beam losses observed in this case during the ramp are small enough to not be of concern. Nevertheless, monotonic jaw functions should be maintained in future to avoid possible issues if the mechanical backlash were to degrade further.

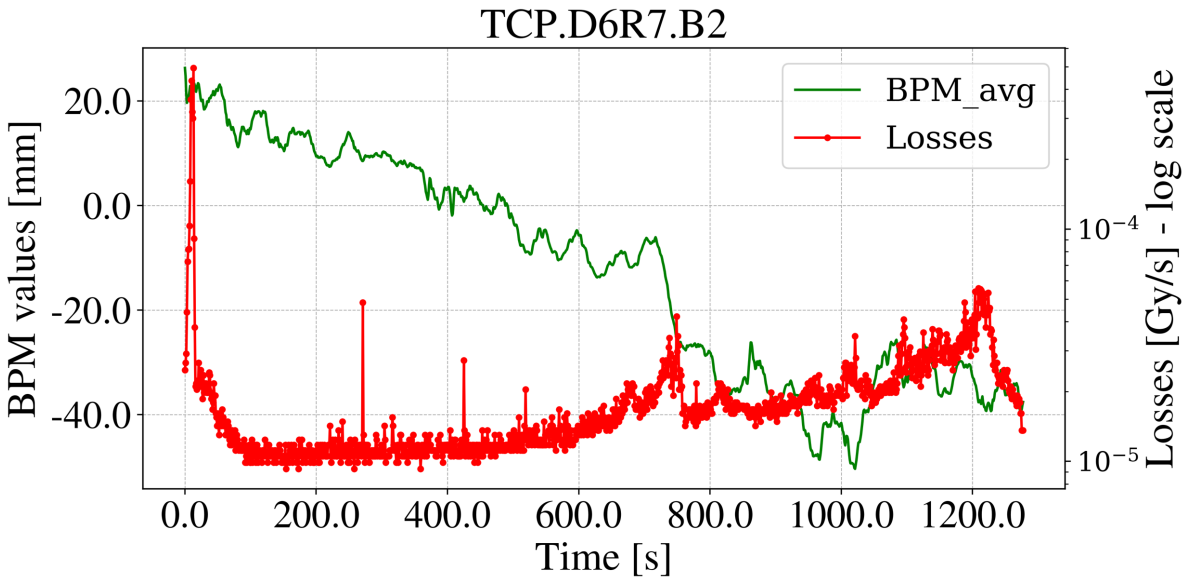


Figure 5.19: BLM individual signal for TCP.D6R7.B2 with orbit .

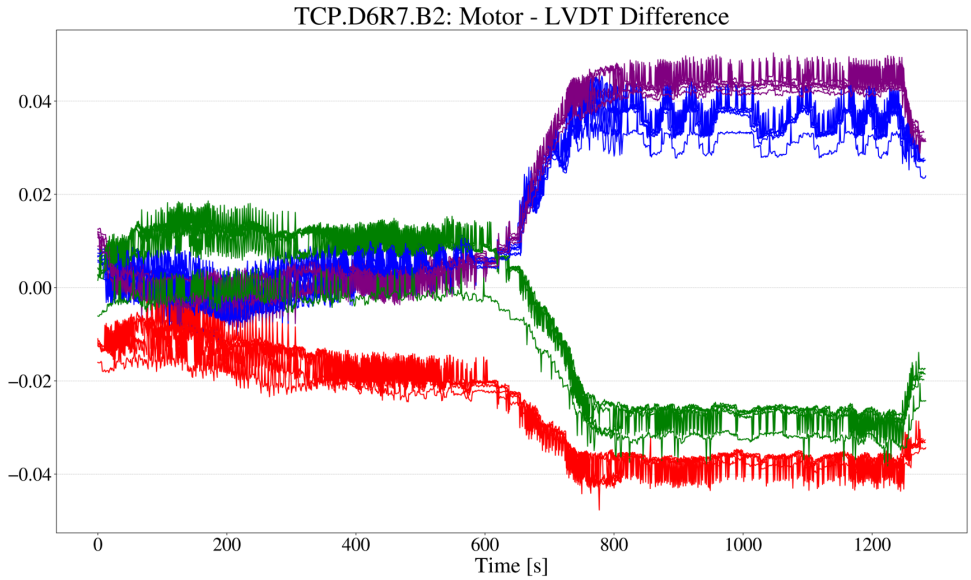


Figure 5.20: Difference between motor position and lvdt position for TCP.D6R7.B2. The four curves correspond to the motor-lvdt difference measured by the four lvdt sensors installed on the collimator, as each jaw is monitored by two sensors at its upstream and downstream ends.

# 6 | Conclusions

The High-Luminosity Large Hadron Collider (HL-LHC) project aims at pushing the accelerator technology beyond its present performance. The main objectives of HL-LHC are a fivefold increase of the instantaneous collision rate and a tenfold increase of the integrated luminosity with respect to the LHC nominal design values. In order to achieve these targets, a key factor is an increase of the bunch intensity from $1.15 \times 10^{11}$ ppb to $2.2 \times 10^{11}$ ppb. This poses unprecedented challenges to the collimation system, for which an upgrade is foreseen.

A first challenge is associated with beam losses, as leakage into the dispersion suppressor (DS) magnets downstream of the betatron collimation insertion can lead to quenches. In addition, operations with higher intensities might be limited by the machine impedance, which can lead to beam instabilities. The collimation system is the main contributor to the LHC impedance at top energy.

A new IR7 optics at top energy was developed in previous work to address both of these challenges. The new optics improves the cleaning performance and the impedance without requiring additional hardware.

The first main goal of the new optics is an increase of the beta function at primary collimators, improving collimator efficiency and resulting in larger phyisical gaps, improving both the cleaning performance and the impedance. The other main goal is an increase of the single-pass dispersion from the primary collimators to the downstream shower absorbers, which further improves the cleaning performance. However, these improvements introduce new operational challenges.

At injection energy, the aperture margins are not sufficient due to the large beta functions, making it necessary to introduce the new optics configuration during the energy ramp: a delicate and complex procedure that has never been done operationally before at CERN. Moreover, the increase of the beta function during energy ramp results in non-monotonic movement for some collimators, that can potentially cause mechanical backlash.

The goal of this thesis is the design and validation of the optics transition between the

nominal and new IR7 configurations during the LHC energy ramp. The work addressed the first operational implementation of the new optics in the LHC cycle.

A smooth optics transition was developed from the reference configuration at injection energy to the new IR7 optics at top energy. This required satisfying aperture constraints and developing the matching procedure and tools using Xtrack. The resulting combined ramp and desqueeze was successfully implemented in machine tests with high intensity beams in the LHC in 2025.

Simulations and measurements show a clear reduction of the DS losses at top-energy compared to the reference scenario. In the best cases, the reduction reaches about up to 60%. Measurements show a decrease of the impedance-induced tune shift by up to 30% in the horizontal plane and 35% in the vertical plane. However, tertiary collimator losses increase, particularly for Beam 2 in the vertical plane in IP1 and IP5.

Both simulations and measurements show that, as the new optics is progressively deployed during the ramp, the cleaning performance improves compared to the reference optics. In simulations, the average DS losses start decreasing half-way through the ramp and then remain lower than those of the reference optics. Measurements show the same behaviour: the DS losses decrease compared to the reference scenario as the new optics is introduced.

The beam lifetime, measured by Beam Loss Monitors (BLMs), remains stable and consistent with reference conditions throughout the energy ramp for both beams. A small reduction is observed around 4 TeV for Beam 1, but the lifetime remains above 300 hours, and does not present any operational concern. Transient loss spikes are observed during the ramp, some of which are correlated with collimator jaw slippage due to the non-monotonic motion of certain collimators. However, these losses remain small. A comparison between simulated and measured cleaning inefficiency during the ramp shows a good agreement, indicating that the cleaning performance of the new optics is well predicted by simulation tools.

A remaining challenge associated with the new optics is the increase of the tertiary collimator losses at top energy. As shown by both simulations and experimental results, the largest increase occurs for Beam 2 vertical in IP1 and IP5. These losses contribute to experimental background and require further study to quantify their impact. They can be mitigated by optimising the phase advance between the primary collimators and tertiary collimators, an upgrade that is already included in the HL-LHC baseline.

The 2025 tests with high-intensity beams represent a crucial milestone demonstrating for the first time that the combined ramp and desqueeze of the new IR7 optics can

be safely deployed in the LHC. These results provide a solid basis for considering the operational deployment of the new optics in future LHC cycles. At the time of writing, its implementation is under evaluation for the 2026 run.

# Bibliography

[1] I. B. Alonso, O. Bruning, P. Fessia, M. Lamont, L. Rossi, L. Tavian, and M. Zerlauth, editors. *High-Luminosity Large Hadron Collider (HL-LHC): Technical Design Report*. CERN Yellow Reports: Monographs. CERN, 2020.

[2] C. Antuono. Private communication, Nov. 2025.

[3] C. Antuono, X. Buffat, L. Giacomel, N. Mounet, and J. Sonpar. Transverse impedance studies for hl-lhc. HL-LHC Collaboration Meeting, CERN, October 2025.

[4] G. Azzopardi et al. Lhc collimation control system for Run III operation. In *Proc. 18th Int. Con. on Accelerator and Large Experimental Physics Control Systems*, Shanghai, China, 2021.

[5] A. Bertarelli, O. Aberle, R. Assmann, E. Chiaveri, T. Kurtyka, M. Mayer, R. Perret, and P. Sievers. The mechanical design for the lhc collimators. In *Proceedings of EPAC 2004*, 2004.

[6] R. Bruce. Parameters for aperture calculations at injection for hl-lhc. Technical report, CERN, 2016.

[7] R. Bruce, R. W. Assmann, V. Boccone, C. Bracco, M. Brugger, M. Cauchi, F. Cerutti, D. Deboy, A. Ferrari, L. Lari, A. Marsili, A. Mereghetti, D. Mirarchi, E. Quaranta, S. Redaelli, G. Robert-Demolaize, A. Rossi, B. Salvachua, E. Skordis, C. Tambasco, G. Valentino, T. Weiler, V. Vlachoudis, and D. Wollmann. Simulations and measurements of beam loss patterns at the cern large hadron collider. *Phys. Rev. ST Accel. Beams*, 17:081004, Aug 2014. doi: 10.1103/PhysRevSTAB.17.081004. URL `https://link.aps.org/doi/10.1103/PhysRevSTAB.17.081004`.

[8] R. Bruce, R. W. Assmann, V. Boccone, C. Bracco, M. Brugger, M. Cauchi, F. Cerutti, D. Deboy, A. Ferrari, L. Lari, A. Marsili, A. Mereghetti, D. Mirarchi, E. Quaranta, S. Redaelli, G. Robert-Demolaize, A. Rossi, E. Skordis, C. Tambasco, G. Valentino, T. Weiler, V. Vlachoudis, and D. Wollmann. Simulation and measurements of beam loss patterns at the cern large hadron collider. *Physical Review Special Topics, Accelerators and Beams*, 2014.

[9] O. Bruning and L. Rossi. *The High Luminosity Large Hadron Collider: New Machine for Illuminating the Mysteries of the Universe*. World Scientific, 2 edition, 2024.

[10] O. Bruning, P. Collier, P. Lebrun, S.Myers, R. Ostojic, J. Poole, and P. Proudlock. *LHC Design Report, Vol. I: The LHC Main Ring*.

[11] F. Carra, A. Bertarelli, A.Dallocchio, L. Gentini, P. Gradassi, G. Maitrejean, A. Manousos, N. Mariani, N. Mounet, E. Quaranta, S. Redaelli, and V. Vlachodius. Mechanical engineering and design of novel collimators for hl-lhc. IPAC 2014, Dresden, Germany, 2014.

[12] CERN. The accelerator complex, 2022. URL `http://home.cern/science/accelerators/accelerator-complex`.

[13] CERN. LHC Collimation Project Home Page, 2025. URL `http://lhc-collimation-project.web.cern.ch`.

[14] CERN Accelerator and Technology Sector. Beam Performance Tracking (BPT), 2025. URL `http://bpt.web.cern.ch`.

[15] F. C. et al. Lhc run 3 optics corrections. In *Proc. IPAC'23*, .

[16] S. M. V. et al. Beam lifetime monitoring using beam loss monitors during lhc run 3. In *Proc. IPAC'23*, .

[17] R. A. Fernandez. Overview of the lhc performance in run 3. Conference Presentation, 2025.

[18] G. Iadarola, R. D. Maria, S. Lopaciuk, A. Abramov, X. Buffat, D. Demetriadou, L. Deniau, C. Droin, J. Dilly, P. Hermes, P. Kicsiny, S. Kostoglou, P. Kruyt, A. Latina, L. Mether, C. E. Montanari, K. Parascou, T. Prebibaj, F. Soubelet, G. Sterbini, and F. V. D. Veken. Xsuite: An integrated beam physics simulation framework. In *Proceedings of the 15th International Particle Accelerator Conference (IPAC2024)*, 2024.

[19] B. Lindstrom. Md7203: Rematched ir7 optics for improved cleaning and impedance. Presentation at the LSWG Meeting, CERN, 2024.

[20] B. Lindstrom, R. Bruce, X. Buffat, R. D. Maria, L. Giacomel, P. Hermes, D. Mirarchi, N. Mounet, T. Persson, S. Redaelli, R. Tomás, F. F. V. der Veken, and A. Wegscheider. Mitigating collimation impedance and improving halo cleaning with new optics and settings strategy of the hl-lhc betatron collimation system. In *Proc. 68th Ad-*

*vanced Beam Dynamics Workshop on High-Intensity High-Brightness Hadron Beams (HB2023)*, Geneva, Switzerland, 2023.

[21] B. Lindström, R. Bruce, X. Buffat, R. D. Maria, L. Giacomel, P. Hermes, D. Mirarchi, N. Mounet, T. Persson, S. Redaelli, R. T. García, F. V. der Veken, and A. Wegscheider.

[22] B. Linstrom. *Criticality of fast failures in the High Luminosity Large Hadron Collider*. PhD thesis, Uppsala University, Uppsala, Sweden, 2020.

[23] S. Redaelli. Beam cleaning and collimation systems. In R. Schmidt, editor, *Proceedings of the Joint International Accelerator School: Beam Loss and Accelerator Protection*, 2016.

[24] R. Schmidt, editor. *Proceedings of the Joint International Accelerator School: Beam Loss and Acceleration Protection*, CERN Yellow Reports, Geneva, Switzerland, 2016. CERN.

[25] R. Steerenberg, R. Alemany-Fernandez, M. Albert, T. Argyropoulos, E. Bravin, G. Crockford, J.-C. Dumont, K. Fuchsberger, R. Giachino, M. Giovannozzi, G.-H. Hemelsoet, W. Hofle, D. Jacquet, M. Lamont, E. Metral, D. Nisbet, G. Papotti, M. Pojer, L. Ponce, S. Redaelli, B. Salvachua, M. Schaumann, M. S. Camillocci, R. Suykerbuyk, G. Trad, S. Uznanski, J. Uythoven, D. Walsh, J. Wenninger, and M. Zerlauth. Operation and performance of the cern large hadron collider during proton run 2. In *Proc. 10th International Particle Accelerator Conference (IPAC'19)*, Melbourne, Australia, 2019.

[26] R. Tomas, O. Bruning, R. Calaga, S. Fartoukh, A. Franchi, M. Giovannozzi, Y. Papaphilippou, S. Peggs, and F. Zimmermann. Procedures and accuracy estimates for beta-beat correction in the lhc. Technical report, CERN, 2006.

[27] R. Tomas, T. Bach, R. Calaga, A. Langner, Y. I. Levinsen, E. H. Maclean, T. H. B. Persson, P. K. Skowronski, M. Strzelczyk, G. Vanbavinckhove, and R. Miyamoto. Record low $\beta$ beating in the lhc. *Physical Review Special Topics - Accelerators and Beams*, 2012.

[28] S. M. Vigo, B. Salvachua, P. Hermes, S. Redaelli, C. Zamantzas, C. P. Welsch, and J. Wolfenden. Beam lifetime monitoring using beam loss monitors during lhc run 3. In *Proc. IPAC'23*, 2023.

[29] J. Wenninger. Machine protection and operation for the lhc. Technical report, CERN, 2016.

[30] H. Wiedemann. *Particle Accelerator Physics*. Springer, 2007.